ACTUATION FATIGUE AND FRACTURE OF SHAPE MEMORY ALLOYS

A Dissertation

by

CEYLAN HAYRETTIN

Submitted to the Office of Graduate and Professional Studies of
Texas A&M University
in partial fulfillment of the requirements for the degree of

DOCTOR OF PHILOSOPHY

Chair of Committee,	Ibrahim Karaman
Committee Members,	James G. Boyd
	Dimitris C. Lagoudas
	Miladin Radovic
Head of Department,	Ibrahim Karaman

December 2017

Major Subject: Materials Science and Engineering

ABSTRACT

Shape memory alloys (SMAs) are promising candidates for solid state actuators since they have the highest energy density among all active materials. However, before SMA solid state actuators can be used in practical applications, especially where their failure can cause casualties, fatigue and fracture properties of these functional materials under actuation thermal cycling conditions must be thoroughly understood.

There are two general approaches for evaluating fatigue response of materials. First one is life based or total life approach, where materials are cycled until failure either under stress/load control or strain/displacement control. Second approach is called damage tolerant approach, in which the materials with known crack lengths are subjected to cyclic loading and crack's growth is monitored. Even though it is limited, there are few studies published in literature on the life based approach for the actuation fatigue of SMAs, where the samples are thermally cycled under a mechanical load. However, to the best of author's knowledge, there is no systematical work on the damage tolerant approach for the actuation fatigue of SMAs. The main goal of this dissertation is to systematically study the actuation fatigue behavior of SMAs with both life based and damage tolerant fatigue approaches. Moreover the effects of microstructure on the actuation fatigue performance of SMAs are investigated. Both conventional low temperature SMAs, NiTi based, and recently discovered stable high temperature shape memory alloys (HTSMAs), NiTiHf based, are studied. Two compositions of binary NiTi namely $Ni_{49.5}Ti_{50.5}$ and $Ni_{50.3}Ti_{49.7}$

and one composition of ternary $Ni_{50.3}Ti_{19.7}Hf_{20}$ are used and their microstructures are modified by precipitation heat treatments. The microstructure is evaluated using transmission electron microscopy and scanning electron microscopy. Mechanical and thermal properties are determined using differential scanning calorimetry, thermo-mechanical tests such as monotonic tension, incremental strain superelasticity, and isobaric heating cooling tests.

It is found that microstructure has a significant effect on the actuating fatigue of SMAs. In NiTiHf, the peak aged condition outperforms overaged conditions in terms of fatigue performance. It is also found that surface finish has a strong effect on fatigue life of tested material. Counter intuitively, the samples with electric discharge machining recast layer have significantly longer fatigue lives than mechanically or electro-chemically polished samples. Damage tolerant approach on the actuation fatigue results shows stable crack growth in NiTi SMAs and the rate of crack growth per thermal cycle is reported. It is found that under comparable average stress intensity factors the crack growth rate during thermal cycling is significantly larger than those under the mechanical cycling.

Improving understanding of actuation fatigue of SMAs not only addresses a missing link in scientific literature but also helps accelerate the development of solid state actuators. With better tools and data, design against fatigue can be performed more accurately and efficiently. Development of damage tolerant approach is expected to better assess remaining fatigue life of components with existing cracks. Other shape memory compositions and microstructures that are not studied in this work can be investigated in future using the methods described in this work.

DEDICATION

This thesis and my life are dedicated to my sons Ismail Arda Hayrettin, Ishak Aras Hayrettin and my future kids.

ACKNOWLEDGEMENTS

First and foremost, I want to thank my advisor Prof. Karaman for all his support throughout the six though years. I had my ups and downs but he believed in me and mentored me. He is truly one of the best advisors a PhD student can ask for. Beyond his contribution to my personal development, he thought me a lot about science, specifically shape memory alloys. His passion to research is unparalleled and he is the most hardworking person I have ever seen.

I would like to thank Prof. Lagoudas, for invaluable collaboration, mentoring and occasional moral boost I received from him. There were times that I had results that I don't think very promising, hearing good words from him gave me boost that help me continue.

I also would like to thank to Prof. Boyd and Prof. Radovic for serving in my committee and giving me valuable suggestions throughout my studies. Moreover, I want to thank them for being so understanding and help me with my tight deadlines.

I am grateful beyond measures to Jim Mabe from Boeing. I learned great deal on testing, data collection, lab organization and preparing presentations. Also he provided invaluable material and technical assistance to my research without which several chapters of thesis would not be possible.

Prof. Baxevanis deserves a special thank. He was like a co-advisor to me. His expertise in fracture mechanics is ground breaking. If anybody can model fracture and

fatigue on shape memory alloys without any experimental data, it would be him. I am really happy to be able to work with him and pick his brain a little.

I want to sincerely thank to Drs. Noebe and Benafan from NASA Glenn Research Center for providing valuable material and guidance throughout my studies.

I would like to thank to Murat Kaynak, Robert Barber, Michael Elverud and Micheal Bass for their help in machine shop. They are my machine shop Gurus. There are thing you can't learn by reading such as using some tools. They patiently thought me how to use tools and also machined numerous pieces for me.

I want to thank my international collaborators. Prof. Chumlyakov was like a grandfather figure to our group. His knowledge in shape memory alloys and his energy is unrivaled. He is also the master of single crystals. I want to thank to him specifically for numerous meetings where I learned a great deal and received valuable directions and suggestions. Prof. Santamarta helped me a lot with TEM. I am thankful to him for not only obtaining images but helping me understand microstructure and the linkage between microstructure and mechanical properties. Prof. Hans Maier hosted me one summer in Paderborn, Germany. Going to Germany during summer was like an oasis in a desert. Apart from pleasant climate change, I learned a lot on mechanical properties of materials and experimentation from him and his group. I also experienced European way of working.

I sincerely thank all the people of "MESAM Group", including but not limited to Sezer Picak, Brian Franco, Dr. Anup Brandyopadhyay. That is the only research group I was a part of but I heard horror stories about how people can turn into each other and make

a though working environment. Thankfully we had a great working environment where everybody are friends and help each other. Special thanks to Ebubekir Dogan and Alper Evirgen thank you guys for valuable technical discussions and training as well as fun past time activities. Ruixian Zhu, Sonia Razavi, Taymaz Jozaghi, Ji Ma, Nick Bruno, Nick Barta, Hande Ozcan, Stephanie Sultan and Joel Sam, thank you very much for being wonderful office mates. Serdar Ozguc, Wahaz Nasim, Jeff Brown and David Rodin, thank you very much for being my undergraduate assistants. I made you do tons of polishing sorry about that. Hopefully you learned some stuff in between :). Omer Karakoc and Benjamin Young, thanks for taking over the projects after me and your help in transition in addition to your company and friendship. Last but not least Tarik Aydogmus, Pinar Karpuz, Kadri Can Atli, Nevin Ozdemir, Prof. Demircan Canadinc thank you very much for everything. Although our time together in Texas A&M was limited, I will always remember our time as fun and happy.

I can't leave my friends out of MESAM group unmentioned. Eda Aydogan, Gokhan Gungor, Alper Kinaci, Simge Andolsun, Mehmet Tatli, Behrouz Haghgouyan, Chris Calhoun, Rob Wheeler, and John Rohmer, thank you all for very nice time we had together.

Last but not least I want to thank my family for their never ending support. My wife Duygu Hayrettin, my parents Sabriye and Sunay Hayrettin and my sister Sibel Hayrettin, thank you very much!

CONTRIBUTORS AND FUNDING SOURCES

This work was supervised by a dissertation committee consisting of Professors Ibrahim Karaman, Miladin Radovic and Dimitris Lagoudas of the Department of Materials Science and Engineering, and Professor James Boyd of the Department of Aerospace Engineering.

The data analyzed for Section 4 was provided in part by Christopher Calhoun and Omer Karakoc. Charpy Impact tests in Section 4 were conducted in Professor Maier's laboratory in University of Paderborn. The data analyzed for Section 5 was provided in part by Robert Wheeler and Omer Karakoc. The transmission electron microscopy data and analysis in Section 6 was provided by Professors Santamarta and Pons from The University of the Balearic Islands, Department of Physics. Collaborating Professors acknowledge the financial support from Spanish MINECO and FEDER under Project Number MAT2014-56116-C4-1-R.

All other work conducted for the dissertation was completed by the student independently.

This work was made possible in part by the Boeing Company, US Air Force Office of Scientific Research (AFOSR) under Grant Numbers FA9550-12-1-0218, FA9550-15-1-0287 and National Science Foundation (NSF) under Grant Number CMMI-1534534.

Its contents are solely the responsibility of the authors and do not necessarily represent the official views of the Boeing Company, AFOSR, and NSF.

NOMENCLATURE

ASTM	American Section of the International Association for Testing Materials
A_f	Austenite finish
A_p	Austenite peak
A_s	Austenite start
BSE	Back scattered electron
CT	Compact Tension
σ_{sim}	Critical stress for stress induced martensitic transformation
DSC	Differential scanning calorimetry
DIC	Digital image correlation
DSLR	Digital single lens reflex
DC	Direct Current
σ_y	Effective Yield Stress
EPFM	Elasto-plastic fracture mechanics
EDS	Energy dispersive spectroscopy
EDX	Energy dispersive X-ray
FEA	Finite element analysis
FC	Furnace cooled
HTSMA	High temperature shape memory alloy
T_H	Homologous temperature

LEFM	Linear elastic fracture mechanics
LVDT	Linear variable differential transformer
LCT	Lower cycle temperature
LPS	Lower plateau stress
M_d	Martensite desist
M_f	Martensite finish
M_p	Martensite peak
σ_{mr}	Martensite reorientation stress
M_s	Martensite start
OWSME	One-Way shape memory effect
PID	Proportional integral derivative
SEM	Scanning electron microscopy
SE	Secondary electron
SAEDP	Selected area electron diffraction pattern
SMA	Shape memory alloy
SWT	Smith-Watson-Topper
SHT	Solution heat treatment
TTT	Time-Temperature-Transformation
TEM	Transmission electron microscopy
TWSME	Two-way shape memory effect
TWSMS	Two-way shape memory strain
ε_{uts}	Ultimate tensile strain

σ_{uts}	Ultimate tensile stress
UCT	Upper cycle temperature
UPS	Upper plateau stress
VIM	Vacuum induction melting
WQ	Water quenched
XRD	X-Ray diffraction
σ_{ys}	Yield stress

TABLE OF CONTENTS

Page

LIST OF FIGURES

Page

LIST OF TABLES

Page

1. INTRODUCTION

This chapter focuses on the significance of the fatigue and fracture for shape memory alloys, especially for solid state actuator applications. The current state of the art on the fundamental understanding of the fatigue mechanisms, use of classical fatigue and fracture theories for shape memory alloys (SMAs), especially under actuation cycling, and the limitations of these methods will be discussed. In the later part of this section, the goals of this work will be summarized and approaches to reach the objectives will be presented.

1.1 Motivation

Fatigue is the biggest cause of failure on all structural materials. It has been estimated that 90% of all failures are due to fatigue [1]. Thus it is important to establish a fundamental understanding and generate sufficient experimental data for the fatigue response of SMAs to develop solid state actuators based on SMAs. Despite its importance there is only limited amount of work available in literature on the actuation fatigue behavior of SMAs. This has been partly due to the lack of interest on actuator applications in the past. The current primary market for SMAs is biomedical industry where only superelastic effect is used. As a result, the main focus in SMA fatigue response was in the area of mechanical fatigue. Due to recent increase in interest for SMA solid state actuators from aerospace, automotive, oil and gas, and consumer electronic industry, the demand

for better understanding the fatigue and fracture of SMAs during actuation cycling has risen.

Solid state actuators are desired in aforementioned industries to reduce weight, volume or complexity by eliminating moving parts [2]. Thanks to SMAs ability to show reversible repetitive phase transformation under high stress levels (up to 500 MPa) and generating several percent strain, SMA based actuators have power-density values comparable with or higher than existing actuation systems such as hydraulic and electric motors. In addition, SMA based actuators can have smaller weights [2]. The weight versus power/weight ratio plot for common actuation technologies and shape memory alloys can be seen in Figure 1.1.

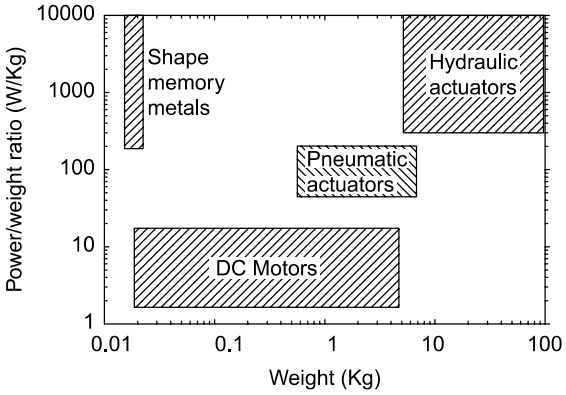

Figure 1.1 Power to weight ratio versus weight chart, showing shape memory alloy actuators and competing technologies such as hydraulic, pneumatic and direct current (DC) motor actuators [3]

On the other hand, there are also several disadvantages of SMA actuators. Energy conversion efficiency of an SMA actuator is far lower than electro-mechanical conversion [4]. Actuation frequency of SMAs are also lower than other actuation technologies or active materials. Due to fact that, stroke is generated by thermally induced phase transformation, time to complete an actuation cycle is limited with heating and cooling rates. One other concern for SMA actuators is auto-actuation. Auto-actuation is defined as unintentional activation of actuator due to temperature fluctuations in the environment. Since SMA actuator works with thermal stimulation, if the environment the device stays experience high enough temperatures, active material will transform and actuate unintentionally. One way to prevent auto-actuation is to increase transformation temperatures of SMA components. Current commercially available alloys have transformation temperatures lower than 100 °C. It is important to develop reliable high temperature shape memory alloys (HTSMA) to prevent against auto-actuation. One other benefit of development of HTSMAs would be increasing the actuation frequency without the need for active cooling systems. For Newtonian cooling, rate of cooling is higher at elevated temperatures with the same ambient temperature. Another disadvantage of SMA actuators is the uncertainty regarding to reliability. Since actuation fatigue life of SMAs are not studied extensively, high confidence levels on life prediction cannot be achieved.

Despite its disadvantages, there are applications where currently available technologies are not feasible or effective, and SMAs can perform better those technologies. A chart showing applications of SMAs for both superelasticity and shape memory effects can be seen in Figure 1.2 [5]. Note that despite many potential applications

for shape memory effect or actuation, the superelasticity application market is currently much bigger. There is a relatively new increase in demand for aerospace applications, including adaptive gas turbine clearance control [6,7], SMA torque tube actuated flaps for adaptive trailing edges and reconfigurable rotor blades [8], variable geometry nozzles [9] and chevrons [10]. Although some of those proposed applications used in tests flights such as variable geometry chevrons in 2006 and adaptive trailing edges in 2012, none is commercially available as of now.

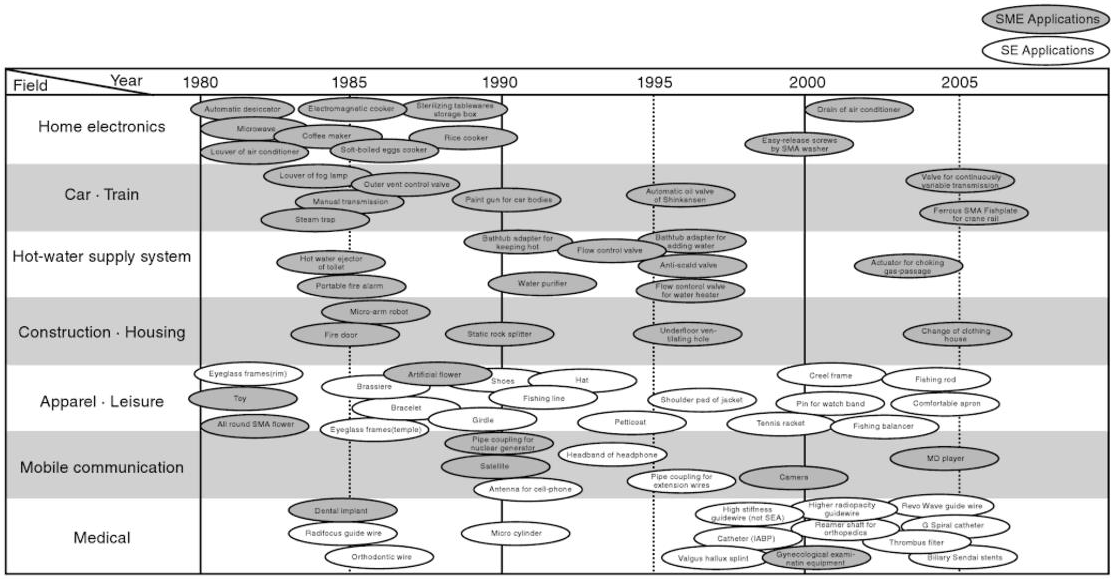

Figure 1.2 Shape memory alloy applications time line with application fields in Japan. Compiled by Yamauchi et. al. [11]

1.2 Objectives

In the light of the brief background given above, the overarching aims of this dissertation are to:

1. Develop material testing methods for the evaluation of the actuation fatigue, fracture and crack growth behavior under actuation cycling,
2. Evaluate different classical fatigue life approaches to determine the most appropriate approach for better understand the fatigue mechanisms, establish empirical relations and find ways to compare different SMAs and associated microstructures,
3. Study the effects of microstructure on the fatigue performance of SMAs.
4. Evaluate methods of measuring fracture toughness in SMAs, including linear elastic fracture mechanics and elasto-plastic fracture mechanics. Moreover determine fracture toughness values and effect of phase on their values.
5. Analogous to damage tolerant fatigue approach, develop a method to measure crack growth rate on actuation fatigue and generate data on studied SMA compositions.

To be able to do achieve these objectives, three compositions of materials were chosen. First and second materials are commercially available binary NiTi compositions of $Ni_{50.7}Ti_{49.3}$ and $Ni_{49.5}Ti_{50.5}$ with lower transformation temperatures and the third one is custom fabricated NiTiHf high temperature SMA. It is desired to increase the strength of the material to prevent from plastic deformation due to high applied stress and increasing dimensional stability during thermal cycling under stress. Although it is possible to

strengthen the materials with various different methods including but not limited to solid solution hardening, grain size reduction, strain hardening or cold working, and precipitation hardening, the method to change microstructure in this study is chosen to be precipitation heat treatments. Whenever possible, the microstructure of materials is modified to investigate the effect of the precipitates. Each material-microstructure pair is characterized to obtain transformation temperatures and basic material properties. Later, actuation fatigue tests are performed on these materials to demonstrate the effects of microstructure on fatigue performance. Moreover, a correlation between easily measurable quasi-static mechanical properties and the fatigue performance is sought for. Another important issue to tackle is to identify the best metrics to quantify the fatigue performance. There are several fatigue life prediction methods with different metrics to quantify/predict the fatigue lives of materials. Their applicability and feasibility to differentiate the performance of different materials is evaluated.

The first goal of this study is to investigate the effects of microstructure on nickel rich binary NiTi and ternary NiTiHf SMAs and find correlations between quasi-static mechanical properties and fatigue performance. The data obtained from binary NiTi can serve as the baseline behavior for the high temperature SMA NiTiHf performance. Different precipitate configurations (size and distribution) are to be obtained using different heat treatments. Tensile actuation fatigue testing is employed to determine fatigue performance.

The second goal of this work is to develop a better method for quantification of fracture toughness of SMAs. All major fracture toughness measurement approaches are

evaluated in terms of applicability to SMAs. Moreover the effects of temperature or phase constitution on toughness as well as effect of sample thickness are investigated.

Finally, crack growth characteristics of SMAs during thermal cycling under different load levels are studied. The major goal of crack growth studies is to develop a modified Paris' Law for SMAs to be used in actuator applications, which does not currently exist. If successful, the results and knowledge based generated in this study are expected to make it possible to apply damage tolerant approach for SMAs for designing against fatigue. In other words, if an actuator material determined to have a crack with a known length, remaining life of the part could be captured given that the path for stresses and thermal fluctuations are known.

More explicitly, the objectives of this study can be summarized as follows:

1. Effects of microstructure on nickel rich binary NiTi ($Ni_{50.7}Ti_{49.3}$) and ternary NiTiHf ($Ni_{50.3}Ti_{29.7}Hf_{20}$) will be determined. Microstructure will be modified by precipitation heat treatments. Four different heat treatments are considered for $Ni_{50.7}Ti_{49.3}$ and three for $Ni_{50.3}Ti_{29.7}Hf_{20}$. Mechanical properties and transformation characteristics of the samples will also be investigated and the correlations between easily measurable quasi-static material properties and fatigue response will be evaluated. In addition, different methods to compare various materials performance metrics will be studied.
2. Extended thermo-mechanical cycling under shear on $Ni_{50.3}Ti_{29.7}Hf_{20}$ torque tubes will be studied. Evolution of accumulated plastic strains, stability of

actuation as well as two-way shape memory effect and its stability will be studied.

3. Fracture toughness of binary equatomic NiTi ($Ni_{50}Ti_{50}$) and $Ni_{50.3}Ti_{29.7}Hf_{20}$ in martensitic and austenitic states will be measured. Compact tension (CT) samples will be used in this study. Applicability of linear elastic fracture mechanics and elasto-plastic fracture mechanics will be evaluated.
4. Based on the critical values obtained from fracture toughness measurements, crack growth behavior of $Ni_{50}Ti_{50}$ and $Ni_{50.3}Ti_{29.7}Hf_{20}$ will be studied by conducting tests where force is kept constant and temperature is cycled. After obtaining crack growth rates for difference force levels, the applicability of a modified Paris' Law for SMAs will be studied.

2. BACKGROUND

This section focusses on the general background for shape memory alloys and phenomena such as superelasticity and shape memory effect as well as fatigue and fracture of SMAs. The literature on actuation fatigue and fracture will also be summarized.

2.1 Shape Memory Alloys

Shape memory alloy is a class of materials with unique ability to show repetitive and reversible phase transformation which can be induced thermally or mechanically [12,13]. The phases of SMAs are named as austenite and martensite regardless of their crystallographic structure. Austenitic phase is stable at higher temperatures and under low stress, where martensitic phase is stable at low temperatures and under high stress. Phase transformation in SMAs is martensitic, in other words, nearest neighbors of an atom does not change and all the atoms move collectively and less than one atomic distance with respect to their nearest neighbors. The austenitic crystal structure has higher symmetry than the martensitic crystal structure. The difference in crystal symmetry is essential for reversibility of macroscopic shape change or strain. Transformation of austenite crystal to martensitic crystal results in net shape change but do not result in significant volume change. Due to difference in symmetry, one austenite lattice can transform into several different martensitic lattices. Relation between two crystal structures determines how many variants an austenite lattice can transform into.

The processes happening in SMAs, with different mechanical and thermal paths has been illustrated in Figure 2.1[14] . If austenite to martensite transformation happens under no stress, martensite crystals twins to accommodate previous shape. That kind of transformation does not yield to macroscopic shape change and microstructure is called self-accommodated martensite or twinned martensite. Later if self-accommodated martensite is subjected to stress, ratio of different twin variants changes in favor to the ones which produces macroscopic strain. This process is called detwinning, and resulting microstructure is named as detwinned martensite. Since all martensite variants originates from same austenite crystal, if detwinned martensite is heated up shape change due to detwinning can be recovered. This phenomena is called shape memory effect.

In addition of shape memory effect, SMAs are also capable of showing super-elasticity. Super-elasticity, which is also called pseudo-elasticity is the process where austenite transforms to martensite due to applied stress in a temperature where austenite phase is stable. Resulting martensite has detwinned morphology. Upon removal of stress, detwinned martensite transforms back to austenite and recovers the macroscopic strain generated during loading.

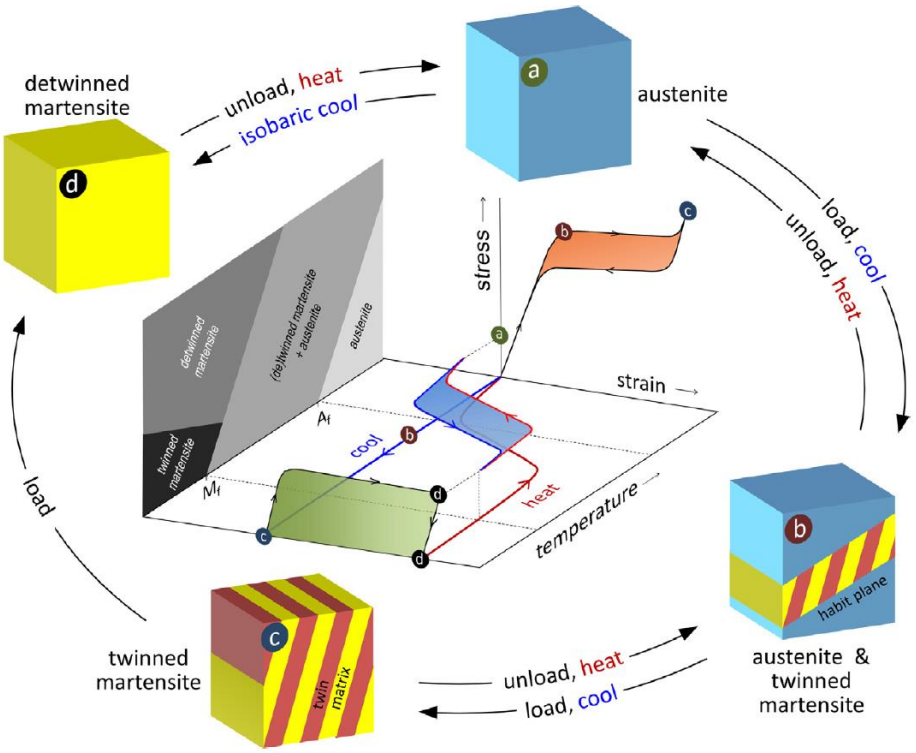

Figure 2.1 Schematic of phase transformation and different morphologies in SMAs [14]

The martensitic transformation in SMAs shows hysteretic behavior, i.e. forward and reverse transformation does not occur at the same point in temperature and stress space. Moreover, the forward and reverse transformations does not occur at a single temperature but rather in a range. When initial state of the material is austenite, upon cooling martensitic transformation starts, and the temperature at which the transformation starts is called martensite start temperature (M_s). The temperature at which the transformation is completed is called martensite finish temperature (M_f). Similarly the onset and completion of austenitic transformation are called austenite start (A_s) and

austenite finish (A_f) temperatures, respectively. Martensitic desist temperature (M_d) is defined as the temperature at which the critical stress for stress-induced martensitic transformation is equal to the stress to deform austenite plastically, thus, the main deformation mechanism above M_d is conventional plasticity rather than the phase transformation [12,15].

Although reversible martensitic transformation [16] and stress induced martensitic transformation was documented for other alloys earlier, shape memory effect (which requires both of the aforementioned phenomena) is first discovered in AuCd alloy in 1950s [17,18]. Later more alloy systems showing shape memory effect were discovered namely, InTi, NiTi [19], CuZn. Upon many SMA compositions, NiTi is most studied and commercially available class due to their superior mechanical properties, excellent corrosion resistance and good biocompatibility. Because of aforementioned properties NiTi found itself a decent amount of commercial applications. First NiTi application utilized shape memory effect and was a pipe coupler. Later applications mostly utilized pseudo-elasticity such as in orthodontic wires, stents, eye glass frames.

2.1.1 Binary NiTi

Binary NiTi is one of the most commercially available and most studied SMA. In NiTi, austenite has B2 (cubic) crystal structure where martensite has B19' (monoclinic). That combination yields to 12 correspondence variants. Location of B2 and B19' in Ni-Ti phase diagram can be seen in Figure 2.2 [20].

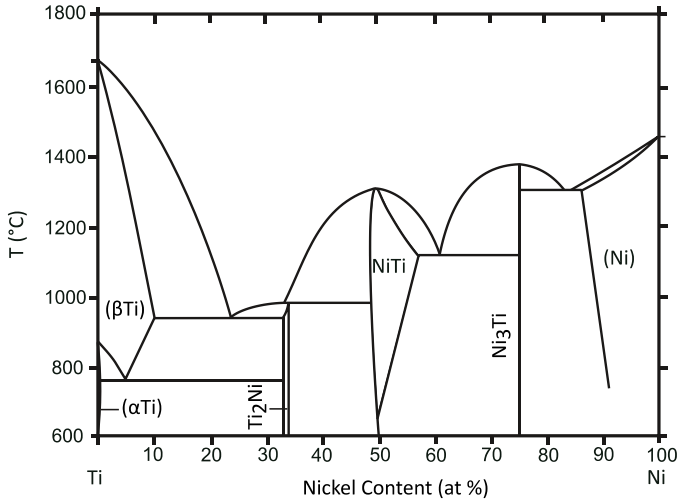

Figure 2.2 Binary NiTi phase diagram [20].

Although NiTi is an intermetallic, at elevated temperatures there is a non-stoichiometric single phase region. On the titanium rich side of NiTi intermetallic precipitated phase is Ti_2Ni. Because Ti solubility on NiTi is not increasing significantly with temperature and Ti_2Ni precipitates stabilized by oxidation, it is not possible to dissolve Ti_2Ni precipitates once they form. On the other hand in Ni rich compositions it is possible to form super saturated Ni rich NiTi. It is also possible to age super saturated NiTi to form desired precipitate structure. Stable Ni rich precipitate is Ni_3Ti. But aging of NiTi produces Ni_4Ti_3 metastable phase particles as can be seen in time-temperature-transformation (TTT) plot in Figure 2.3. The crystal structure of Ni_4Ti_3 precipitates is rhombohedral, $R\bar{3}$ [21–23], which is significantly different from both austenite and martensite.

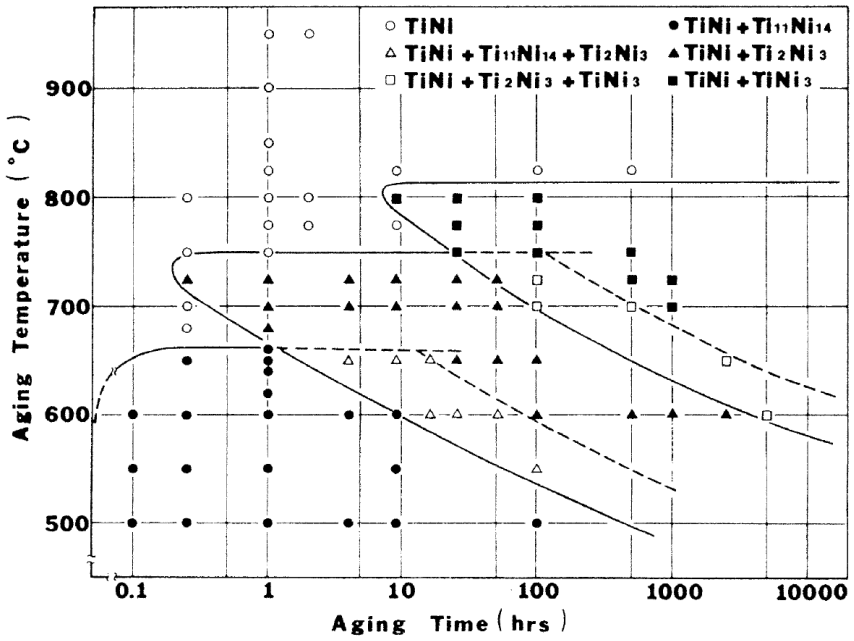

Figure 2.3 Time-temperature-transformation (TTT) plot for $Ni_{52}Ti_{48}$ showing precipitation path in Ni rich NiTi [24].

Transformation temperatures on NiTi is very strongly dependent to composition as can be seen in Figure 2.4. When Ni content is below 50%, transformation temperatures don't change much. But between 50 and 52 % Ni, they drastically drop[25]. Thus it is possible to control transformation temperatures with changing composition. Moreover, since precipitates are Ni rich, it is possible to form precipitates and change matrix composition to change transformation temperatures. In the case of precipitation, there are two competing effect on transformation temperatures. First one is matrix composition as mentioned earlier. Second one is constraint in martensite nucleation by precipitates [26]. The latter is most effective when inter particular distance is comparable to critical nucleus size of martensite. Existence of two competing effect establish itself as non-monotonous

behavior on transformation temperatures versus precipitate size or heat treatment duration plots. On such plots there is an initial drop in transformation temperatures especially for low temperature short duration aging or small precipitates. Upon increasing aging time or temperature in other words increasing precipitate size, transformation temperatures increases [26,27].

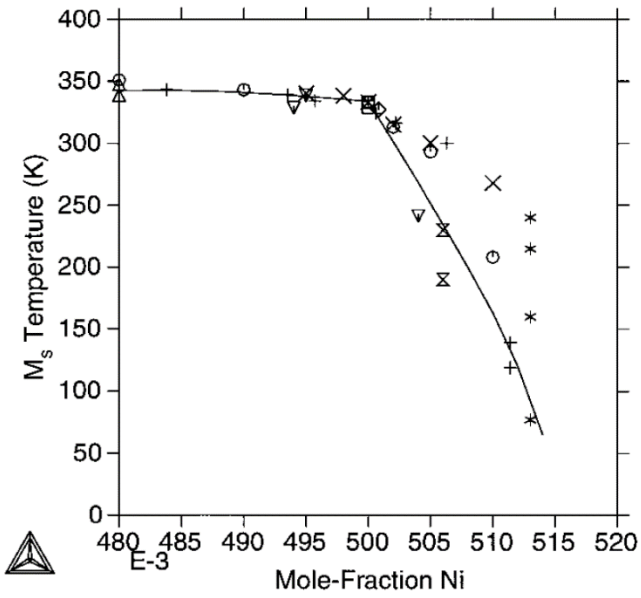

Figure 2.4 Effect of Ni content on transformation temperatures, namely M_s.[25]

The general material strengthening methods such as solid solution hardening, work hardening which also known as strain hardening, grain refinement and precipitation, also work for NiTi shape memory alloys [28].

2.1.2 NiTiHf High Temperature Shape Memory Alloys

One way to increase transformation temperatures of NiTi SMAs is ternary alloy addition [28,29]. Hf and Zr are cheaper alternatives to other alloying element candidates such as Au, Pt and Pd. Similar to binary NiTi, NiTiHf has austenite structure of B2 (cubic) and martensite structure of B19' (monoclinic). NiTiHf phase diagram can be seen in Figure 2.5. Note that, phase diagram on figure a shows solidus line which is the end of solidification and slice of ternary phase diagram is for 50 % Ni thus doesn't show precipitates. Similar to binary NiTi, phase diagrams don't present metastable states.

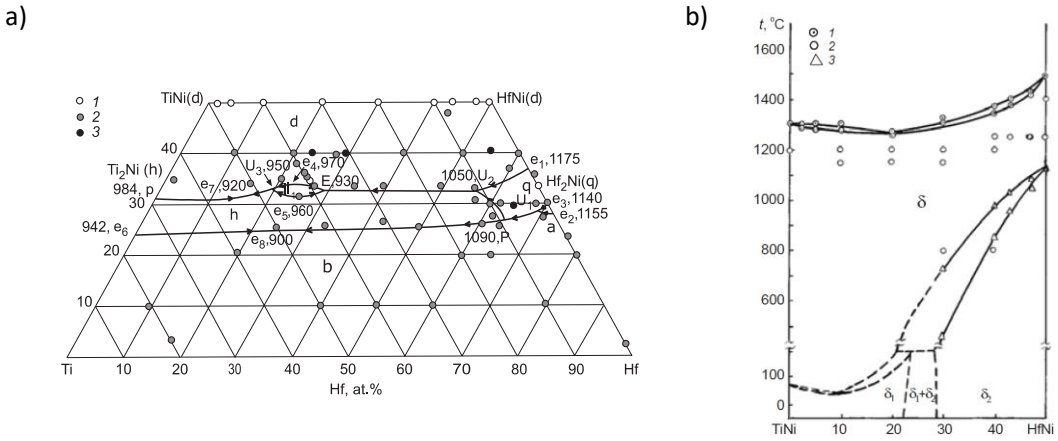

Figure 2.5 NiTiHf phase diagrams a) Ternary NiTiHf phase diagram showing liquidus surface projection [30] b) slice of ternary NiTiHf phase diagram among 50% Ni line [31]

Hf occupies Ti cite in NiTiHf unit cell. Similar to binary NiTi, NiTiHf intermetallic phase has certain solubility of Ni, Ti and Hf. It is also possible to form Ni

rich precipitates and dissolve them back to matrix via solutionization by going to temperature and composition coordinate on phase diagram where single phase is stable. Composition of precipitates formed by aging, is reported to be around 52.4 % Ni, 18.0 % Ti and 29.6 % Hf [32,33]. The phase is dubbed as "H phase" and its structure is determined to be a super structure of austenite phase, orthorhombic [32,34] specifically $L2_1$ [32].

Transformation temperature of NiTiHf is also a function of composition. Dependence of Ni and Hf content can be seen in Figure 2.6. Similar to binary NiTi, transformation temperatures of NiTiHf drops significantly with increasing Ni content beyond 50 %, at the same time addition of Hf monotonically increases transformation temperatures [3].

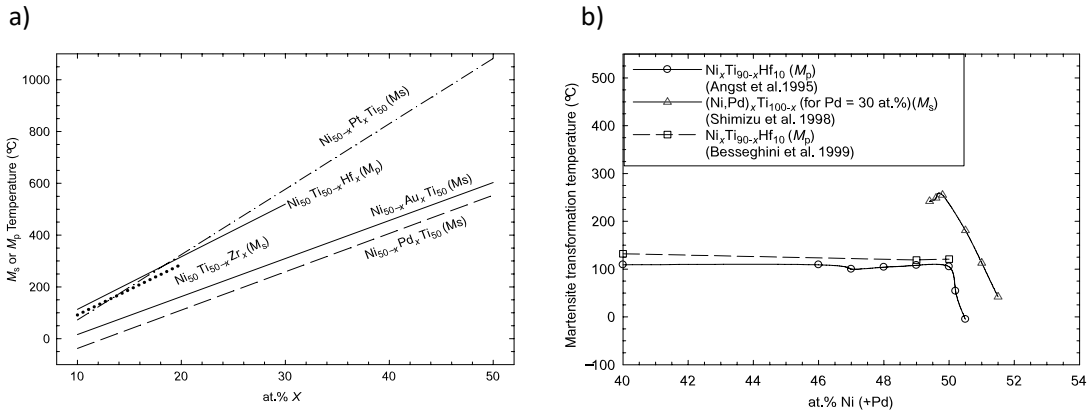

Figure 2.6 Effect of composition on transformation temperatures of NiTi based high temperatures shape memory alloys. a) Effect of ternary alloying addition (Pt, Hf, Zr, Au, Pd) on Ms b) Effect of Ni content in NiTiHf and NiTiPd SMAs [3]

Earlier studies on NiTiHf SMAs started on compositions where Ni content kept below 50 at. % [32,35,36]. Recently, higher than 50 at. % Ni alloy systems have attracted attention because of the enhanced mechanical and thermal stability due to the formation of nano-precipitates in these compositions. Moreover, Ni rich side of the stoichiometry makes it possible to tailor transformation temperatures with precipitation heat treatments [27,32].

2.2 Fatigue of Materials

Fatigue is defined as failure of a material under repetitive application of stress even at values that are much lower than what is required for yielding the material in a single stress application [1]. It is a relatively old field of science since the earliest work on fatigue dates back to 1830s [37]. The challenge in understanding the fatigue behavior of materials is to establish methodologies to present and compare the fatigue performance of materials, and develop empirical or physics based models to eventually predict the fatigue response of materials under any given loading condition and loading path. Below, some of these approaches are summarized.

2.2.1 Life Based Approach

Life based approach is used in many material systems and it is the historically first method designed to quantify fatigue performance. Wohler developed the way to represent fatigue of materials with stress amplitude-life plots called S-N curves. Note that strain amplitude-life curves are called ε-N curves. A typical S-N curve can be seen in Figure 2.7.

Note that some materials, notably iron based alloys, have a critical stress below which materials survive more than testing cutoff (typically 10^7 cycles). It is also customary to divide fatigue regimes into two, namely "low cycle fatigue" for lives less than 10^5 cycles and "high cycle fatigue" for anything more than that [1].

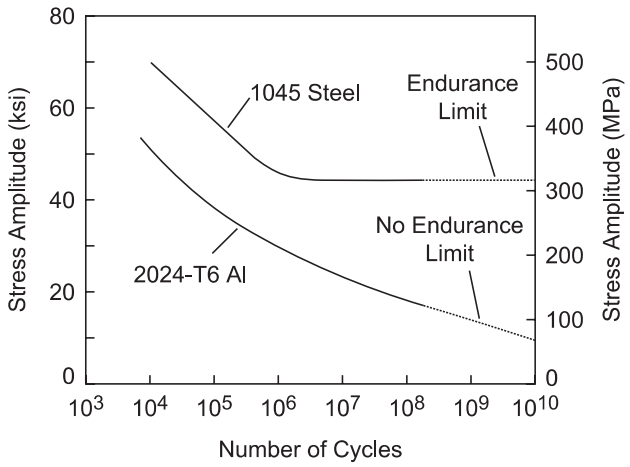

Figure 2.7 An illustration of S-N curve showing endurance limit and no endurance limit materials [1]

First empirical life prediction functions developed by Wohler in 1870s by fitting linear correlation to S-N curves [38], where y axis is linear and x axis is logarithmic, a fatigue life prediction function can be obtained in the form of equations 2.1 or 2.2 [39]. Note that A and B are material constants and $\Delta\sigma$ is stress range or difference between maximum and minimum stress during fatigue cycling, and N is fatigue life or number of cycles to failure.

$$Log(N) = A + B(\Delta\sigma)$$ eq. 2.1

$$Log(N) = A + B(S_{max})$$ eq. 2.2

Empirical life prediction functions developed by Basquin is in high cycle fatigue range [1,37]. The form of Basquin fatigue law can be seen in equation 2.3, where σ_a is stress amplitude, σ_f' is the fatigue strength coefficient, and b is the fatigue strength exponent. Typical values for b is within -0.05 and -0.12 where smaller b means longer fatigue life for comparable σ_f'. Similarly for comparable b, smaller σ_f' means higher fatigue life. Note that because b is in the power of fatigue life its effect is much more significant. Although Basquin fatigue life is developed initially for high cycle fatigue range it is also used for low cycle fatigue life prediction [1,37,40].

$$\sigma_a = \sigma_f'(2N)^b$$ eq. 2.3

The most common fatigue life prediction function used in low cycle fatigue regime is called Manson-Coffin law. The equation formulating the law can be seen in equation 2.4, where $\Delta\varepsilon_p$ is plastic strain per cycle, $\frac{\Delta\varepsilon_p}{2}$ is plastic strain amplitude, ε_f' is the fatigue ductility coefficient, and c is fatigue ductility exponent. Typical values for c are in between -0.5 and -0.7.

$$\frac{\Delta\varepsilon_p}{2} = \varepsilon_f'(2N)^c$$ eq. 2.4

It is also common to combine Basquin and Manson-Coffin fatigue laws into one master prediction formula as shown in equation 2.5 [1,37,40].

$$\frac{\Delta\varepsilon}{2} = \frac{\sigma_f'}{E}(2N)^b\varepsilon_f'(2N)^c$$ eq. 2.5

Note that so far only stress or strain amplitudes were considered when determining fatigue life. To specify mean stress, the ratio between minimum and maximum stress during a fatigue test being reported and it is denoted by R. For fully reversed loading condition R is equal to -1. Each R value generate a shifted S-N curve. Historically first mean stress effect corrections were developed for high cycle fatigue range as corrections to Basquin law. Three most common methods for this, are Goodman, Soderberg and Gerber and their respective equations can be seen in equations 2.6, 2.7 and 2.8 [1,37].

$$\sigma_a = \sigma_e \left[1 - \left(\frac{\sigma_m}{\sigma_{uts}}\right)\right] \quad \text{eq. 2.6}$$

$$\sigma_a = \sigma_e \left[1 - \left(\frac{\sigma_m}{\sigma_y}\right)\right] \quad \text{eq. 2.7}$$

$$\sigma_a = \sigma_e \left[1 - \left(\frac{\sigma_m}{\sigma_{uts}}\right)^2\right] \quad \text{eq. 2.8}$$

Other methods to take effect of mean stress into account were also developed such as Smith-Watson-Topper (SWT). In this work, SWT method will be used extensively. In that method, one of the expression has the form of equation 2.9.

$$\sqrt{(\sigma_a + \sigma_o).\varepsilon_a.E} = A.N^a + B.N^b \quad \text{eq. 2.9}$$

Similar to previous nomenclature, σ_a is stress amplitude, σ_0 is mean stress, ε_a is strain amplitude, E is elastic modulus, A, a, B and B are material constants, and N is fatigue life Note that this expression can be further simplified by setting B=0 for the cases where log-log plot of $\sqrt{(\sigma_a + \sigma_o).\varepsilon_a.E}$ vs fatigue life is linear instead of piecewise linear. Lastly an expression can be rewritten to be in the form of equation 2.10.

$$\sigma_{max}\varepsilon_a = A'N^{c'} \quad \text{eq. 2.10}$$

That form will be used in the rest of the study.

Lastly it is worth mentioning that, fatigue life of stepwise loading condition in other words application of different stress or strain amplitudes for certain durations, can be calculated by Miner's rule. In this rule, the hypothesis is the fatigue life is determined by an internal damage variable and that variable is additive with multiple steps.

There are also ASTM standards that describes the relevant testing procedures. For strain amplitude controlled testing ASTM E606 should be used where for stress controlled testing ASTM E467 is suitable.

2.2.2 Damage Tolerant Approach

Damage tolerant approach makes it possible to assess remaining fatigue life of parts with existing cracks by predicting crack growth rates, given that the loading profile is known. Although previous crack growth laws existed at the time, Paris and Erdogan's work unified different modes of crack growth and yield to one unified law which is called Paris' law. Basic Paris law has the following structure

$$\frac{da}{dN} = C\Delta K^m \qquad \text{eq. 2.11}$$

where a is crack length, N is number of cycles, da/dN is crack growth rate per cycle, C is a material constant, K is stress intensity factor, ΔK is stress intensity amplitude and m is another material constant. Typical value for m is between 2 to 4 for metallic materials and 4 to 100 for ceramics and polymers [1].

Paris' law defines stress intensity factor amplitude (ΔK) as main driving force and fatigue life prediction variable. A typical crack growth rate versus stress intensity factor amplitude plot can be seen in Figure 2.8. Note that material response has 3 distinct

behaviors in its respective regions. In “Region I” a threshold (ΔK_{th}) can be observed below which crack doesn’t grow. In “Region II” stable crack growth is observed and described by Paris’ law. In “Region III” rapid crack growth is the phenomena that is present and significant deviation from Paris’ law can be observed.

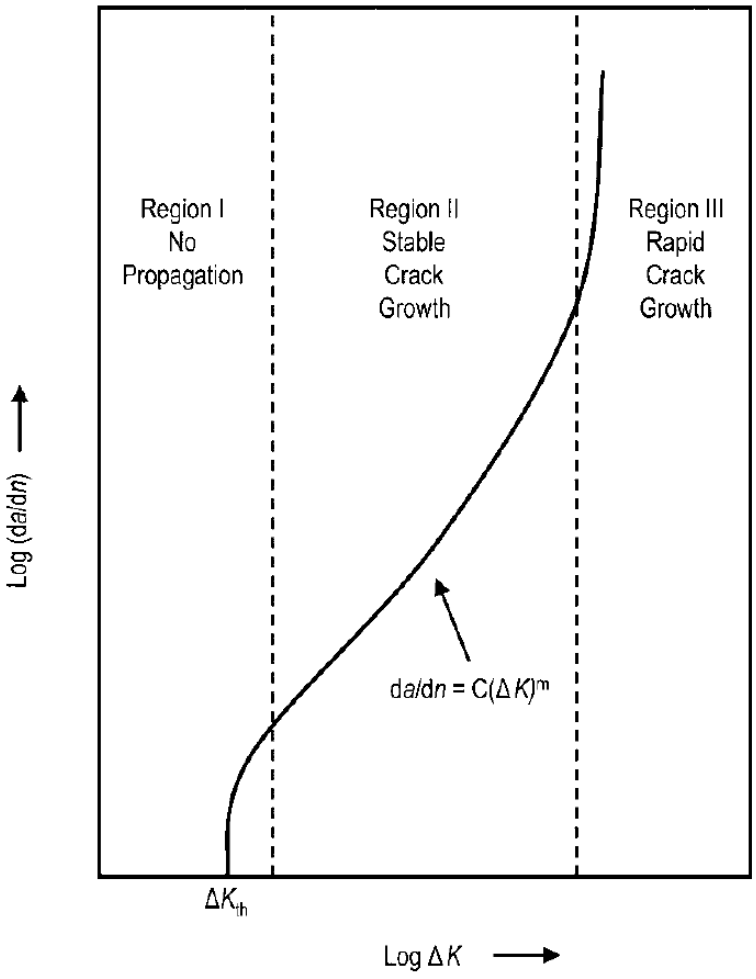

Figure 2.8 A schematic of typical crack growth versus stress intensity factor amplitude plot. The 3 distinct region of crack growth can also be seen [1].

Note that similar to life based approach, mean stress or stress intensity factor in damage tolerant case also has an effect. Ratio between minimum and maximum stress intensity factor is denoted by R similar to life based approach. It is common to present different R values in the same plot to indicate effect of mean stress intensity factor. One correction method is in the form of in equation 2.12 and named as Forman method [41]. where Kc is critical stress intensity factor in other words fracture toughness. Note that this method requires prior knowledge of fracture toughness.

$$\frac{da}{dN} = \frac{C\Delta K^m}{(1-R)K_c - \Delta K} \qquad \text{eq. 2.12}$$

It is possible to modify Paris' law to take mean stress intensity factor into account with other forms. A Modified Paris' law [42,43] can be seen in equation 2.13.

$$\frac{da}{dN} = C\Delta K^p K_{max}^n \qquad \text{eq. 2.13}$$

Lastly it is common to normalize stress intensity factor with elastic modulus [44–46] as can be seen in equation 2.14. It is reported that response of most engineering metallic materials collapse to a single stable crack growth region [45] where $C=5.1x10^6$ and m=3.5.

$$\frac{da}{dN} = C\left(\frac{\Delta K}{E}\right)^m \qquad \text{eq. 2.14}$$

Experimental determination of aforementioned properties standardized by ASTM with E647. Two sample geometries are suggested in the standard namely compact tension samples and notched tension samples (middle or side notches).

2.3 Fatigue of Shape Memory Alloys

Due to unique properties of shape memory alloys, in addition to regular mechanical fatigue, a specific version of thermo-mechanical fatigue is also relevant. In this mode which is called “actuation fatigue”, stress is kept constant or can be varied as a function of strain and temperature is cycled.

2.3.1 Mechanical Fatigue of Shape Memory Alloys

Life based approach for the mechanical fatigue mode is studied extensively for NiTi and other SMAs. Results of typical mechanical fatigue experiments are presented with S-N or ε-N curves where one axis is stress or strain amplitude respectively, depending on the controlled variable and the other axis is the number of cycles to failure. Specimen geometries can be bulk dog-bone [45,47–50], wire [51–53] and other application driven shapes [54,55]. Stress mode can be uniaxial tension-tension [53,56,57], compression-compression[55], tension-compression [45,47,48], torsion [54] or rotation bending [51,52] at constant temperature. Frequencies of cyclic loading is typically around 1 Hz, but can range from 0.04 to 10 Hz. A compilation of mechanical fatigue results can be seen in Figure 2.9. Stress controlled fatigue results were shown in Figure 2.9.a and strain controlled test results were shown in Figure 2.9.b.

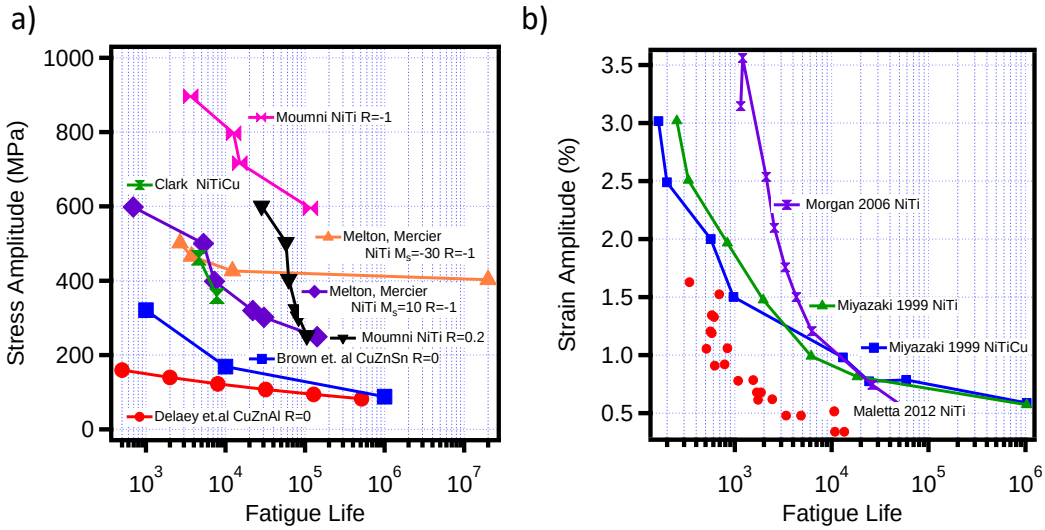

Figure 2.9 Compilation of selected mechanical fatigue results on SMAs. a) stress controlled experiments[45,48,55–57] d) strain controlled experiments[49,51,58]

Note that fatigue performance is vastly changing between different compositions, microstructure and R. It can be concluded that in general NiTi shows better fatigue performance then Cu based (CuZnAl [57] and CuZnSn [56]) shape memory alloys.

Runciman et. al. studied effect of stress ratio and stress mode (tension, torsion and bending) [50]. Results were shown in Figure 2.10 .It is reported that effect of stress mode can be corrected by using normalized stress (Cauchy) and strain (Lagrangian). Moreover a modified Manson-Coffin approach was used in this study where instead of plastic strain amplitude transformation strain amplitude is used. The results with modified Manson-Coffin approach can be seen in Figure 2.10.

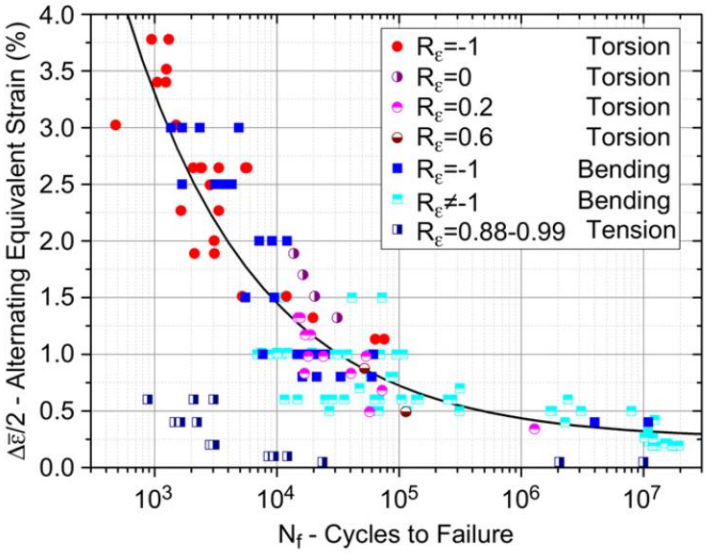

Figure 2.10 Effect of loading method demonstrated with modified Manson-Coffin approach. Equation of trend line is $\Delta\varepsilon/2=0.25+49.6\ N_f^{-0.4}$. Note that only significant deviation is from high mean stress tests R=0.88 – 0.99 [50]

Miyazaki et. al. studied effects of test temperature [51], microstructure [59] and composition [51]. Summary of aforementioned studies can be seen in Figure 2.11. It can be concluded that increasing temperature decreases fatigue performance and strengthening with changing microstructure increases fatigue life in higher stresses but decreases it under lower stress levels.

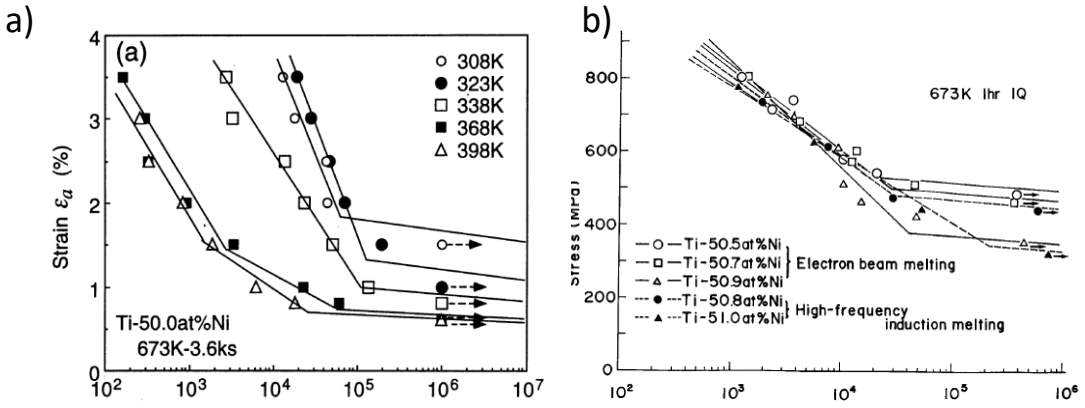

Figure 2.11 Mechanical fatigue of NiTi a) Effect of test temperature [51] b) Effect of microstructure [59]

Several fatigue life predication laws, such as Wohler [51,59], Manson-Coffin [45,47,49], and Smith-Watson-Topper [60] were utilized for mechanical fatigue of SMAs. In addition to established fatigue life prediction laws an energy based fatigue life criteria was also developed [48,53,61].

Since SMAs are functional materials, fracture is not the only way to render a part useless. If the material lost its reversible phase transformation ability or elongates more than its design allowables, it can be deemed failed. Because of this distinction, the fatigue of SMAs can be divided into two groups, depending on how material fails. If the material fails with fracture, it is called structural fatigue [62]. Likewise if the material is deemed failed due to the loss of actuation or substantial permanent plastic strain, it is called functional fatigue [62].

Although literature on it is much more limited compared to life based approach, damage tolerant approach was also studied for SMAs. First studies of crack growth reported by Melton and Mercier [45] on binary NiTi. Effects of inclusion content [63], testing environment [64,65], phase constitution and temperature [66,67], load ratio R or mean stress intensity factor [67–69], loading frequency [69], sample thickness [69], and microstructure [46] were studied. A good compilation of most of the literature on damage tolerant approach can be found in Robertson et. al. [60].

2.3.2 Actuation Fatigue of Shape Memory Alloys

Limited literature is available on actuation fatigue of shape memory alloys. Report format of this type of studies varies greatly from one study to another. Common representations involve one or combinations of stress, actuation strain, plastic deformation level and work output (product of actuation strain and applied stress) in one axis where fatigue life or number of cycles to failure on the other. Specimen geometries can be bulk dog-bone [70–72], wire [73–79] and other application driven shapes [80]. Stress mode is mostly constant tensile while constant compression [55] and to a much limited extend variable stress as a function of displacement [78] is also reported. Frequency of thermal cycling changes significantly with sample geometry. It can be as high as 2 seconds per cycle for wires to as low as 8 minutes for bulk samples.

Historically actuation fatigue gained attraction with development of SMA heat engines in late 1980s[81] and early 1990s[82]. But due to efficiency of energy conversion and poor performance of the materials available at that time, the interest faded away.

Recent demand from aerospace, automotive and oil and gas industries to compact and high power actuators revived the interest to the field of actuation fatigue.

Despite its importance, crack growth characteristics during thermal cycling under stress has not been studied systematically. There are only a few reports on crack growth behavior during thermal cycling in NiMnGa [83] and NiTi [84]. The reason of crack growth during thermal cycling was also studied by finite element analysis with the conclusion that the crack should mostly grow during cooling due to unfavorable stress redistribution as a result of the phase transformation [85–87].

2.4 Fracture of Shape Memory Alloys

The determination of fracture toughness of SMAs is a challenging problem due to the unique temperature dependent stress-strain behavior of SMAs. When the material is in martensitic state, the first deviation from the linearity in the stress-strain response corresponds to martensite reorientation and when the material is austenitic and the temperature is below M_d, the first non-linearity corresponds to the onset of stress induced martensitic transformation. In either case, the stress levels are much below the actual plastic yield point of the materials. ASTM E1820 describes the standards regarding the fracture toughness measurements including linear elastic and elasto-plastic analysis. The norm in the literature is to use linear elastic fracture mechanics (LEFM) analysis [88–91]. If the first non-linearity is used as yield stress, as defined in the standard, the minimum dimensions for LEFM approach to be valid become prohibitively large. The studies reporting fracture toughness values for SMAs acknowledge this fact and report obtained

values using the samples with dimensions below the minimum dimensions required by LEFM approach [88,89]. Elasto-plastic analysis of SMA fracture toughness is recommended in several articles [92,93] but experimental results are not currently present. There is a hybrid approach using linear elastic fracture calculations and crack growth (resistance curves with K) [68,90].

3. MATERIALS AND METHODS

This section contains details about initial materials, their processing history as well as experimental methods for mechanical, thermo-mechanical characterization and imaging used throughout the present study.

3.1 Materials

Three different compositions used in this study: $Ni_{50.7}Ti_{49.3}$, $Ni_{50.3}Ti_{29.7}Hf_{20}$ and $Ni_{49.5}Ti_{50.5}$. Details of these materials including processing history and selected heat treatments can be found in what follows.

3.1.1 $Ni_{50.7}Ti_{49.3}$

Slightly nickel rich, binary NiTi with the composition of 50.7 at. % Ni and 49.3 at. % Ti obtained from SAES Getters. Vacuum induction melting (VIM) was used to fabricate the material. Subsequently cast ingots were hot rolled.

Because the composition of Ni is beyond the solubility limit at room temperature, the material has the ability to show precipitation hardening. In order to establish a baseline behavior, this material was solutionized at 800 °C for 1 hr followed by water quenching. Samples were encapsulated in borosilicate glass tubes under vacuum to prevent oxidation during heat treatments. 3 different precipitation heat treatments were applied to the solution heat treated samples. Those heat treatments were selected based on previous

experience. First one is the peak aged condition which is 300°C 100 hrs. This heat treatment yields nano-sized dispersed Ni_4Ti_3 precipitates with average width to be around 5 nm. Second one is a two-step aging performed by aging at 500°C 10 hrs and 400°C 24 hrs. This heat treatment yields to sub-micron sized precipitates with anticipated bimodal precipitate size distribution. The mean precipitate width and length were measured to be 0.21 and 0.97 μm respectively. Third one is furnace cooling done by cooling from 550 °C to 100 °C in 100 hrs. This heat treatment yields to micron sized precipitates. The mean and standard deviation of the precipitate width and length were measured to be 0.36 ± 0.10 and 1.39 ± 0.62 μm respectively. Microstructures after each precipitation heat treatments can be seen in Figure 3.1. Transformation temperatures after each heat treatment was measured by DSC and the results can be seen in Table 3.1.

Grain size of the material after each heat treatment was measured with average grain intercept method and can be seen in Table 3.1. Note that there are small differences between different heat treatments but they are within the standard deviation of the experimental scattering. The average grain size for this material is 74 ±18 μm.

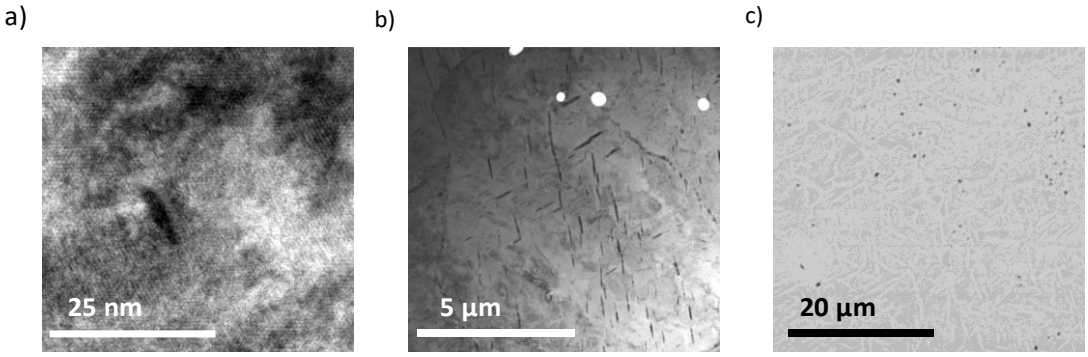

Figure 3.1 Microstructure of $Ni_{50.7}Ti_{49.3}$. a) Ni_4Ti_3 precipitate (darker shade) size and shape can be seen on 300 °C 100 hrs aged material. Image captured by high resolution, high magnification bright field TEM. b) Precipitate size and distribution on two step aged (500 °C 10 hrs and 400 °C 24 hrs) microstructure. Image captured by lower magnification bright field TEM. Darker shaded lenticular features are Ni_4Ti_3 precipitates where white circular features are carbides. c) Precipitate size and distribution on furnace cooled (550 °C to 100 °C in 100 hrs) microstructure. Image captured by back scattered electron mode on SEM. Lighter shaded lenticular features are Ni_4Ti_3 precipitates where black circular features are carbides.

3.1.2 $Ni_{50.3}Ti_{19.7}Hf_{20}$

Slightly Ni rich, NiTiHf ternary high temperature shape memory alloy used in this study was acquired from NASA Glenn Research center. The material has composition of 50.3 at. % Ni, 19.7 at. % Ti and 20 at. % Hf. The material was fabricated by VIM method and hot extruded.

Table 3.1 Summary of heat treatments with parameters, grain size, and transformation temperatures on $Ni_{50.7}Ti_{49.3}$.

Heat Treatment Type	**Heat Treatment Parameters**	**Grain Size (μm)**	**Transformation Temperatures (°C)**			
			M_f	**M_s**	**A_s**	**A_f**
Solution Heat Treatment (SHT)	800 °C 1 hr + WQ	80 ± 16	-21.4	-2.4	12.0	33.6
Peak Aging	300 °C 100 hrs +WQ	60 ± 19	-28.0	-2.3	52.3	61.1
Two Step Aging	500 °C 10 hrs + WQ 400 °C 24 hrs + WQ	90 ± 19	22.4	36.0	61.5	73.6
Furnace Cooling	550 °C 15 min + linearly cooling from 550 °C to 100 °C in 100 hrs + WQ	72 ± 11	-9.5	23.4	31.9	59.2

Three aging conditions were studied throughout this study. These aging heat treatments selected based on the previous systematic study by Evirgen et al. [27,94]. Several different versions of aging heat treatments were studied such as, aging in air or vacuum, and quenching vs air cooling. It was found that aging in air vs vacuum or quenching and air cooling did not create any significant difference. Thus starting with as received condition, aging in air and cooling in air was selected as condition for further considerations. Three aging heat treatment selected for this study are 550 °C 3 hrs, 600 °C

10 hrs and furnace cooling from 700 °C to 100 °C in 48 hrs. Transformation temperatures can be seen in Table 3.2. Microstructures after those heat treatments can be seen in TEM images in Figure 3.2 [94]. The average precipitate sizes were determined to be 5.2 ± 1.4, 22.8 ± 4.0, 31.8 ± 6.4 nm in width and 10.1 ± 3.5, 46.6 ± 9.3, 132.7 ± 39.1 nm in length for peak aged, over aged and furnace cooled conditions respectively.

Table 3.2 Summary of heat treatments with parameters and transformation temperatures on $Ni_{50.3}Ti_{19.7}Hf_{20}$.

Heat Treatment Type	**Heat Treatment Parameters**	**Transformation Temperatures (°C)**			
		M_f	**M_s**	**A_s**	**A_f**
Peak Aging	550 °C 3 hrs	121.6	153.7	151.0	176.3
Over Aging	600 °C 10 hrs	141.5	181.1	185.1	220.3
Furnace Cooling	700 °C 15 min + linearly cooling from 700 °C to 100 °C in 48 hrs + WQ	161.8	213.9	213.2	269.0

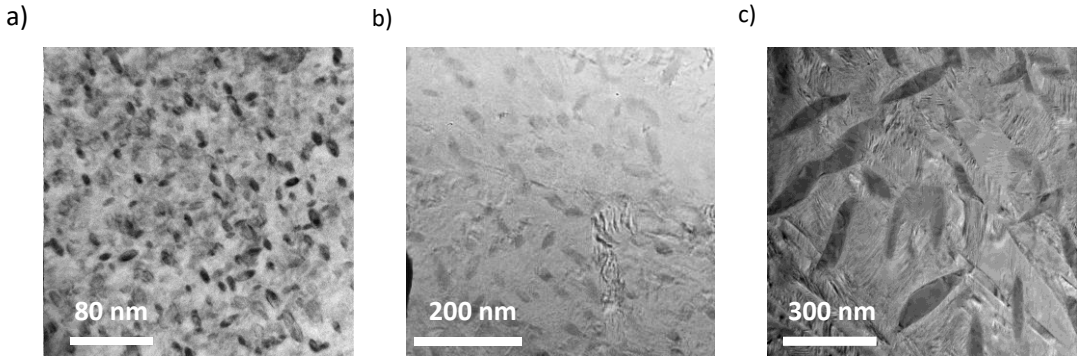

Figure 3.2 Bright field transmission electron microscopy images of all heat treatments studied in this work a) Precipitate size and distribution of peak aged (550 °C 3 hrs) condition. [94] b) Precipitate size and distribution of over aged (600 °C 10 hrs) condition. c) Precipitate size and distribution of furnace cooled condition (700 °C to 100 °C in 48 hrs). In all images darker shades represents H phase precipitates [94].

Because the NiTiHf material is martensitic at room temperature determining grain size is not possible with regular approach. However, after thermo-mechanical cycling grains became visible on optical microscopy studies. Based on those images grain size of 550 °C 3 hrs heat treated material is 143 µm calculated by using average grain intercept method.

3.1.3 $Ni_{49.5}Ti_{50.5}$

Slightly Ti rich NiTi is used in this study to be an alternative to Ni rich binary NiTi with higher transformation temperatures. The material used in this study was obtained from ATI and had composition of 49.5 at. % Ni and 50.5 at. % Ti. It was melted by VIM/VAR method and rotary forged at 800 °C followed by air cooling.

No aging or annealing is done on this material. Since the material is not precipitation hardenable, the aging heat treatment is not applicable. Moreover, because processing history of material does not include cold working annealing is not applicable either. Transformation temperatures of the material was measured by DSC and found to be 45.0, 71.3, 84.0 and 112.3 °C for M_f, M_s, A_s, and A_f respectively.

3.2 Experimental Methods

Details of experimental methods including description of setups, procedures, sample size and geometry can be found in this section. Some of the experiments were well defined and guidelines for them exist as ASTM standards. On the other hand, some of the experiments were novel and procedures are self-generated. Moreover to run some of those novel tests there are no commercially available test systems exist. Several custom made test systems were developed and their detail can be found in the following subsections.

3.2.1 Monotonic Tension Tests

Tension tests were conducted using MTS 312.31 equipment. Displacement was used as the control mode in monotonic tension tests. The strain rate was set to be $5\ 10^{-4}$ mm/mm.s obtained by constant displacement rate of $4\ 10^{-3}$ mm/s. In this study modified flat dog bone samples which were shown in Figure 3.3.a were used with gauge dimensions of 3 x 8 x 1 mm. Note that depending on material availability and polishing, the thickness may vary between 0.75 to 1.5 mm.

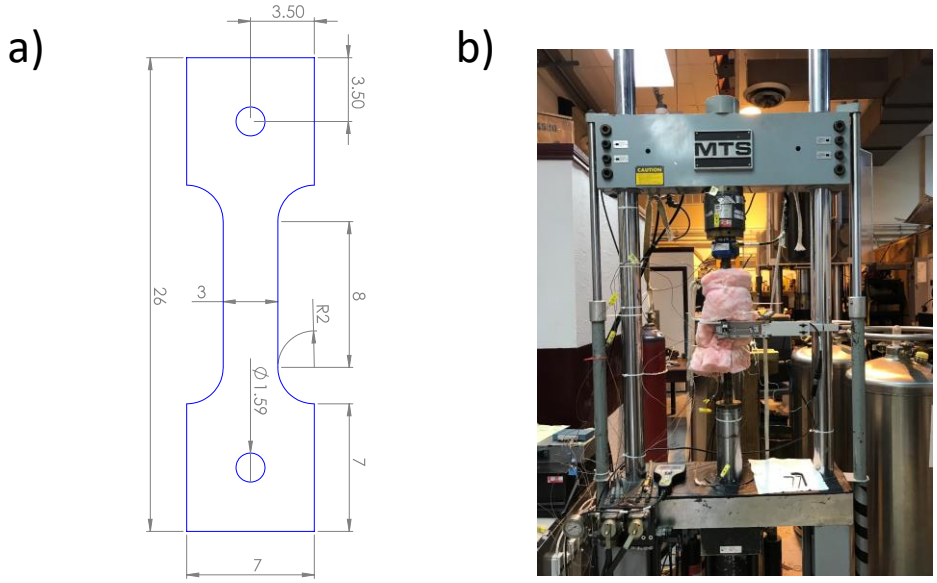

Figure 3.3 a) Technical drawing of flat dog bone samples used in monotonic tension, superelasticity, and isobaric heating cooling tests. All dimensions are in mm. Thickness can be anywhere between 0.75 mm to 1.5 mm b) Picture of servo-hydraulic test frame (MTS 312.31).

MTS servo hydraulic test frame (shown in Figure 3.3.b) was used for testing with grips that are equipped with heating and cooling elements to control temperatures. Temperature was controlled by two PID temperature controllers one for each grip.

3.2.2 Charpy Impact Toughness Tests

Charpy tests were conducted to measure energy required to fracture material under high strain rates. This method is extensively used to determine effect of temperature on the toughness of metals most notably steels. The ASTM standard E23 defines and describes details of such tests. Specimen size and geometry used in this test can be seen

in Figure 3.4.a. Note that this size is smaller than those specified in the standard which is 10x10x55 mm for width, thickness and length respectively. The ASTM E23 standard acknowledges in section A3.1 that; if the material availability is limited, smaller samples can be used. In that case, the size of the tested specimen should be clearly noted and the values obtained by sub-size specimen shouldn't be compared with full sized samples. It is however permitted to compare the values among the same sized specimen.

A commercial test system named Impactor II (shown in Figure 3.4.b) by CEAST (Pianezza, Italy [now part of Instron, MA USA]) was used in this study. This device is instrumented which means that it has load cells which can provide force displacement data throughout the test duration. Sample temperature was controlled by timing. Temperature control by timing can be described as follows. For lower than room temperature tests, a representative sample, which has a spot welded thermocouple on the other side of the notch, was dipped in liquid nitrogen. After its temperature was stabilized, it was taken out from the liquid and placed in the system. While this happens the temperature of the sample was periodically recorded. After this profiling is repeated 3 times, a time-temperature function was generated. This makes it possible to set a time for desired temperature. Similarly for higher than room temperature tests, a hot plate is used with a set temperature to establish starting temperature. Later, time-temperature function was determined.

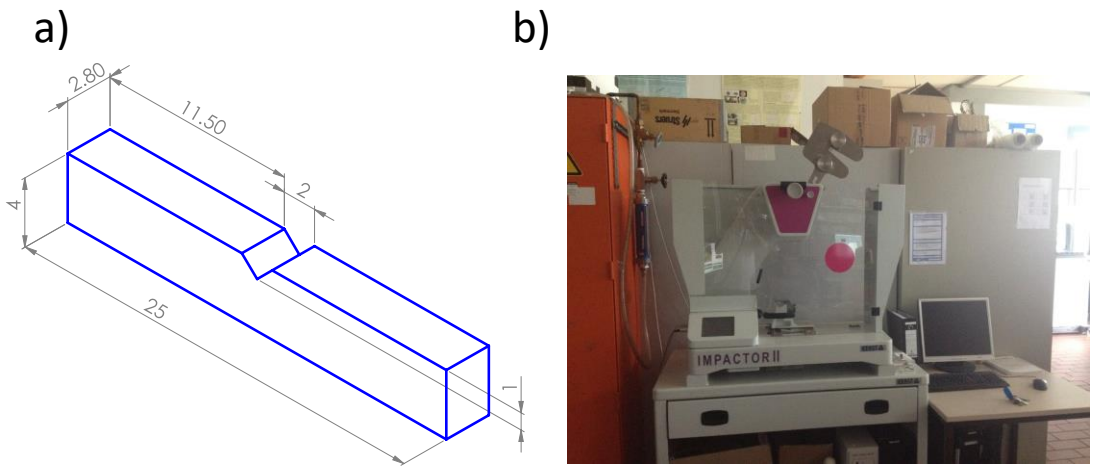

Figure 3.4 a) Technical drawing of Charpy impact test sample. All dimensions are in mm. b) Picture of Charpy impact toughness test system "Impactor II".

3.2.3 Determination of Shape Memory Alloy Properties

Shape memory alloys have several distinct material properties which are not defined for other structural or active materials. Those properties include critical transformation temperatures such as M_f, M_s, A_s, and A_f at no load or under stress, critical stresses such as onset of stress induced martensitic transformation, critical strains such as transformation strain, actuation strain, irrecoverable strain. Definitions of aforementioned properties as well as methods to measure them can be found in this section.

3.2.3.1 Isobaric Heating-Cooling Tests

Isobaric heating cooling or load biased thermal cycling experiments are one of the most basic SMA property determination tests used. Currently, there is no published ASTM standard for it. But there is a work item being considered by ASTM committee E08.05 with work item number WK55902. In this study an MTS servo hydraulic test frame equipped with heating and cooling systems was used. The system was same with the one described in section 3.2.1 and shown in Figure 3.3.b. Similar to tension tests, flat dog-bone tension samples with dimensions and shape given in Figure 3.3.a was used.

A schematic showing a typical isobaric heating cooling cycle can be seen in Figure 3.5. Some parameters such as strain in martensite, strain in austenite and actuation strain is also used in actuation fatigue since actuation fatigue is repetitive isobaric heating cooling cycles.

Isobaric heating cooling test procedure is as follows: the sample is heated to a temperature above A_f which is called upper cycle temperature (UCT). Typical value for UCT is A_f+ 50 °C but can change depending on the stress range. After sample reaches to the desired temperature, stress is being increased to a set value and force is kept constant throughout the cycle. Heating and cooling rates were set to be 10 °C per minute to ensure thermal homogeneity in gauge section of the samples. A typical isobaric heating cooling test includes one cycle per stress level but multiple cycles were also done in the current study.

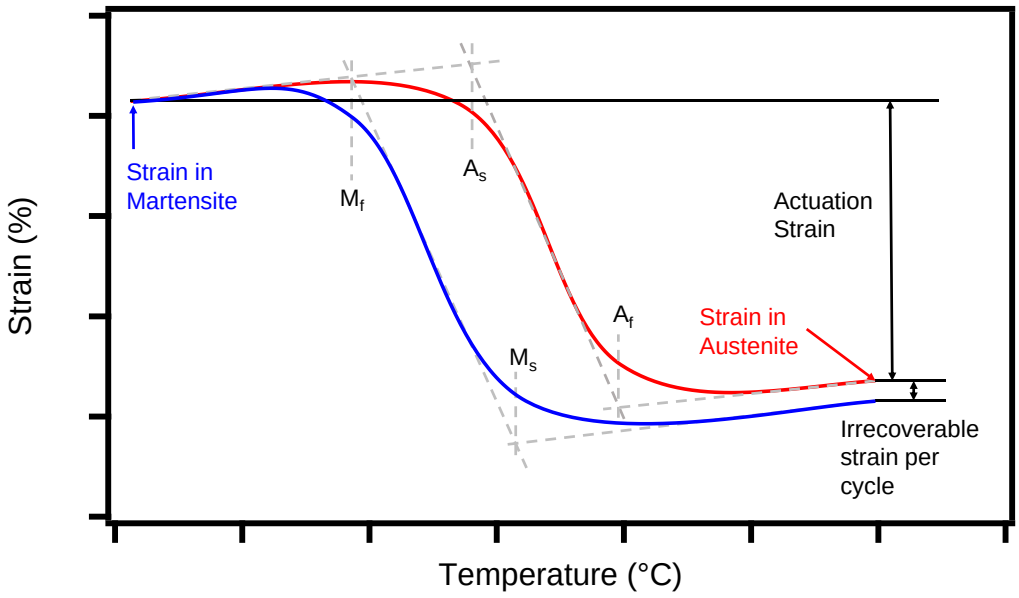

Figure 3.5 Schematic of an isobaric heating cooling test. In actuation fatigue same response is also obtained.

Transformation temperatures under stress were measured by tangent method. This method requires the determination of linear region during transformation both during martensite to austenite transformation and austenite to martensite one. Later a tangent is drawn from the linear region. Once the transformation is completed, material shows non-hysteretic linear regions that are dominated by thermal expansion. Two tangents are also drawn from those regions. The intersections of those lines signify, critical transformation temperatures under stress. The graphical representation of this method can be seen in Figure 3.5. There are other ways to measure strain due to phase transformation and often the strain due the phase transformation is called “transformation strain” but for this study

an end to end approach is chosen for simplicity and because it better represent a real actuator in service. In order to differentiate from the values reported in literature a new term is used which is “actuation strain”. Also note that critical strain points were marked namely the strain at lower cycle temperature (LCT) “strain in martensite” and the strain at UCT “strain in austenite”. The difference between those two values are “actuation strain”. The irrecoverable strain was also marked which is measured between start of the thermal cycle at UCT and at the end of it at again same temperature.

It is known that transformation temperatures increase with increasing stress. This phenomena is based on the thermodynamics law quantified by Clausius-Clapeyron equation. A phase diagram of austenite and martensitic transformation with respect to temperature and strain can be generated using isobaric heating cooling tests as well as superelasticity tests. Although ideally those two methods should yield to exact same phase diagram, due to complex nature of shape memory alloys such as tension-compression asymmetry, transformation induced plasticity, anisotropy in mechanical properties of martensite and austenite can yield notable differences. Therefore, it is important to characterize the material with the same route of its anticipated application.

3.2.3.2 Superelasticity Tests

Superelasticity or pseudoelasticity is a phenomenon in SMAs that happen at temperatures above A_f and below M_d. ASTM standard F2516 defines and describes details of such tests. Same test system and sample geometry described in 3.2.1 used to do these experiments.

Procedurally, it includes heating up to the desired temperature, loading the material to a predefined strain level by displacement control, unloading to zero stress by force control and repeating with higher strain levels until fracture. In the ASTM standard, it is recommended to run these tests in one step with strain set to 6 % and zero force is defined as any value lower than 7 MPa. In the current study multiple steps were utilized with step size of 1 % used unless otherwise stated.

A schematic of a superelastic test and the critical values obtained is shown in Figure 3.6. ASTM standard suggests reporting upper plateau strength (UPS) at 3 % strain during loading and lower plateau strength (LPS) at 2.5% strain during unloading. Another method to quantify stress where transformation starts is using 0.2% intersection of the parallel line to elastic modulus that is offset for 0.2 % and stress-strain diagram and it is called stress induced martensitic transformation stress (σ_{sim}). Note that σ_{sim} is upper bounded by UPS and can be very close if the transformation is sharp and can be significantly lower if it happens at a wide range. Upper and lower plateau stresses are more relevant for the materials with low or no hardening during transformation on the other hand when there is significant hardening σ_{sim} is more relevant.

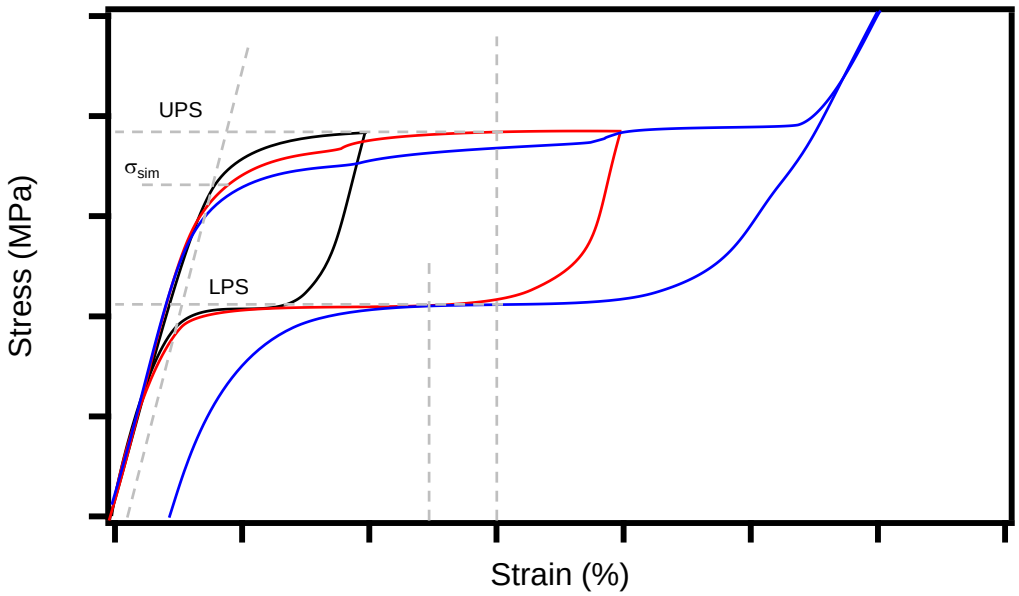

Figure 3.6 Schematic of superelastic test result with critical stress points, upper plateau stress (UPS), lower plateau stress (LPS) and critical stress for stress induced martensitic transformation (σ_{sim})

3.2.3.3 Differential Scanning Calorimetry

Differential scanning calorimetry (DSC) is a method to determine heat flow from and to a material during thermal sweeping. It is widely used in SMAs to determine transformation temperatures since martensitic transformation is a first order transformation in other words it has enthalpy of transformation. Austenite to martensite transformation is exothermic which means it releases heat to the surrounding. Martensite to austenite transformation endothermic in other words absorbs heat from the surrounding. ASTM F2005 defines differential scanning calorimetry procedure and how to extract critical temperatures from it. Critical transformation temperatures M_f, M_s, A_s, and A_f are

determined by intersection of tangents of transformation peak and flat sections as shown in Figure 3.7.

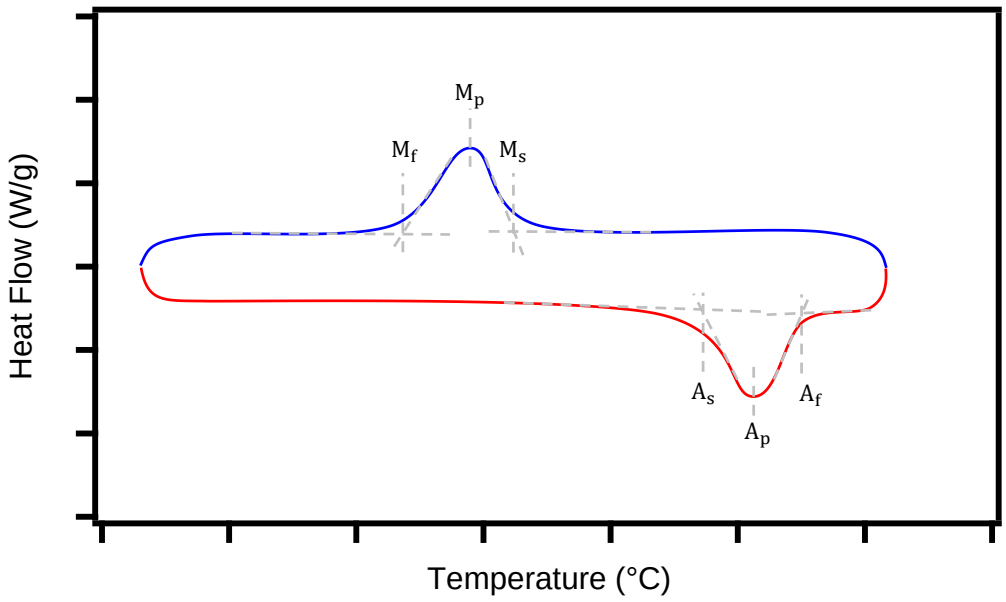

Figure 3.7 Schematic of differential scanning calorimetry results showing critical transformation temperatures

Thermal Analysis Q2000 differential scanning calorimeter was used in this research. Heating and cooling rate was set to be 10 °C per minute. Sample size can be varied but kept small enough to fit 5 mm diameter aluminum pan which is used with the calorimeter. Thickness is kept below 1.5 mm. Typical sample is 3 mm diameter disk with 1 mm thickness. Samples were polished and etched before DSC test to remove EDM recast layer and oxide layer to prevent those layer to interfere with transformation.

3.2.4 Actuation Fatigue Testing

Actuation fatigue or thermo-mechanical fatigue is relatively new procedure, thus there is no ASTM standard on such testing. It involves thermal cycling under constant stress or stress as a function of displacement such as spring loading.

In this study custom made fatigue testing systems were used. Two stress states were considered for this work, namely tensile and shear. Details on test systems and experimental procedures can be found in the following sections.

3.2.4.1 Tensile Actuation Fatigue Testing

Tensile actuation fatigue testing were done on flat dog bone samples that are shown in Figure 3.8. Testing system had major improvements through the length of the study thus it could be possible to divide testing system into versions.

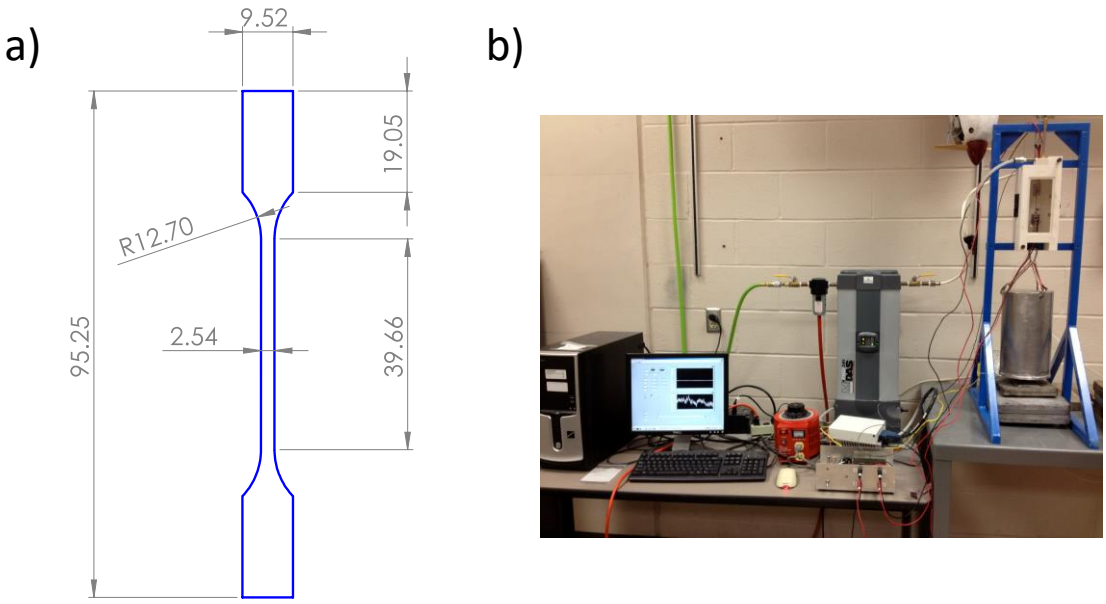

Figure 3.8 a) Technical drawing of flat dog bone samples used in tension actuation fatigue tests. All dimensions are in mm. Thickness can be anywhere between 0.75 mm to 1.5 mm b) Picture of custom made actuation fatigue testing system.

First version had an environmental chamber made by 3D printed ABS box by Stratasys FDM360. It has an opening at the back for displacement sensor connection, and a polycarbonate window in front for visual inspection. The environmental chamber includes two vortex cooling tubes. When pressurized air passes through vortex cooling tubes one end of the tube blows cold air and the other end (exhaust) blows hot air. With the configuration in the system the chamber temperature was kept constant at -20 °C. Heating was done by Joule heating in other words direct current application to the samples. A variable transformer (Variac) is used as power source. Cycle control was achieved by time control. Current was let pass through the sample for a predetermined duration.

Subsequently the sample let cool down in the environmental chamber. The cooling segment of thermal cycle is also terminated by time control. Heating and cooling times are determined by several cycles in the beginning of the test. Because attaching a contact based thermal measurement device such as thermo-couple creates thermal inhomogeneity in the gauge section of the samples, real time temperature data was absent on the first version of the actuation fatigue frame. Displacement was measured by linear variable differential transformer (LVDT) from bottom grip of the material by the help of an extension which is called LVDT arm. Application and cut of the current was controlled by a Labview program as well as data acquisition.

In the second version of the actuation fatigue frame, an infrared (IR) thermometer (Micro-Epsilon (Ortenbug, Germany) CTL-CF1-C3) with laser crosshair for aiming was used for real time temperature measurements. Specified spot size for temperature measurement is 0.9 mm diameter. Through the real-time temperature feedback, it became possible to control cycling with temperature thresholds. In this version, heating segment was ended when temperature reaches to specified value. Likewise during cooling current was not applied until temperature reaches to a specified value. Because polycarbonate window of environmental chamber interferes with infrared measurement front cover of environmental chamber was removed. Also because high temperature shape memory alloys were tested with this version of the system, vortex cooling tubes and environmental chamber was not required.

In third version of the system, to test binary NiTi SMAs environmental chamber was re-assembled. A window was cut from environmental chamber not to interfere with

IR thermometer. Similar to second version, real time thermal measurement and temperature target control was employed.

Data obtained from tension actuation fatigue testing is presented in 3 different types. The strain-temperature plots show transformation temperatures and accumulated plastic deformation similar to isobaric heating cooling tests. A schematic of them can be seen in Figure 3.5. In addition to strain-temperature graphs critical strains (strain in martensite, strain in austenite and actuation strain) are also plot against number of cycles. Those plots help to demonstrate evolution of critical strains with number of cycles. A schematic of critical strains-number of cycles plot can be seen in Figure 3.9.a. Lastly, to compare different heat treatments and compositions, work output- fatigue life plots are presented. Smith-Watson-Topper fatigue law states a power law correlation as shown in Equation 2.9. A schematic of such plots can be seen in Figure 3.9.b.

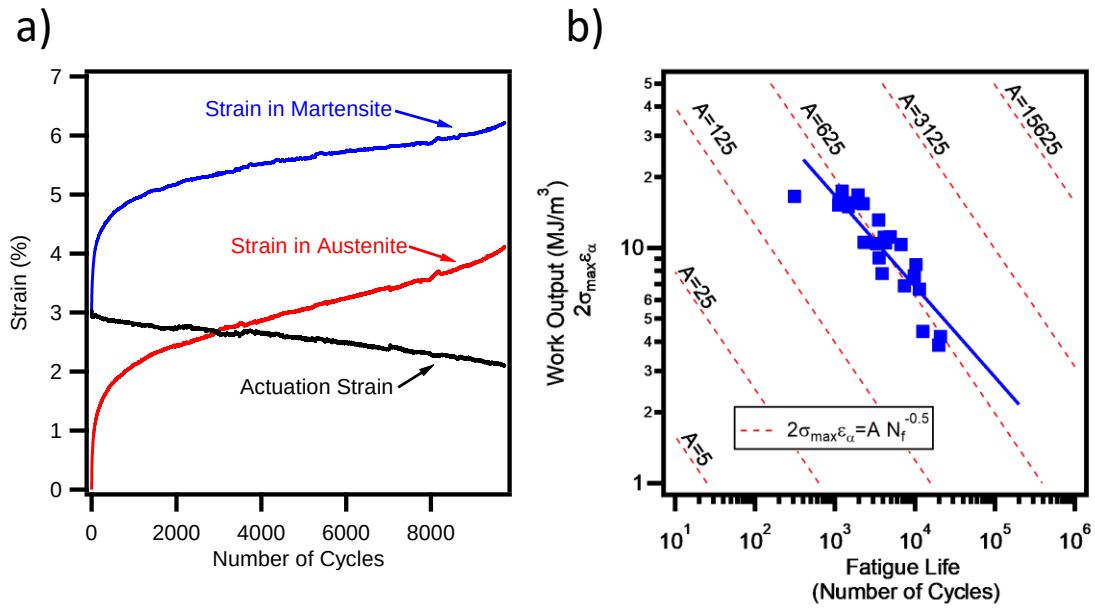

Figure 3.9 Schematics of data obtained from life based actuation fatigue testing. a) Critical strains as a function of number of cycles plots. Those plots are useful to determine stability and evolution of strains as test progress. b) Work-output as a function of fatigue life plots. The construction of the plot is inspired by Smith-Watson-Topper approach where Y axis is work output and X axis is fatigue life.

3.2.4.2 Shear Actuation Fatigue Testing

To study the effects of stress mode on extended thermal cycling and fatigue, SMAs were tested on a custom made fatigue testing system. Similar to tensile version there is no ASTM standard on thermal cycling under constant shear stress. Pure shear was applied to SMA samples by using hallow cylindrical samples which are called torque tubes.

Custom made external (placed the outer surface of the tubes) heating elements were used to heat up the samples. Heaters made out of chromel wire were shaped into helixes with varying winding frequencies. To compensate heat losses at the ends of the

tubes winding frequency was increased. The cooling was assisted by 5.5 cm diameter fans placed in each side of the tube. In the first version, the temperature is controlled by Omega N8200 proportional-integral-derivative (PID) temperature controller. In the heating channel, the PID controller opens and closes the current to the heating element. Heating element is powered by Variac. Rotation is measured from the center of the loading pulley by a potentiometer. Potentiometer is excited to 10 volts which is also measured and monitored through the test for normalization. Potential to rotation conversion function obtained by calibrating known rotations and voltages and matches well to the specifications of potentiometer. Data collection is done by Measurement Computing USB-TC data acquisition (DAQ) board attached to a Labview program.

Specimens connected to the test system with EDM machined splines at each end. The spline geometry can be seen in Figure 3.10.c and 3.11.b. Splined region is 12.7 mm and is not considered in active length. Samples with two different wall thicknesses studied. Both of them have same outer diameter of 9.52 mm where thinner tubes have 6.86 mm inner diameter and thicker tubes have 5.79 mm. Technical drawings of two torque tube geometries can be seen in Figures 3.10 and 3.11. The system has one stationary end which is made out of glass phenolic polymer matrix composite. Other end is free to rotate but to keep system in balance supported by an array of ball bearings. Loading shaft is attached to the center of loading pulley. Dead loads are attached to the pulley to generate constant torque on the system. Picture of shear actuation fatigue testing system can be seen in Figure 3.10.a.

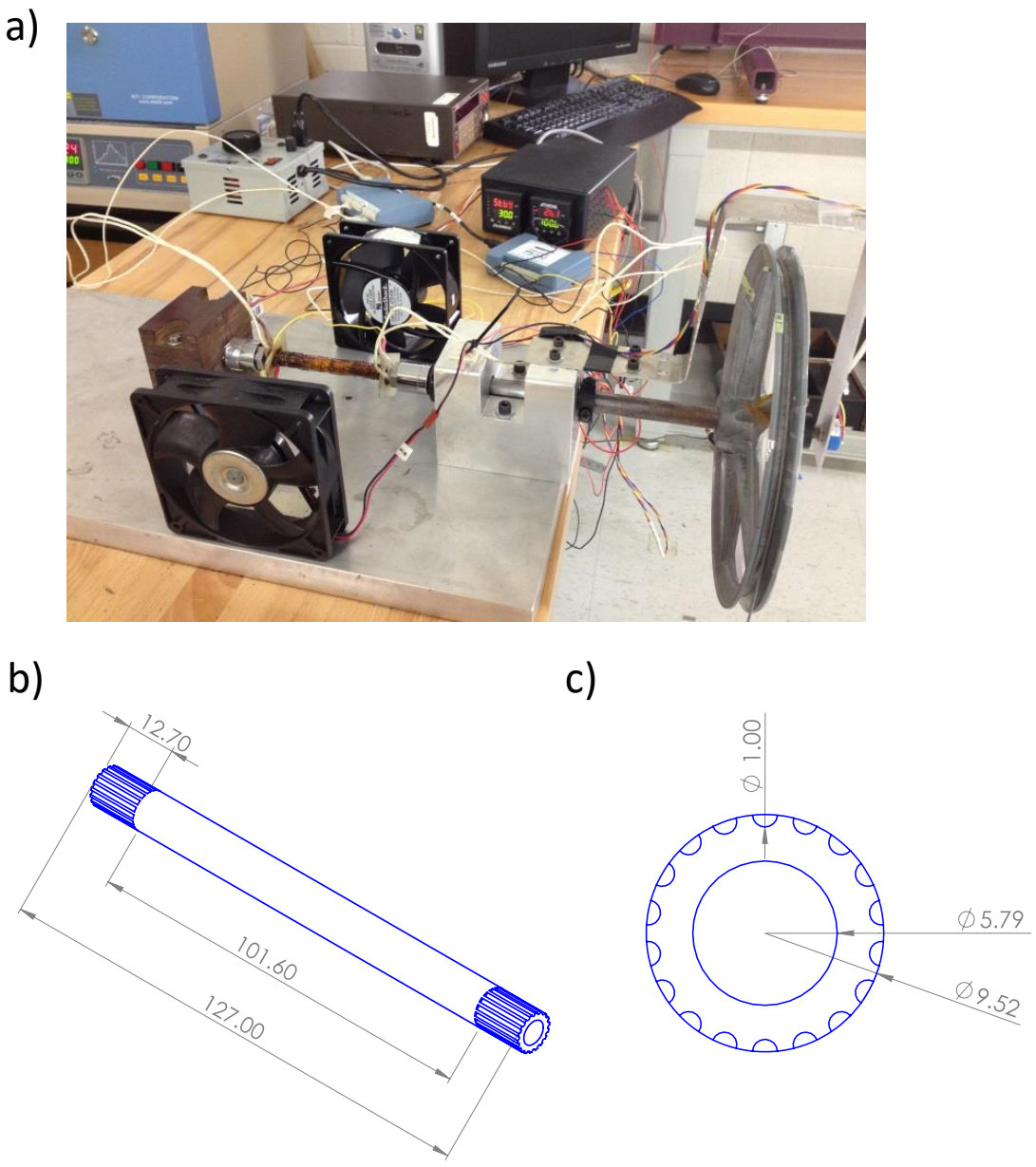

Figure 3.10 a) Picture of shear actuation fatigue system. b and c) Technical drawing of thick torque tubes used in this study.

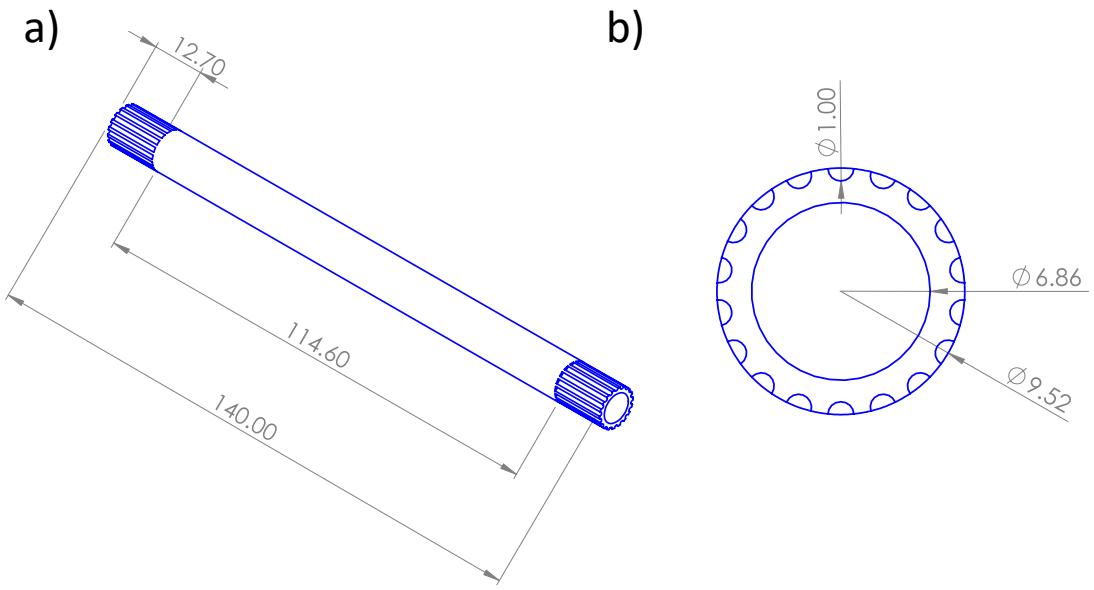

Figure 3.11 Technical drawing of thin torque tubes used in this study.

Stress reported in this study is calculated for outer surface of the tubes using the Equation 3.1.

$$\tau = \frac{Tr}{\frac{\pi}{32}(OD^4 - ID^4)} \qquad \text{eq. 3.1}$$

where τ is the shear stress, *T* is applied torque, *r* is the radius of the point of interest, OD is the outer diameter, and ID is the inner diameter. Similarly, the strains were taken as the outer surface strain of the tube and calculated using,

$$\gamma = \frac{\theta r}{L} \qquad \text{eq. 3.2}$$

where γ is the shear strain, θ is the rotation angle, and *L* is the active length of the tubes. Equations 3.1 and 3.2 were also used to calculate applied stress and strain of the torque tubes in similar studies [8,95,96].

3.2.5 Fracture Toughness Measurements

Fracture toughness can be defined as the resistance to crack growth and widely used in structural materials. ASTM standard E1820 defines and describes the details of tests to determine the fracture toughness. Compact tension and disk shaped compact tension samples used in this study. Sample sizes and technical drawings can be seen in Figure 3.12.

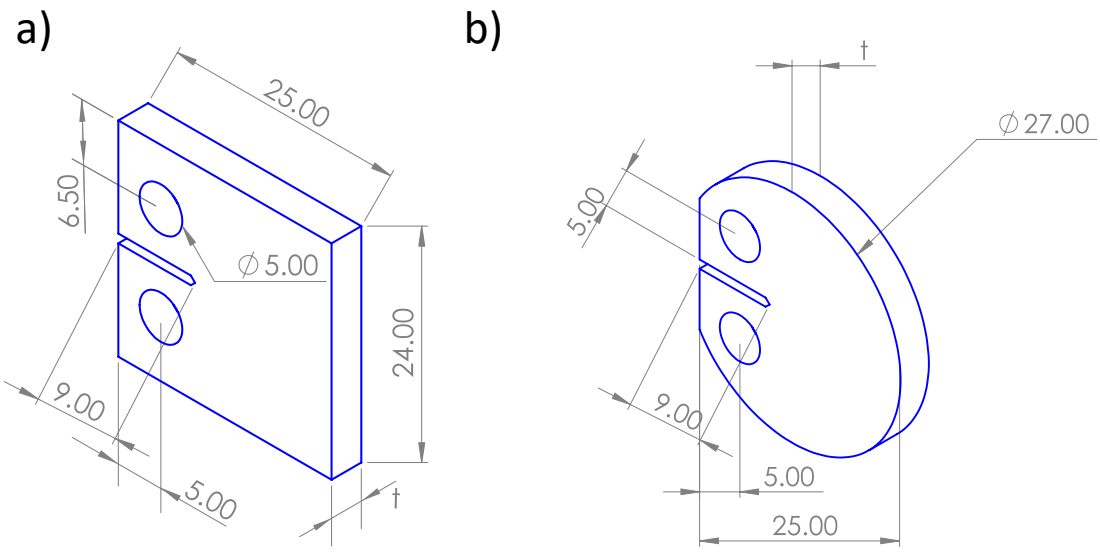

Figure 3.12 Technical drawing of fracture toughness samples.

The testing procedure can be summarized as follows. First, a fatigue pre-crack is introduced to have an atomistically sharp crack in the beginning of fracture toughness test.

The precracking stress intensity amplitude was selected as 9 MPa$\sqrt{\text{m}}$ with ratio (R) of 0.1, which means sample is cycled between 10 and 1 MPa$\sqrt{\text{m}}$. Precrack should be at least 1.3 mm and total crack length measured from the load line should be between 0.45 to 0.55 of width (W) of the sample which is 9 to 11 mm for samples studied in this work. The notch length is not specified in fracture toughness testing standard (ASTM E1820) but in crack growth testing standard (ASTM E647) it is suggested to be 0.20 of W which is 5 mm on this work.

Although testing procedure is almost identical, there are three distinct approach to process data. First one is linear elastic fracture mechanics. This approach threats the material a linear elastic medium with no plastic deformation. The conversion between boundary and macroscopic variables such as force and sample size and geometry parameters to crack tip stress intensity factor done by Equation 3.3 where P is force B is thickness, B_N is the thickness at notch plane (in case of samples with no side grooves B=B_N), W is width, a is the crack length and f $\left(\frac{\text{a}}{\text{W}}\right)$ is a function of crack length and width and given in Equations 3.4 and 3.5 for compact tension and disc shaped compact tension samples respectively.

$$K = \frac{P}{(BB_N W)^{\frac{1}{2}}} f\left(\frac{a}{W}\right) \qquad \text{eq. 3.3}$$

$$f\left(\frac{a}{W}\right) = \frac{\left\{\left(2+\frac{a}{W}\right)\left[0.886+4.64\left(\frac{a}{W}\right)-13.32\left(\frac{a}{W}\right)^2+14.72\left(\frac{a}{W}\right)^3-5.6\left(\frac{a}{W}\right)^4\right]\right\}}{\left(1-\frac{a}{W}\right)^{3/2}} \qquad \text{eq. 3.4}$$

$$f\left(\frac{a}{W}\right) = \frac{\left\{\left(2+\frac{a}{W}\right)\left[0.76+4.8\left(\frac{a}{W}\right)-11.58\left(\frac{a}{W}\right)^2+11.43\left(\frac{a}{W}\right)^3-4.08\left(\frac{a}{W}\right)^4\right]\right\}}{\left(1-\frac{a}{W}\right)^{3/2}} \qquad \text{eq. 3.5}$$

For a test to be qualified by ASTM standards as material property the test data should satisfy several conditions. First condition is related to the shape of force displacement curves. The tentative fracture toughness value is called K_Q and it is calculated at the force level of P_Q. To determine P_Q, a tangent is drawn from the initial linear region of load displacement plot and another line initiating from the same start point but with 95% of the slop which is called "95% secant line", P_Q is the maximum force within the envelop of tangent and 95% secant line. In the case of monotonically increasing behavior in those region (as can be seen in the left curve of Figure 3.13), P_Q is the intersection of 95% secant line and force displacement curve. When there is a local maxima in aforementioned envelope that maximum is treated as P_Q. P_{max} is the global maximum force obtained during the test. The ratio of P_{max} to P_Q must be lower than 1.10 for K_Q to be qualified as K_{IC}. Note that it is customary for shape memory alloy literature to use P_{max} while calculating critical K values.

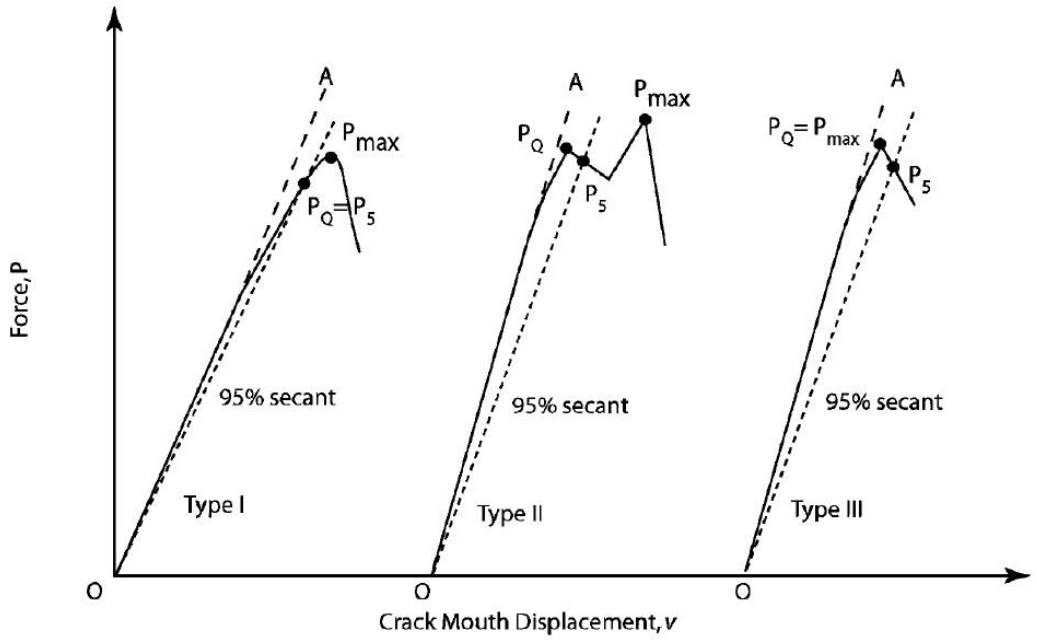

Figure 3.13 Schematic of force displacement curves during fracture toughness tests and determination of P_Q [97]

Second criteria that must be satisfied for K_Q to be qualified as K_{IC} is thickness and length of the unbroken ligament. Earlier versions of ASTM E1820 (2005 and before) specify both thickness and unbroken ligament with Equation 3.6 where b_0 is unbroken ligament, and σ_{ys} is yield stress. Newer versions of the same standard relaxed one of the constraints and just requires minimum length for unbroken ligament (b_0). In ideal geometry thickness should be half of width thus indirectly the constraint still exists but It was also appended that thinner samples could be tested.

$$b_o > 2.5 \left(\frac{K_Q}{\sigma_{ys}}\right)^2 \qquad \text{eq. 3.6}$$

Second way to process data to calculate fracture toughness is elasto plastic approach basic method. In this method, area under the force displacement curve and parallel to initial loading line is calculated and marked as A_{pl}. The schematic of calculation of A_{pl} can be seen in Figure 3.14. Later J value is calculated for any given point by using Equations 3.7. Where K is stress intensity factor calculated by Equation 3.3, *v* is poisons ratio, E is elastic modulus, B_N is thickness, b_0 is length of unbroken ligament, and η_{pl} is a function of unbroken and width as given in Equations 3.8.

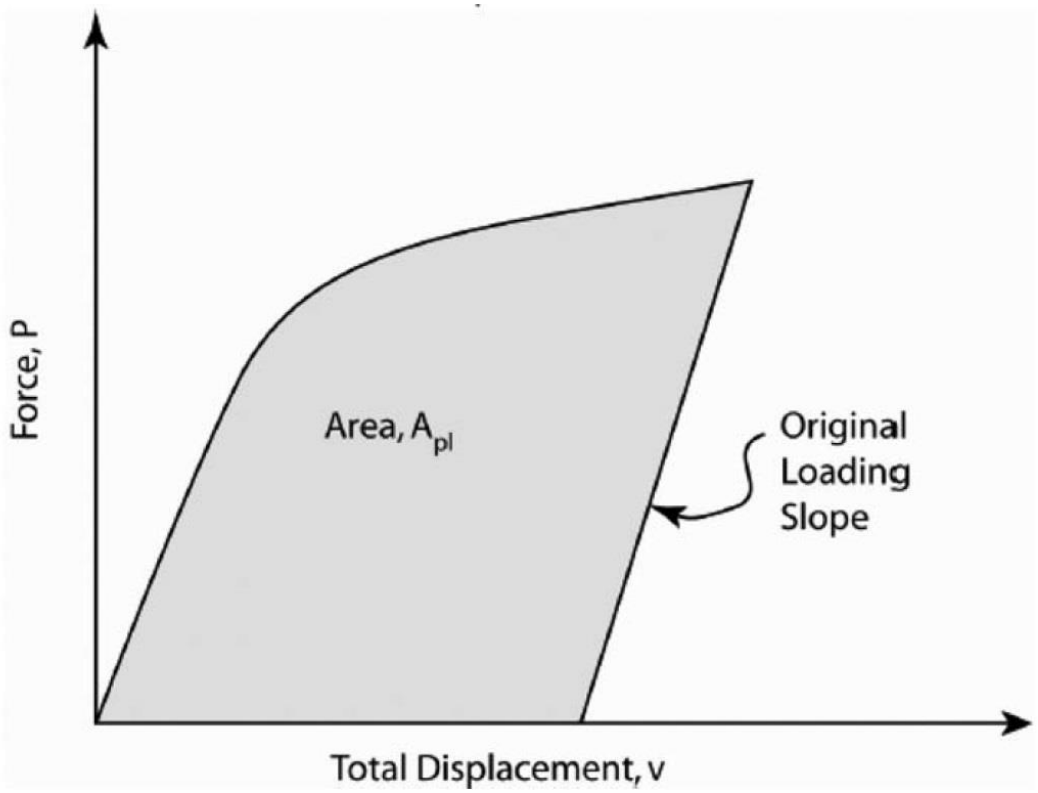

Figure 3.14 Calculation of A_{pl} for basic elasto plastic method [97]

$$J = \frac{K^2(1-v^2)}{E} + \frac{\eta_{pl} A_{pl}}{B_N b_o} \quad \text{eq. 3.7}$$

$$\eta_{pl} = 2 + 0.522 b_0/W \quad \text{eq. 3.8}$$

Maximum J can be calculated at maximum force. For calculated J integral values to be qualified as fracture toughness of the material they need to satisfy several criteria as listed. Accepted stable crack growth should be limited by following Equation 3.9. Minimum thickness (B) and length for unbroken ligament (b_0) is also specified by Equation 3.10. If the data satisfies given conditions, it is designated as J_C.

$$\Delta a_p < 0.2 + J_Q/2\sigma_Y \quad \text{eq. 3.9}$$

$$B, b_0 \geq 100\, J_Q/\sigma_Y \quad \text{eq. 3.10}$$

Last method used in this study is called elasto plastic approach R curve method. In this method constant monitoring of crack length is required. J integral is suggested to be calculated in an iterative manner shown in Equations 3.11 where $A_{pl(i)}$ is calculated by Equation 3.12 and schematically presented in Figure 3.15.a. Note that v_{pl} is plastic displacement not poison's ratio and it is calculated by Equation 3.13 where v is total displacement and C is the reciprocal of slope of force displacement curve during unloading.

$$J_{pl(i)} = \left[J_{pl(i-1)} + \left(\frac{\eta_{pl(i-1)}}{b_{(i-1)}}\right)\frac{A_{pl(i)} - A_{pl(i-1)}}{B_N}\right]\left[1 - \gamma_{(i-1)}\left(\frac{a_{(i)} - a_{(i-1)}}{b_{(i-1)}}\right)\right] \quad \text{eq. 3.11}$$

$$A_{pl(i)} = A_{pl(i-1)} + \frac{[P_{(i)} + P_{(i-1)}][v_{pl(i)} - v_{pl(i-1)}]}{2} \quad \text{eq. 3.12}$$

$$v_{pl(i)} = v_{(i)} - (P_{(i)} C_{(i)}) \quad \text{eq. 3.13}$$

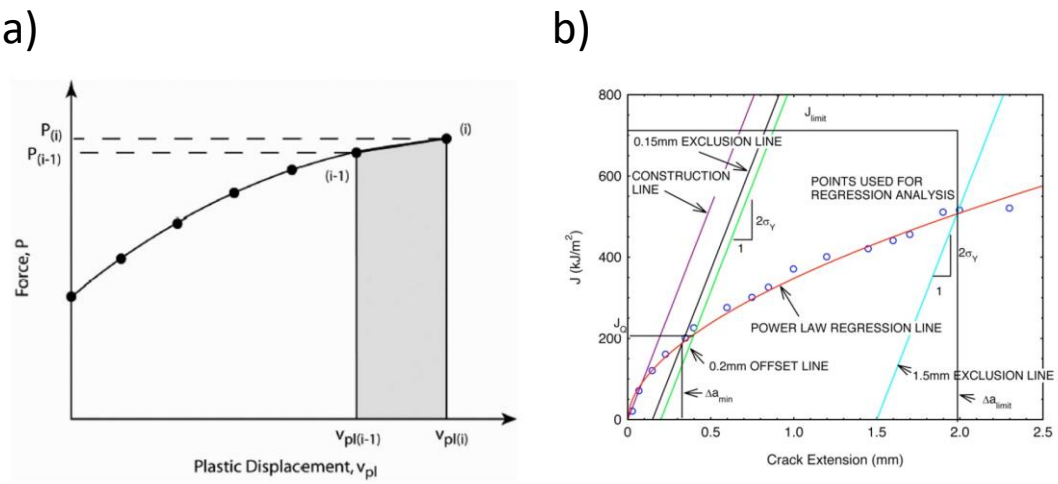

Figure 3.15 a) Schematic of calculation of A_{pl} where x is plastic component of displacement and y is force. b) Schematic of R curve where x is crack extension and y is J integral

Once incremental J integral values are calculated, they are plotted against crack extension as can be seen in Figure 3.15.b. Several lines are constructed such as construction line and their parallels (0.15, 0.2 and 1.5 mm exclusion lines), J_{limit} and Δa_{limit}.. Construction line has the slope of $2\sigma_y$, Δa_{limit} is vertical line drawn from the intersection of power law regression and 1.5 mm exclusion line, and J_{limit} is horizontal line calculated by Equation 3.14. The power regression of J integral and crack extension is calculated for data points in between 0.15 and 1.5 mm exclusion lines. The fracture toughness value is calculated from the intersection of regression line and 0.2 mm offset line.

Similar to other methods there are several conditions for measured value by R curve method to be qualified as material property in accordance with ASTM standard. First condition is related to number of data points within the range that is used for power

regression. It is stated that at least 8 data points must be present in this range. Second condition is related to thickness. Minimum thickness of unbroken ligament (b_0) and thickness (B) is given by Equation 3.14. It must be noted that the coefficient of equation 3.14 was 25 prior to 2008 which is when reduced to current value of 10. If the data satisfies given conditions the value is designated by as J_{IC}.

$$B, b_0 \geq 10\, J_Q/\sigma_Y \qquad \text{eq. 3.14}$$

Although three methods (optical, compliance and potential drop methods) are used in this study, the results reported are coming from compliance method.

3.2.6 Crack Growth Testing

Crack growth tests are essential for designing against fatigue with damage tolerant approach. The material behavior in cyclic mechanical loading was formulated by Paris' law. In the following two sub sections, details regarding to mechanical and actuation crack growth testing are presented.

3.2.6.1 Mechanical Crack Growth Testing

Crack growth during mechanical load cycling is defined by ASTM standard E647. Same samples and test setup used in section 3.2.6 are used in crack growth testing as well. Crack lengths were measured by potential drop method. Electrode locations with respect to sample can be seen in Figure 3.16. Note that a slightly different arrangement than ASTM suggested was used in this study. Since SMAs show phase transformation at superelastic region and martensite reorientation at martensitic region which shows

significant anisotropy, calibration between voltage and crack length determined by comparing measurement by optical image processing.

Stress intensity values (K) are calculated by using Equation 3.3. The material is cycled between two K values. The ratio between lower and higher K value is designated by R and the difference in between is designated by ΔK. In this study R value of 0.1 is used. After crack reaches to a predetermined crack growth, 1 mm in this work, stress intensity range (ΔK) is decreased and another step is done. Lastly, crack growth rates of each step is plotted against ΔK in a log-log scaled plot. The linear section of the data obeys the Paris law.

3.2.6.2 Thermo-Mechanical Crack Growth Testing

To the best of author's knowledge, actuation or thermo-mechanical crack growth testing in compact tension samples were done for the first time. Although there is no ASTM standard, mechanical crack growth standard was used for sample size and setup. Thermal cycling, is done by Roy 1500 induction heater controlled by Eurotherm 2200 PID temperature controller with analog output to control power proportionally. Cooling is done by assisted convection cooling by continuous air flow provided by 6" diameter fan. Temperature of the sample measured by 6 thermo-couples placed on marked locations in the figure. Mechanical data, such as force and load line displacement, acquisition is done by MTS multi-purpuse test suite program where temperatures and voltage recorded in Labview by Measurement Computing DAQ USB-TC and digital multimeter (Keithley 199 system DMM/Scanner) respectively. Constant current between electrodes provided

by Keithley 2231A-30-3 programmable power source with 3 channels. One channel is used for providing constant current where another channel is used to output crack length calculated from potential drop method. Crack length channel is connected to MTS controller through analog input channel for automation and safety purposes.

The testing procedure is as following; to get an atomically sharp crack in the beginning, mechanical fatigue precracking is done. Similar to fracture toughness test preckracking stress intensity factor amplitude was selected as 9 $MPa\sqrt{m}$ with ratio (R) of 0.1, which means sample is cycled between 10 and 1 $MPa\sqrt{m}$. The total crack length before thermal actuation starts set to be 6 mm. After precracking, sample is heated up to a value higher than A_f typically A_f +55 under zero force. Later sample is loaded to a predetermined force and the force kept constant throughout the test. Temperature is cycled with 10 minutes heating, followed by 2 minute wait at highest temperature, 10 minutes cooling and 8 minutes wait at the lowest temperature. Crack length is determined by optical image processing.

3.2.7 Imaging and Microstructural Characterization

Scanning electron microscopy (SEM) and transmission electron microscopy (TEM) were used in this study to investigate microstructure. Details regarding to procedures and equipment used in the following sections.

3.2.7.1 Scanning Electron Microscopy

Scanning electron microscopy is used to determine features from sub-micron size to macroscopic sizes. Those features include carbides and fracture surfaces. In this study FEI Quanta 600 is used. The SEM is equipped with energy dispersive spectroscopy (EDS), back scattered electron (BSE) detector in addition to secondary electron (SE) detector.

3.2.7.2 Transmission Electron Microscopy

Transmission electron microscopy is used to determine sub-micron and nano sized features such as precipitates, dislocations and fine twins. Transmission electron microscopy (TEM) investigation was conducted in a JEOL 2011 high-resolution microscope (in phase contrast mode) with a LaB6 filament, operated at 200 kV and equipped with an energy-dispersive X-ray (EDX) spectrometer. All the imaging has been done at room temperature. Specimens were machined by EDM into 3 mm diameter discs and mechanically polished to around 100 micron thickness. Lastly to obtain electron transparent zones, double jet electrochemical polishing used a 30% HNO_3 / 70% ethanol solution at -20 °C and 12 V. Bright field and dark field images were obtained to demonstrate precipitate and dislocation distribution. Selected area electron diffraction patterns (SAEDP) were obtained to identify phases and orientations of crystallites with each other.

3.2.8 X-Ray Diffraction

X-Ray diffraction (XRD) is used to determine crystal structure and constituency (presence of carbides, oxides, precipitates or two phase mixture of martensite and austenite) of the materials. Bruker D8 diffractometer with heating stage attachment was used for this study.

The phase constitution is also studied with XRD by using Rietweld analysis. Commercial Bruker Topas 3 software was used in those analyses.

3.2.9 Digital Image Correlation

To determine 2 dimensional strain distribution digital image correlation (DIC) was used. Images for DIC are captured by digital single lens reflex (DSLR) camera Cannon Rebel EOS 5. The processing is done with open source DIC software Ncorr 1.2 developed by J. Blaber et. al. [98]. Black background on samples obtained by high temperature spray paint. White speckle patterns applied by air brush with water based paint. The DIC pixel size is typically 40 microns.

4. EFFECT OF MICROSTRUCTURE ON TENSILE ACTUATION FATIGUE OF $Ni_{50.7}Ti_{49.3}$

4.1 Overview

In this section investigation on effect of microstructure on tensile actuation fatigue of $Ni_{50.7}Ti_{49.3}$ is presented. The microstructure is modified by precipitation, 4 microstructure are considered. Effect of surface finish was also considered which yielded to a major observation. Correlations between fatigue performance and easily measurable quasistatic and high strain rate mechanical properties are investigated. Lastly postmortem investigations were conducted to determine effect of microstructure and nucleation sites and reasons.

4.2 Introduction

Although effect of microstructure on mechanical fatigue performance of SMAs studied in systematical studies, similar work was lacking in literature for actuation fatigue. Lastly it is desired to establish correlations between easily measurable mechanical properties and actuation fatigue properties. That would provide insight on mechanism on actuation fatigue failure as well as make it possible to perform initial screening on materials to help design against fatigue. Specific aim of this work is to generate data to assess effect of microstructure and seek correlations between mechanical properties and actuation fatigue performance.

4.3 Experimental Procedure

Material described in section 3.1.1, was used in this study. In first part of the work 4 microstructures were considered. All those microstructures were products of different heat treatments which were decided based on previous experience. The table summarizing heat treatments can be seen in Table 4.1. Transformation temperatures after those heat treatments were also shown. Actuation fatigue tests were done on system described in section 3.2.4.1. Only one stress level was studied in this section which is 200 MPa. The first version of the system was used in this work, thus real time temperature data and information on upper and lower cycle temperatures were lacking. Sample surfaces were polished to a mirror like finish by mechanical polishing in the first part.

In the second part of the study those microstructures (4 heat treatments) were studied with third version of fatigue testing system and without polishing. Also 3 stress levels (200, 250 and 300 MPa) used in this work as opposed to only one (200 MPa) in the previous.

Table 4.1 List of heat treatments, description of microstructure and transformation temperatures obtained by DSC for nickel rich NiTi ($Ni_{50.7}Ti_{49.3}$)

Heat Treatment Type	**Heat Treatment Parameters**	**Resulting Microstructure**	**Transformation Temperatures (°C)**			
			M_f	**M_s**	**A_s**	**A_f**
Solution Heat Treatment (SHT)	800 °C 1 hr + WQ	No Ni_4Ti_3 Precipitates	-21.4	-2.4	12.0	33.6
Low Temperature Long Duration Aging	300 °C 100 hrs +WQ	Nano size coherent Ni_4Ti_3 precipitates	-28.0	-2.3	52.3	61.1
Two Step Aging	500 °C 10 hrs + WQ 400 °C 24 hrs + WQ	Micron size incoherent Ni_4Ti_3 precipitates	22.4	36.0	61.5	73.6
Furnace Cooling	550 °C 15 min + linearly cooling from 550 °C to 100 °C in 100 hrs + WQ		-9.5	23.4	31.9	59.2

4.4 Results

4.4.1 Actuation Fatigue of NiTi on Polished Samples

Summary of actuation fatigue results with key results (fatigue life, actuation strain, ratcheting at 100 cycle and at failure) can be seen in Table 4.2. It is observed that ratcheting increases the most in earlier stage of fatigue.

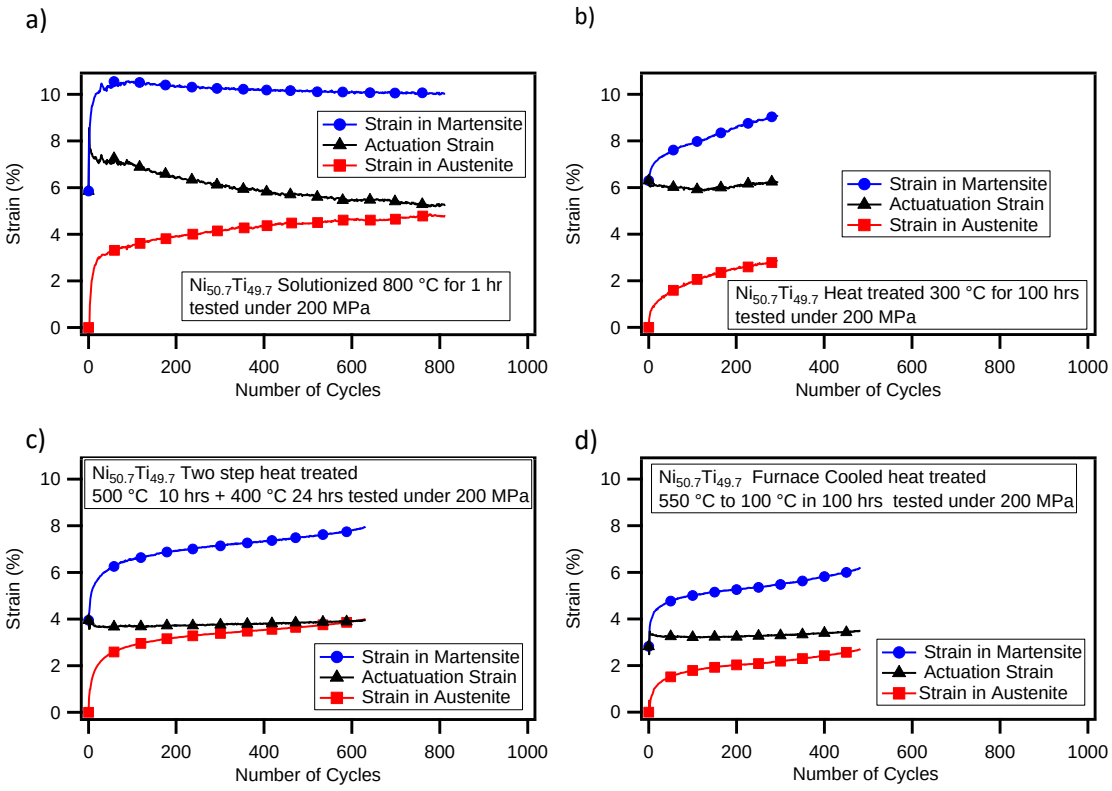

Figure 4.1 Evolution of strains with number of cycles for all microstructures of $Ni_{50.7}Ti_{49.3}$.

Note that microstructure changes fatigue life and ratcheting significantly. Precipitate free microstructure obtained by solutionization heat treatment gives the longest fatigue life close to furnace cooled heat treatment. Nano-size precipitated microstructure is yielding lowest fatigue life after 300 °C 100 hours. Two step ageing (500 °C 10 hrs +400 °C 24 hrs) yields to intermediate fatigue life. Lastly over aging, in the case of furnace cooling (550 °C 15 min + 550 °C to 100 °C in 100 hrs) yields high average fatigue life but also a high deviation. Note that actuation strain lowers with number of cycles for solutionized case significantly where it stays constant for all other heat treatments as can be seen in Figure 4.1.

Table 4.2 Summary of the experimental results for actuation fatigue tests on polished $Ni_{50.7}Ti_{49.3}$ samples. The stress level was 200 MPa for all shown tests.

Heat Treatment	**Actuation Strain (%)**	**Fatigue Life**	**Ratcheting in austenite (%)**	
			at failure	**at 100th cycle**
800 °C, 1hr		1013		
	6.00	812	5.76	4.43
300 °C, 100 hrs	5.02	305	2.46	1.71
	5.95	294	2.84	1.94
500°C, 10 hrs + 400°C, 24 hrs	3.48	450		
	3.65	631	3.99	2.86
550°C, 15min, FC 4.5 °C /hr		1313		
	3.18	501	2.71	1.75

Critical strain evolution with number of cycles can be seen in Figure 4.1.Note that ratcheting evolves the most in early stages of actuation fatigue thus ratcheting at 100 cycle was also reported in Table 4.2.

All fatigue life prediction laws considered in this study requires multiple material constants that are to be determined by experiments. Since only single stress level used in polished samples it is not possible to determine all the parameter through experimental data. In the following section, where unpolished samples were tests, multiple stress levels were studied. To compare different microstructures performance Smith-Watson-Topper approach was used. Trend lines were drawn to highlight performance difference in Figure 4.2. The coefficient in the power was selected to be -0.5 which is a typical value for most metals, and multiple multiplier coefficients were selected as shown in plots. Performance of the points within the same trend line considered to be equivalent where higher the multiplier coefficient better the fatigue life.

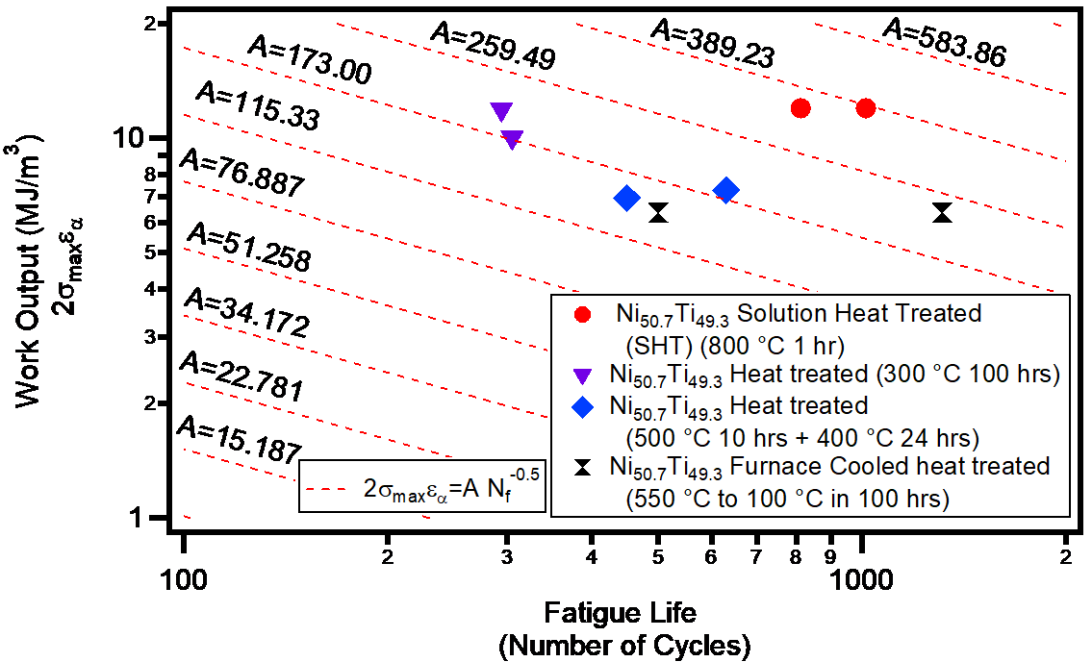

Figure 4.2 Work output versus fatigue life plots for all $Ni_{50.7}Ti_{49.3}$ microstructures. Smith-Watson-Topper trend lines with given coefficients are shown with dashed red lines.

Based on performance criteria described above, solutionized material shows the best fatigue life, where other heat treatments have comparable but lower fatigue life expectancy. If a Smith-Watson-Topper equation with material constant at power of fatigue life taken as -0.5, trend lines can be drawn for 4 heat treatments to determine multiplier parameter. Those values found to be 362.5, 189.8, 165.8 and 191.5 for solution heat treated, peak aged, two-step aged and furnace cooled microstructures respectively.

4.4.2 Actuation Fatigue of NiTi on Unpolished Samples

Table 4.3 Summary of the experimental results for actuation fatigue tests on unpolished $Ni_{50.7}Ti_{49.3}$ samples.

Heat Treatment	Stress (MPa)	Actuation Strain (%)	Fatigue Life	Ratcheting in austenite (%)	
				at failure	at 100th cycle
800 °C, 1hr	200	5.75	384	1.78	1.46
	250	5.98	369	6.14	5.22
	250	6.38	209	4.97	4.03
	300	7.00	125	12.07	11.15
300 °C 100 hrs	200	5.45	425	3.21	1.82
	250	5.47	321	4.86	3.61
	300	5.68	87	4.31	NA
500 °C, 10 hrs + 400 °C, 24 hrs	200	2.91	5890	2.82	1.40
	250	3.05	3564	5.41	3.23
	300	2.74	1807	4.14	2.59
Furnace Cooled 550 °C 15 Min 550 °C to 100 °C in 100 hrs	200	2.20	10187	2.96	1.42
	250	2.96	3833	2.88	2.33
	300	2.72	3161	4.79	2.78

Based on experience, it is found that testing samples with EDM recast layer on significantly increases fatigue life. Thus in this section, samples with as treated surface condition tested for actuation fatigue. In addition to changing surface condition, improvements in testing system was also taken into advantage. Real time temperature measurements and upper and lower cycle temperature target control made possible by

using third version of the setup. Details regarding to changes in experimental system can be found in 3.2.4.

Same 4 heat treatments used in previous section were further studied by testing unpolished samples. Samples were tested at three stress levels which were 200, 250 and 300 MPa summary of the results can be seen in Table 4.3.

Note that fatigue life of unpolished samples were significantly higher than polished ones in two step aging and furnace cooled conditions when the opposite is true for solutionized case. When compared using Smith-Watson-Topper fatigue law, parameters are A=158.798, 51.861, 70.22, 581.22 and B= -0.423, -0.246, -0.282, -0.529 determined with R^2=0.823, 0.871, 0.844, 1.00 for solutionized, peak aged, two-step aged and furnace cooled cases respectively. It must be noted that the data points for 300 MPa deviates from trend line in peak aged and two-step aged conditions. Because of that deviations slopes appear to be much shallower that typical value of -0.5. If those data points are excluded the SWT parameters become A=1461.40, 633.63, and B=-0.821, -0.540 for peak aged and two-step aged conditions respectively. This deviation is likely due to relatively high testing stress or limited ductility of the material. Note that peak aged condition still has significantly stiffer slope than typical value, probably due to limited number of data points.

Based on obtained values, two-step aged and furnace cooled conditions have virtually same fatigue performance and it is significantly better than other microstructures as shown in Figure 4.3. It must also be notes that since in two-step aged condition deviates from trend line at higher stresses, it can be noted furnace cooled case has larger operation range. Similarly solutionized and peak aged conditions have comparable fatigue

performance but peak aged condition has significantly stiffer slope. Thus if the trend holds true for the lower stress levels solutionized case is expected to perform better than peak aged condition.

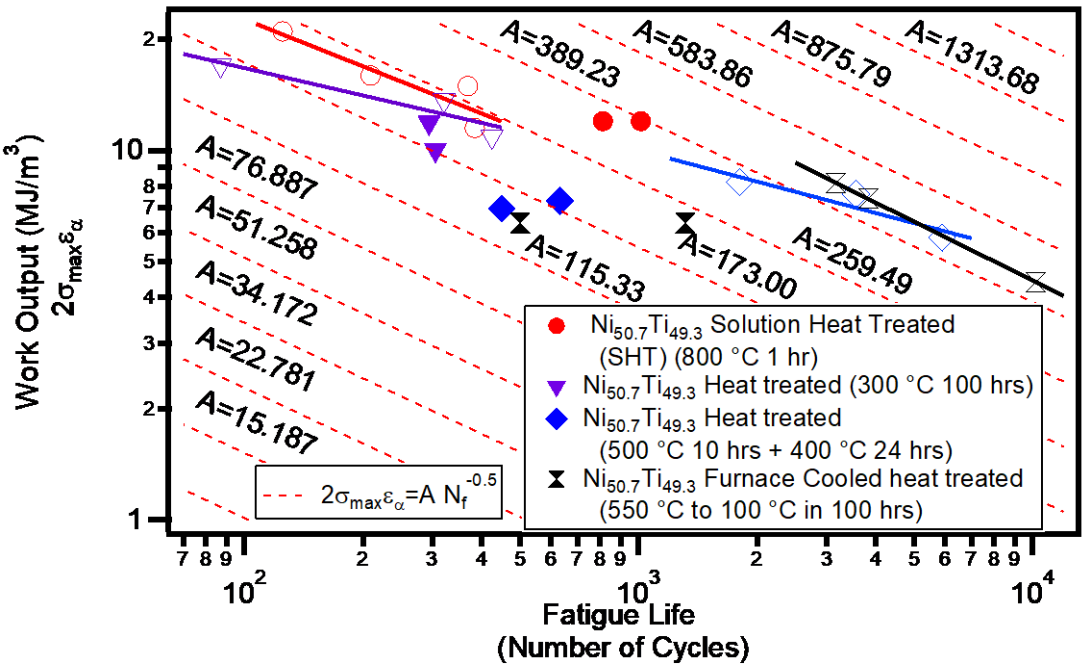

Figure 4.3 Work output versus fatigue life plots for all $Ni_{50.7}Ti_{49.3}$ microstructures for both polished and unpolished samples. Each microstructure is shown with a different shape and polished samples are shown with solid markers where open markers are for unpolished samples. Smith-Watson-Topper trend lines with given coefficients are shown with dashed red lines

4.4.3 Correlation between Mechanical Properties and Actuation Fatigue

A correlation between mechanical properties and mechanical fatigue has been established for mechanical fatigue of shape memory alloys. It is shown that if the ratio of

stress induced martensitic transformation stress (σ_{sim}) and yield stress (σ_{ys}) is minimized fatigue life is maximized [99] (see equation 4.1). In other words, higher yield or ultimate tensile stress and lower stress induced martensitic transformation stress maximizes fatigue performance. A similar correlation on actuation fatigue is desired to be established.

$$\frac{\sigma_{sim}}{\sigma_{ys}} = min \qquad \text{eq. 4.1}$$

In order to find the correlation between mechanical properties and fatigue, two sets of mechanical testing were done. Those mechanical tests are monotonic tension tests and Charpy impact tests. Summary of critical mechanical properties can be seen in Table 4.4 and stress-strain curves where the data points were obtained from can be seen in Figure 4.4.

When polished samples are considered, because data is limited, the trend is not be concluded and formulated with certainty. Solutionized case has baseline mechanical properties. The highest ductility was observed in this condition with low strength values. The highest fatigue performance from both life and SWT criteria was observed for this microstructure. Peak aging increases strength but it greatly reduces ductility. The fatigue life is the lowest for tested stress yet, in SWT criteria it is comparable to furnace cooled condition. Two-step aging doesn't increase strength significantly yet reduces ductility. It has the intermediate fatigue life and lowest SWT criteria fatigue performance. Furnace cooled condition, has an increase in strength and ductility is not reduced as much as other heat treatments. Fatigue life of this heat treatment is comparable to solutionized but it must be noted that actuation strain of this case is significantly lower. As a results it has comparable SWT criteria fatigue performance to peak aging heat treatment.

Table 4.4 Summary of critical mechanical properties of $Ni_{50.7}Ti_{49.3}$. The data is obtained by monotonic tension tests at one fully martensitic and one fully austenitic state.

Heat Treatment	Temperature (°C)	σ_{SIM} or σ_{MR} (MPa)	σ_{UTS} (MPa)	ε_{UTS} (%)
Solutionized 800 °C 1 hr + WQ	-50	147	817	28.70
	50	395	742	31.12
Peak Aging 300 °C 100 hrs +WQ	-50	110	964	11.14
	100	620	923	11.30
Two Step Aging 500 °C 10 hrs + 400 °C 24 hrs	-25	141	735	9.55
	100	320	865	17.29
Furnace Cooled 550 °C 15 Min 550 °C to 100 °C in 100 hrs	-50	161	922	16.39
	100	440	873	30.35

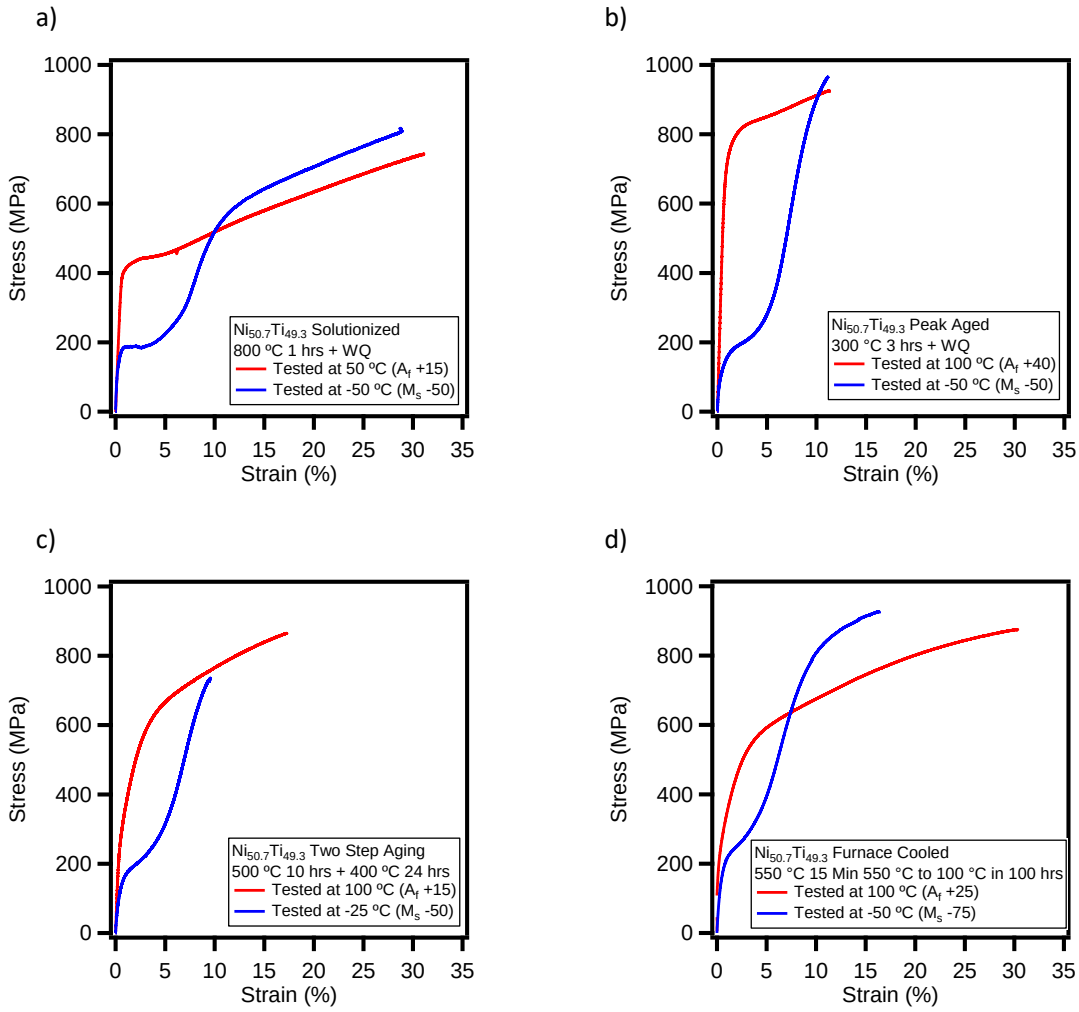

Figure 4.4 Stress strain curves of all 4 heat treatments on NiTi. a) Solutionized (800 °C 1 hrs + WQ) b) Peak aged (300 °C 3 hrs + WQ) c) Two Step Aging (500 °C 10 hrs + 400 °C 24 hrs) d) Furnace cooled (550 °C 15 Min + 550 °C to 100 °C in 100 hrs)

When unpolished samples are considered, although fatigue lifes changes with heat treatments all heat treatments fall into a very close SWT trend line. Although peak aged condition has very different mechanical properties, both their fatigue lifes and actuation

strains are very close. On the other hand, two-step aged condition has smaller actuation strain but significantly higher fatigue life. As a result all heat treatments fall into the same trend line.

Another characterization tool used to link mechanical properties to fatigue performance was Chapry impact testing. Charpy impact tests were conducted on 3 of the heat treatments. Details of testing can be found in section 3.2.2. Normalized impact toughness energy as a function of test temperature was shown in Figure 4.5.a. Note that there is a dip in super-elastic region for all heat treatments. Solutionized case has the highest impact toughness energy (425 kJ/m^2) at low temperatures (-50 °C) but it drops significantly to 122 kJ/m^2 levels when heated up to superelastic temperature for that microstructure. Furnace cooled case has comparable but slightly lower values except some temperatures. Peak aged condition consistently shows lower impact toughness energies than other heat treatments at all temperatures. If the average impact toughness values are considered, impact toughness energies correlate with fatigue lifes obtained under 200 MPa for polished samples but do not correlate well with SWT coefficients.

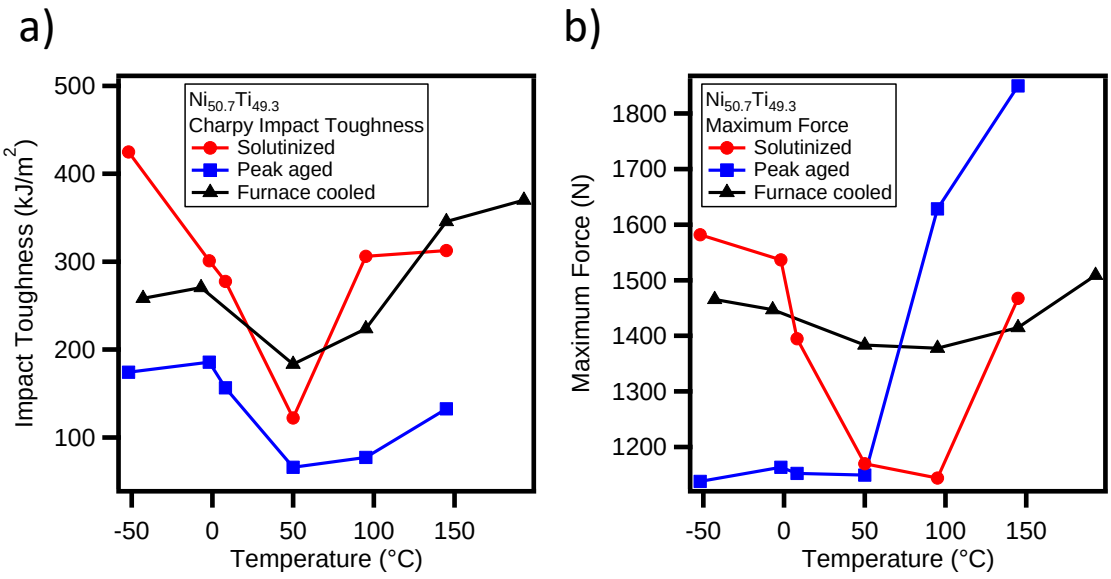

Figure 4.5 a) Charpy impact toughness test results as a function of temperature for three microstructures obtained by solutinized (800 C 1 hr + WQ), peak aged (300 C 100 hrs + WQ) and furnace cooled (550 °C 15 Min + 550 °C to 100 °C in 100 hrs) b) Maximum force obtained during charpy impact toughness tests as a function of temperature for three microstructures.

Maximum force obtained during charpy impact toughness tests were also shown in Figure 4.5.b. Note that temperature dependence on maximum force is significantly different for all three microstructures. In solutionized case, maximum force is high at low temperatures and it is lowered for a range (0 to 100 °C). Beyond that range maximum force increases again. In furnace cooled condition temperature has minimal effect on maximum force. Peak aged condition shows a sharp transition at 50 °C. At temperatures lower than 50 °C, maximum force is the lowest of all microstructures and after that critical temperatures it reaches to the highest values. Note that those values correlate with

monotonic tension test results where solutionized case has the lowest strength, furnace cooled condition has the intermediate and peak aged condition has the highest when measured at austenitic temperatures. Martensitic temperature response is likely a function of martensite orientation stress and ductility rather than purely ultimate tensile strength.

4.5 Post Mortem Investigation

After material fails, fracture surface and side surfaces of the broken samples were investigated by optical and electron microscope to determine presence and size of cracks and possibly identify nucleation site and reason of main crack that yields to fracture. Moreover to determine change in transformation temperature DSC tests were conducted.

Optical microscope images of side surfaces after failure for 3 microstructures (solution heat treated, peak aged and furnace cooled) can be seen in Figure 4.5 d-f . Note that this images were taken from originally polished samples. It can be deduced that a number of cracks form after thermal cycling. To quantify the presence of those cracks their length were measured within 20 mm from fracture surface. It is observed that number of cracks and distribution are significantly differs from one condition to another. Solutionized case has 306 cracks and their distribution can be seen in Figure 4.6 a-c . 300 °C 100 hours aged case 260 cracks in total and their distribution can be seen in Figure 18 b. Furnace cooled case gives the most significant difference. Total number of cracks in it is 65 and it has 22 cracks that are longer than 300 microns. Also note that crack locations change with heat treatments. In solutionized and peak aged conditions cracks mostly form on the side where in furnace cooled case they form on the edge.

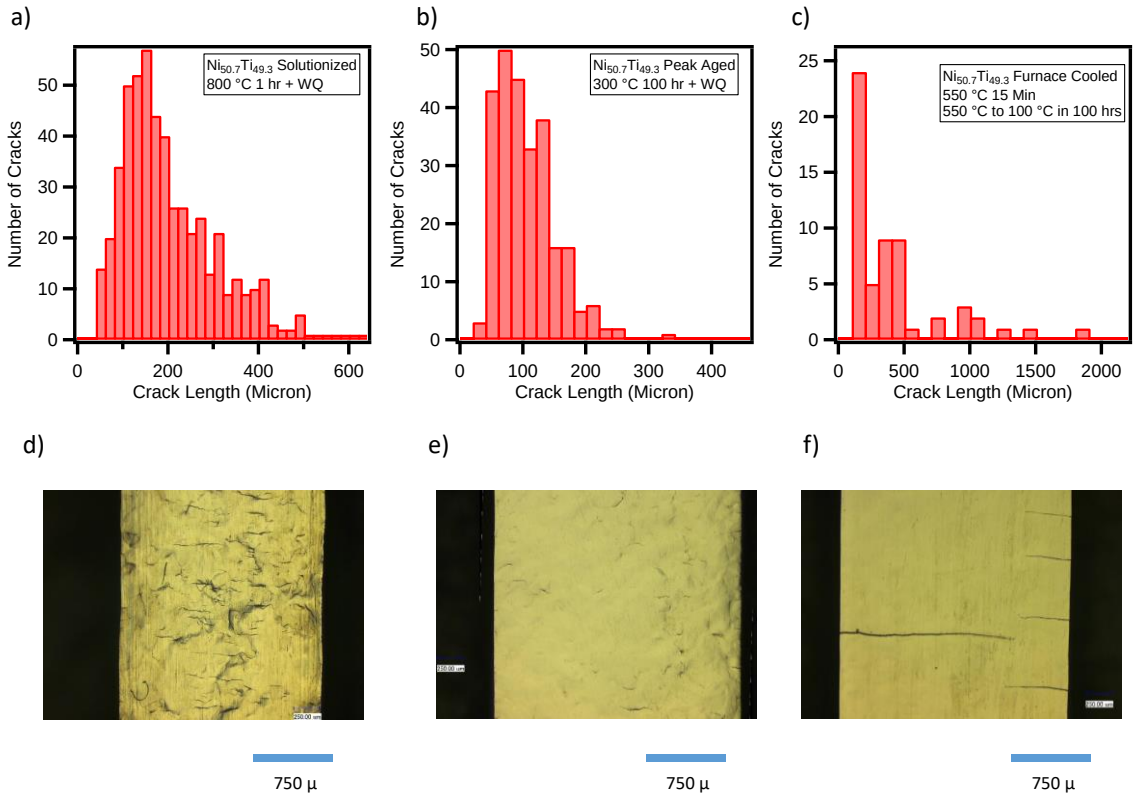

Figure 4.6 Statistical analysis of cracks on NiTi. a-c) shows histograms of crack lengths d-f) shows optical microcopy images

Transformation temperatures determined by DSC before and after fatigue can be seen in Table 4.5. Note that M_s temperatures were decreased in all cases, where M_f were lowered for solutionized and peak aged conditions but increased for furnace cooled condition. A_s also decreased for all cases, where A_f increased for solutionized and peak aged condition but decreased for furnace cooled. This behavior was explained by Miyazaki [59]. It was reported that under no stress or prestrain if material is thermally cycled transformation temperatures decrease. On the other hand if material is thermally

cycled under stress or prestrain transformation temperatures increases with number of cycles.

Table 4.5 Comparison of transformation temperatures that are determined by DSC on NiTi before and after fatigue testing

Material	Condition	M_s (°C)	M_f (°C)	A_s (°C)	A_f (°C)
Solutionized	Virgin	-22	-2	12	33
	Post mortem	-47	-14	-6	18
	Difference	-25	-12	-18	-15
300 °C 100 hours aged	Virgin	-30	-2	52	60
	Post mortem	-44	-10	42	69
	Difference	-14	-8	-10	9
Furnace Cooled	Virgin	17	42	52	75
	Post mortem	-12	60	31	71
	Difference	-29	18	-21	-4

4.6 Discussions

It is found that surface has a significant effect on actuation fatigue performance of SMAs. Unpolished samples with two-step aging have significantly higher number of cycles to failure (fatigue life) with comparable actuation strain. On the other hand, solution heat treated samples have lower number of cycles to failure. Moreover, peak aged condition (300 °C 100 hrs) has same fatigue life and actuation strain in both polished and unpolished samples. It is hypothesized that surface morphology created by martensitic transformation acts a crack nucleation cite. When martensite variant boundaries reach to surface, they create very sharp intrusions which can act as crack nucleation sites. This hypothesis illustrated by Hornbogen [100] as can be seen in Figure 4.6. In solutionized

case, since actuation strain is the highest, protecting effect of EDM recast layer is lowered. The ductility or strain that can be accommodated by this layer is limited. If material shows actuation strains beyond this limit, EDM layer will crack and those crack will propagate to the interior of material and yield to failure. That can explain the reduction in fatigue life in solution heat treated case. Likewise this can explain the reason of no reduction or improvement on fatigue life of peak aged condition since its ductility is already limited. In two-step aging case unpolished surface with EDM recast layer has higher fatigue life because martensite surface relief is prevented by the layer at the same time the strains generated by material is lower than ductility limit.

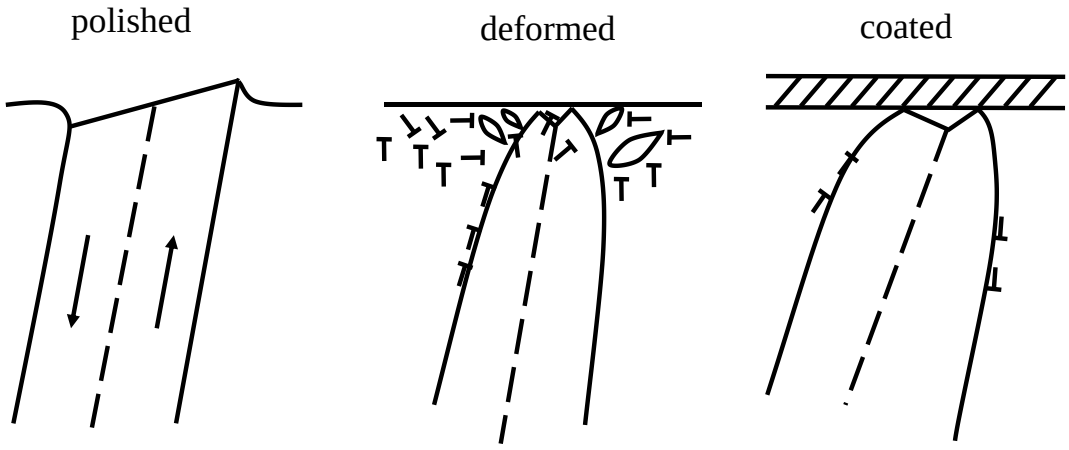

Figure 4.6 Morphology of surface during actuation fatigue for 3 surface conditions, polished, deformed and coated [100]

4.7 Summary and Conclusions

Effect of microstructure and surface condition on actuation fatigue of $Ni_{50.7}Ti_{49.3}$ was studied. Although there are several methods to compare fatigue performance, Smith-Watson-Topper approach was used to quantify it.

1. It is found that microstructure has an effect on fatigue performance. Because only single stress level was tested on polished conditions it is not possible to determine SWT coefficients for each microstructure but if a typical exponential value is used, which is -0.5 in this study, it can be noted that solutionized case has the best fatigue performance. Solutionized case has the highest work output and average fatigue life. Peak aged and furnace cooled conditions has comparable SWT coefficients where two-step aged conditions shows the worst fatigue performance.
2. When unpolished samples are considered, furnace cooled and two-step aged conditions showed virtually same fatigue performance but two-step aged condition started to show deviation at the highest stress level (300 MPa). Solutionized and peak aged conditions also showed comparable results.
3. Effect of surface condition has also been studied. It is found that, EDM recast layer significantly increases fatigue performance of two-step aged and furnace cooled condition. At the same time performance of peak aged conditions has not changed and solutionized case showed a decrease. This is associated with martensite boundary surface interaction. Moreover, due to the limitation of

strain that can be accommodated by surface layer, the increase in fatigue performance was expected and observed for the cases with lower actuation strains.

4. Correlations between mechanical properties and actuation fatigue performance were investigated. When monotonic tensile tests were considered, it can be noted that ductility has the most important effect on fatigue performance. Peak aged condition has the highest σ_{uts} but the fatigue life is the smallest. This is also expected in part due to high actuation strain. On the other hand, furnace cooled condition has the intermediate σ_{uts} but high ductility. In polished samples, when SWT coefficients were considered solutionized has the highest thus the best performance, followed by virtually same value for peak aged and furnace cooled. Two step aged condition had the lowest coefficient. In unpolished samples, the most important factor is found to be actuation strain. Below a critical value EDM recast layer act as a rigid coating and increases fatigue life considerably but for any value higher than that it actually reduces the fatigue performance. Moreover charpy impact tests were conducted and although impact energies and fatigue lives were qualitatively matched for polished samples. When surface effects were introduced there was no correlation.

5. EFFECT OF MICROSTRUCTURE ON TENSILE ACTUATION FATIGUE OF $Ni_{50.3}Ti_{29.7}Hf_{20}$

5.1 Overview

In this section investigation on effect of microstructure on tensile actuation fatigue of $Ni_{50.3}Ti_{29.7}Hf_{20}$ is presented. The microstructure is modified by precipitation, 3 microstructures are considered. In addition to investigating effect of microstructure, several fatigue life prediction laws were utilized and compared in terms of sensitivity and predictive power. Effect of surface finish was also considered which yielded to a major observation. Lastly correlations between fatigue performance and easily measurable quasistatic and high strain rate mechanical properties are investigated.

5.2 Introduction

Increasing transformation temperatures is desired to prevent auto actuation. In this study ternary alloying addition is chosen as the method of increasing transformation temperature. A slightly Ni rich composition is selected to make it possible to modify microstructure with precipitation. Hf is selected as ternary alloying element.

A similar systematical study to previous chapter was conducted. Actuation fatigue tests were conducted on flat dog-bone samples. Different fatigue life prediction laws applied to obtained data. Mechanical properties were measured and the correlation between those properties and fatigue was evaluated.

5.3 Experimental Procedure

Material used in this section was described in section 3.1.2. Heat treatments were selected based on previous experience and can be found in the Table 5.1 with transformation temperatures. First version of the fatigue testing system was used in unpolished samples. The stress levels were 50, 100, 150 and 200 MPa. Because second version of the fatigue testing system described in section was used for unpolished samples, it was possible to use temperature target control. Lower cycle temperature was always set to 40 °C. On the other hand two levels of upper cycle temperatures (300 and 350 °C) were considered. This made it possible to assess effect of upper cycle temperature on fatigue life. Two stress levels were also considered which are 300 and 400 MPa. Lower upper cycle temperature value (300 °C) is not tested for 400 MPa to prevent partial transformation. It is known that due to Clausius-Clapeyron law, higher stresses yield to higher transformation temperatures. The current test matrix makes it possible to assess isolated effect of upper cycle temperature within 300 MPa tests and effect of stress within 350 °C upper cycle temperature tests. In that regard, the test matrix can be classified as parametric rather than full factorial.

Table 5.1 List of heat treatments, description of microstructure and transformation temperatures obtained by DSC for nickel rich NiTiHf ($Ni_{50.3}Ti_{29.7}Hf_{20}$)

Heat Treatment Type	**Heat Treatment Parameters**	**Resulting Microstructure**	**Transformation Temperatures (C)**			
			M_f	**M_s**	**A_s**	**A_f**
Peak Aging	550 °C 3 hrs +AC	Nano size coherent H phase precipitates	121.6	153.7	151.0	176.3
Over Aging	600 °C 10 hrs +AQ	Submicron size coherent H phase precipitates	141.5	181.1	185.1	220.3
Furnace Cooling	700 °C to 100 °C in 48 hrs	Micron size incoherent H phase precipitates	161.8	213.9	213.2	269.0

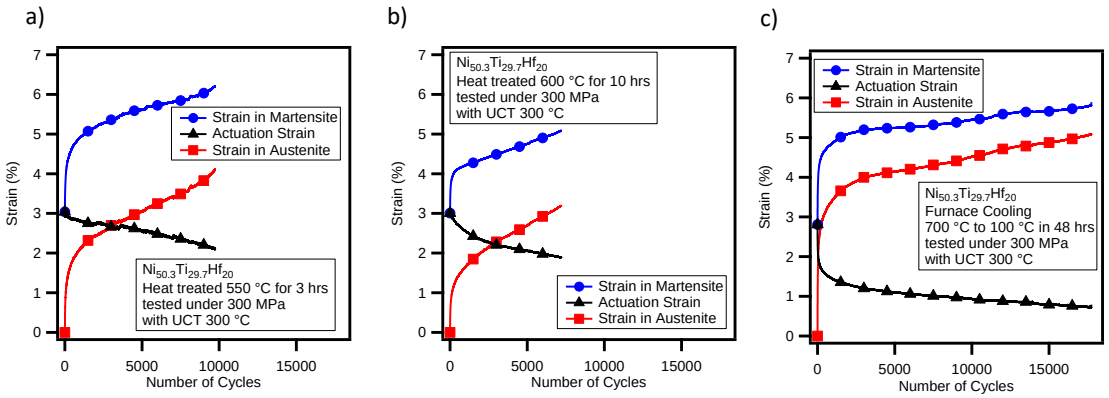

Figure 5.1 Evolution of strains with number of cycles for all microstructures of $Ni_{50.3}Ti_{29.7}Hf_{20}$.

5.4 Results

The actuation fatigue results are divided into two categories. In the first section fatigue life of polished samples will be presented. Note that stress levels are lower in that study because after 200 MPa, fatigue life decreased to single cycle.

5.4.1 Actuation Fatigue of NiTiHf on Polished Samples

Only one heat treatment which is peak aging (550 °C, 3 hrs) used in this study. Stress levels are 50, 100, 150 and 200 MPa. The first version of the fatigue system used in this part of the work thus upper cycle temperature is unknown.

Table 5.2 Summary of the experimental results for actuation fatigue tests on polished $Ni_{50.3}Ti_{29.7}Hf_{20}$ samples.

Heat Treatment	Stress (MPa)	Actuation Strain (%)	Fatigue Life	Ratcheting in austenite at failure (%)
550 °C, 3 hrs	200	NA	1	NA
	150	1.19	13	0.39
	100	1.26 ± 0.07	34 ± 2	0.42 ± 0.04
	50	0.45 ± 0.06	440 ± 190	0.84 ± 0.03

Results that are reported in Table 5.2 are based on 2 test run at the same stress level for 50 and 100 MPa. Note that there is a significant variation in 50 MPa tests, which is 190 cycles. This could be due to lack of temperature control. There is only one test in 150 MPa, where multiple samples tested under 200 MPa failed during first cycle. Thus it is not possible to extract actuation strain and ratcheting for those tests.

5.4.2 Actuation Fatigue of NiTiHf on Unpolished Samples

Summary of all results on unpolished NiTiHf can be seen in Table 5.3. In parametric comparison, when stress level is 300 MPa, 300 °C upper cycle tests generated higher fatigue lifes and lower average actuation strain. Effect of stress can be deducted by comparing 350 °C upper cycle temperature tests. As expected increasing stress decreases fatigue life. Note that for furnace cooling (700 °C to 100 °C in 48 hrs) and for overaged (600 °C, 10 hrs) heat treatments, fatigue life at 400 MPa is drastically shorter. Evolution

of strains for all three microstructures can be seen in Figure 5.1. Although fatigue life of furnace cooled samples are higher than that of peak aged condition, actuation strain of former is significantly smaller.

Table 5.3 Summary of the experimental results for actuation fatigue tests on unpolished $Ni_{50.3}Ti_{29.7}Hf_{20}$ samples.

Heat Treatment	Stress (MPa)	Upper Cycle Temperature (°C)	Actuation Strain (%)	Fatigue Life	Ratcheting in austenite at failure (%)
550 °C, 3 hrs	300	300	2.54 ± 0.25	10454 ± 694	3.13 ± 0.92
	300	350	3.21 ± 0.43	4028 ± 329	3.82 ± 0.77
	400	350	3.54 ± 0.56	2716 ± 2301	5.92 ± 1.45
600 °C, 10 hrs	300	300	1.94 ± 0.22	8859 ± 1216	3.86 ± 1.02
	300	350	2.40 ± 0.36	5774 ± 1339	4.13 ± 0.13
	400	350	3.22 ± 0.36	62 ± 21	2.4 ± 0.16
700 °C to 100 °C in 48 hrs Furnace Cooling	300	300	1.14 ± 0.13	13110 ± 4632	4.60 ± 0.50
	300	350	1.43 ± 0.10	8659 ± 2112	5.69 ± 0.58
	400	350	2.77 ± 0.02	7 ± 2	0.84 ± 0.09

To compare fatigue performance of different microstructures a performance metric needs to be established. The major fatigue life predicting laws, which are mentioned earlier will be used to assess effect of microstructure.

First and historically earliest fatigue life predicting law is Wohler Curves and the linear trend lines. Results for all three microstructure can be seen in Figure 5.2. Although original Wohler method is designed to be used with stress amplitude, strain amplitude was also used in literature. Two Wohler curves are constructed for applied stress and actuation strain (2 times of strain amplitude) as can be seen in Figure 5.2.a and Figure 5.2.b. Note that Wohler Curves method doesn't distinguish between upper cycle temperatures. When stress based Wohler curves were considered as in Figure 5.2.a, trend lines are drawn for same upper cycle temperature (350 °C) and for two stress levels (300 and 400 MPa). Lower upper cycle temperatures tests shows higher fatigue lifes. Thus predictive power of this method is limited to a subset of conditions. The tests run must have the same parameters, or for each parameter set a new study with a new test matrix needs to be conducted. Moreover, because fatigue lifes of furnace cooled and over aged samples are exceptionally low under 400 MPa, predictability of trend lines drawn by this method is questionable. The performance metric in this approach is higher fatigue life at the same stress level. Based on that, peak aged condition has the better fatigue life performance above 300 MPa, but over aged condition is better under lower stresses and the furnace cooled condition is the best. But as mentioned earlier those conclusions are not very sound due to extremely low fatigue lifes at 400 MPa. When strain based Wohler curves considered as in the case of Figure 5.2.b, peak aged condition is showing best fatigue life

below actuation strains of 3.5% above which extrapolation of overaged case shows longer fatigue lifes. But it must be noted that while drawing trendline 400 MPa results from overaged condition was omitted thus extrapolation do not hold at those stress/strain levels based on experiments. It can be concluded that peak aged condition shows best fatigue performance fallowed by over aged case and the furnace cooled case shows the worst performance.

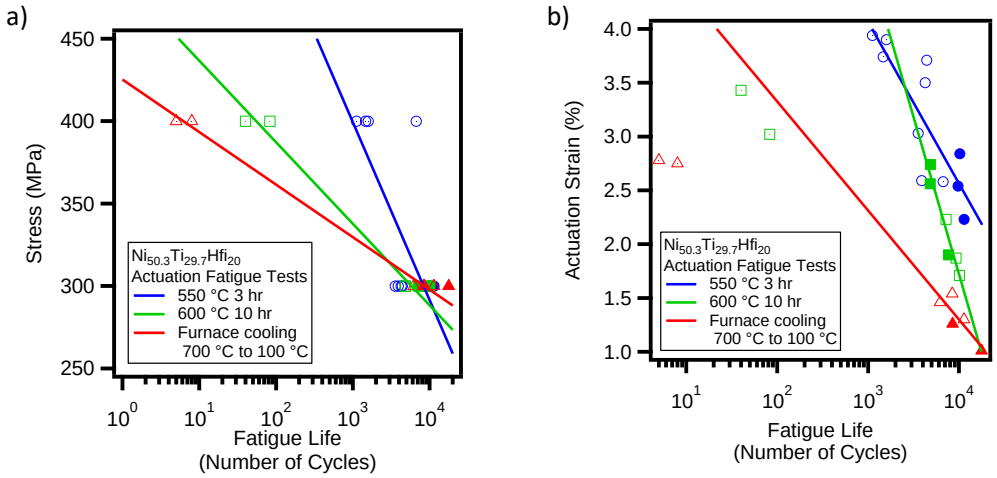

Figure 5.2 Wohler curves for unpolished $Ni_{50.3}Ti_{29.7}Hf_{20}$ actuation fatigue results. a) Plot showing applied constant stress (in linear axis) versus fatigue life (in logarithmic axis). b) Plot showing actuation strain which is twice of strain amplitude (in linear axis) versus fatigue life (in logarithmic axis)

Second fatigue life predicting law that is considered in this work is Manson-Coffin. Results for all three microstructures can be seen in Figure 5.3. This method can indirectly take into account for upper cycle temperature and stress level. Thus predictive power of this method is higher than Wohler method. All test results for each microstructure is used

to fit fatigue life predicting function in Figure 5.3. The performance metric in this method is plastic deformation per cycle. For same plastic deformation per cycle peak aged condition shows the highest fatigue life at values higher than 0.001 % per cycle strain. Below this level furnace cooled heat treatment is projected to have higher fatigue lifes. The over aged condition is always showing intermediate performance.

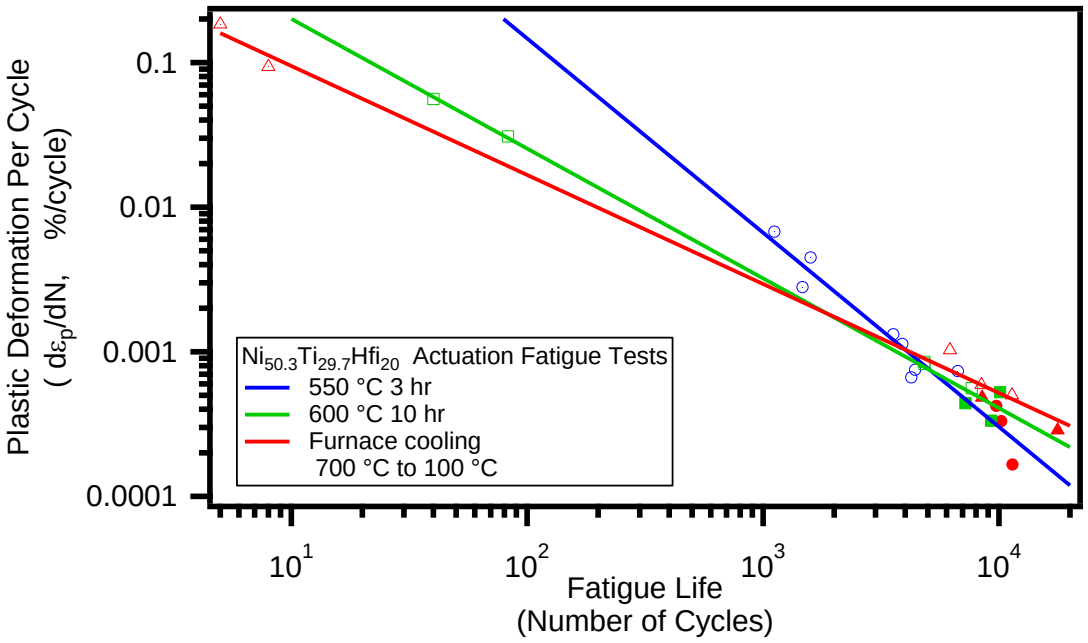

Figure 5.3 Manson-Coffin curves for unpolished $Ni_{50.3}Ti_{29.7}Hf_{20}$ actuation fatigue results. Plot showing plastic deformation per cycle versus fatigue life (both in logarithmic axes).

Third fatigue life prediction law is Smith-Watson-Topper. Results for all microstructures can be seen in Figure 5.4. This method directly take stress and actuation strain into account, and indirectly takes upper cycle temperature into account since it effects actuation strain. It has the best resolving power to differentiate performance of

different microstructures. Performance metric in this method is work output which is the product of actuation strain and applied stress. Peak aging condition is performing better in all work output values, where over aged condition is intermediate and furnace cooling shows the poorest performance. Note that because 400 MPa tests for furnace cooled and over aged cases showed extremely low fatigue lifes and reduce quality of the fitting, they are removed from the data used for fitting. It suggests that fatigue performance changes significantly beyond a threshold between 300 and 400 MPa. It will be better explained with the presentation of mechanical properties.

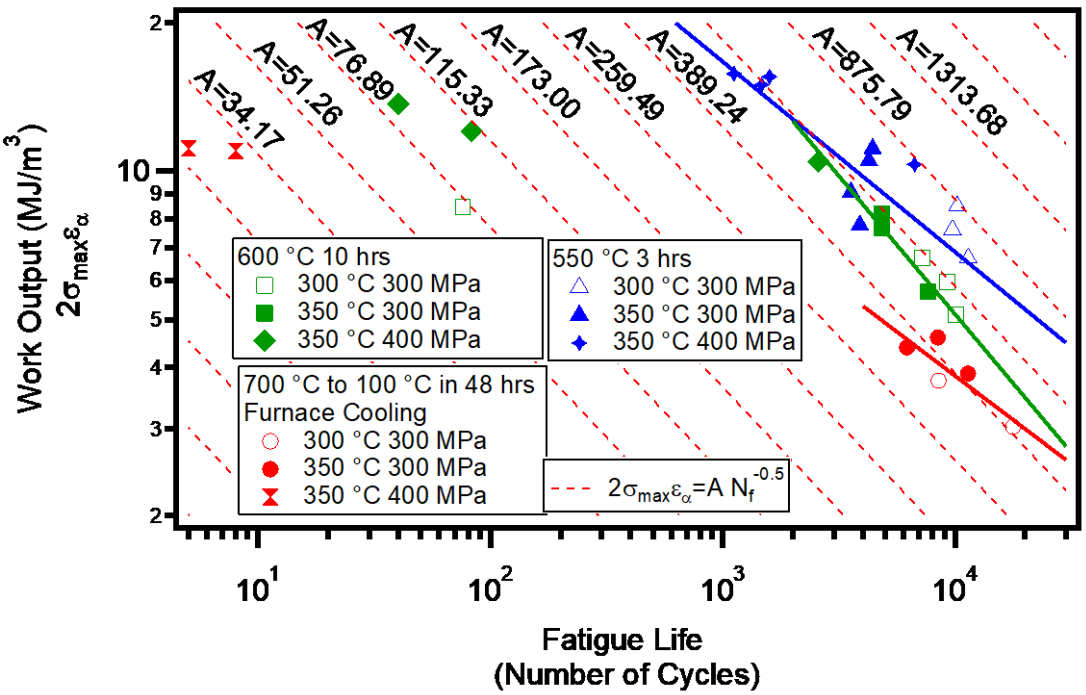

Figure 5.4 Smith-Watson-Topper curves for unpolished $Ni_{50.3}Ti_{29.7}Hf_{20}$ actuation fatigue results. Plot showing plastic deformation per cycle versus fatigue life (both in logarithmic axes).

5.4.3 Correlation between Mechanical Properties and Actuation Fatigue

Uniaxial monotonic tension tests run for room temperature on all heat treatments. The results can be seen in Figure 5.5. Note that although room temperature is significantly below M_f for all heat treatments, materials don't show plateau. After initial linearity material continuously hardens till failure. The distinction between, σ_{mr} and σ_{ys} for martensite is not clear. It is possible that, the material doesn't yield and fail in a brittle manner. Critical mechanical properties are tabulated in Table 5.4.

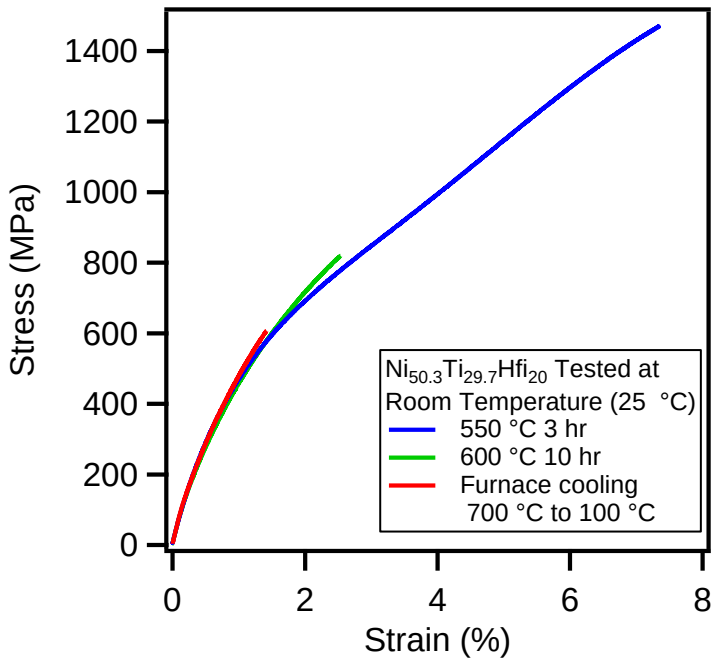

Figure 5.5 Monotonic tension results showing stress-strain plots for all 3 microstructures. Tested at room temperature for $Ni_{50.3}Ti_{29.7}Hf_{20}$

Table 5.4 Summary of critical mechanical properties of $Ni_{50.3}Ti_{29.7}Hf_{20}$. The data is obtained by monotonic tension tests at room temperature which is significantly lower than Mf for all heat treatments.

Heat Treatment	σ_{mr} (MPa)	σ_{uts} (MPa)	ε_{uts} (%)
550 °C, 3 hrs	496.54	1469.16	7.34
600 °C, 10 hrs	472.11	818.90	2.53
700 °C to 100 °C in 48 hrs Furnace Cooling	531.31	607.60	1.42

Note that Hornbogen's approach [99] holds for actuation fatigue of NiTiHf. Since yield stress is not clear ultimate tensile strength was used in denominator.

5.5 Discussions

Similar to binary NiTi, the most significant effect is the surface condition. Samples with EDM recast layer, have higher fatigue lifes. Upper cycle temperature also has an effect on fatigue life. Higher upper cycle temperatures yield to lower fatigue life. This can be associated by complete transformation for more number of cycles. It is known that transformation temperatures increase with number of cycles. If upper cycle temperature is lower, after certain number of cycles partial transformation will be observed. The indication of that is reduction in actuation strain. If the actuation strain is reduced, fatigue life increases. This hypothesis further supported by Smith-Watson-Topper fatigue life prediction law. Although upper cycle temperature changes fatigue life, data points stay in proximity of same trend line. Increased stress reduces fatigue life, as also in the case of other structural materials.

Correlation between mechanical properties and fatigue performance was also studied by monotonic tension testing. Peak aged condition showed highest σ_{uts} and ductility at the same time. As a result it was expected to show best fatigue performance and it is in agreement with the actuation fatigue testing data. Similarly over aged and furnace cooled cases has intermediate and lowest σ_{uts} and ductility values respectively and it is in agreement with their fatigue performance. Note that due to significant hardening behavior after onset of martensite reorientation it is not possible to identify elastic deformation and yield of martensite. In general this material can be considered brittle.

Effect of surface on actuation fatigue is also studied and it is found that testing material with EDM recast layer on the surface, increases fatigue performance considerably. This can be rationalized by the general lack of ductility and lower actuation strains. Similar improvement was found in binary NiTi when actuation strains were smaller than 5 %,

5.6 Summary and Conclusion

Effect of microstructure and surface was studied on precipitation hardened nickel rich NiTiHf ($Ni_{50.3}Ti_{29.7}Hf_{20}$) high temperature shape memory alloys. Microstructure was changed by aging heat treatments and 3 heat treatments namely peak aging (550 °C 3 hrs), over aging (600 °C 10 hrs) and furnace cooling (700 °C to 100 °C in 48 hrs). Overall it is found that NiTiHf has better fatigue performance than binary NiTi compositions.

Main findings in this study can be summarized as follows:

1. The surface effect was studied and it is found that polished samples show significantly lower fatigue lifes than samples with EDM recast layer on. The reason was associated with surface-martensite boundary interaction. When martensite variant boundaries reach to the surface they create sharp intrusions. Those intrusions can act as nucleation sites and reduce fatigue life and performance. In the presence of a coating martensite boundaries can't reach to te surface and form sharp boundaries thus enhance fatigue performance.
2. The effect of microstructure was studied and it is found that peak aging condition shows the best fatigue performance with respect to Smith-Watson-Topper approach. Peak aged condition has the highest work output and fatigue life at the same time. The over aged condition is showing intermediate fatigue performance while furnace cooled condition has to worst performance.
3. Three fatigue life prediction methods namely Wohler, Manson-Coffin and Smith-Watson-Topper were studied. It is found that Wohler curves don't have much of prediction power when used with testing stress. The order of fatigue performance is peak aged, over aged and furnace cooled for fatigue lifes less than 10000 cycles. At that point there is an infliction point beyond which order is reversed. When used with actuation strain the resolution is better since it indirectly takes other effects such temperature range into account. In Manson-Coffin approach again there is an infliction point at around 5000 cycles and trends are same with Wohler method. Manson-Coffin approach is more useful when rating material in terms of fatigue life per unit accumulated plastic deformation when plastic deformation is the

critical variable in the design this approach can be used. In Smith-Watson-Topper approach the order of fatigue performance is again peak aged, overaged and furnace cooled microstructures. This approach is taking stress, actuation strain and indirectly other effects such as partial transformations and temperature range. Also this approach takes work output as a metric thus best suits for actuator applications.

4. Correlation between mechanical properties and fatigue performance was also studied. It is found that peak aged condition has highest ductility and strength. As a result, it has the best fatigue performance. Over aged condition has the intermediate ductility and strength when furnace cooled has the worst. Those heat treatment also show respective fatigue performances to their mechanical properties.

6. EXTENDED THERMO-MECHANICAL CYCLING UNDER SHEAR OF NiTiHf

6.1 Overview

In this section investigation on evolution and stability of TWSME on $Ni_{50.7}Ti_{49.3}Hf_{20}$ is presented. TWSME is obtained by thermo-mechanical cycling on hallow cylinder which are called torque tubes. Samples are cycled up to 1600 thermal cycles. Effects of stress level, sample geometry and number of cycles are studied. After evolution of TWSME is measured one sample is systematically annealed to determine stability of established TWSME. Microstructure of the material before and after training is studied by TEM.

6.2 Introduction

Solid state actuators which uses SMAs as active material can benefit either one way shape memory effect (OWSME) combined with a mechanism to re-set the actuator or two way shape memory effect where the material has two stable configuration which can be accesses many times by putting the material to thermal domain where the desired state is stable at. Unlike OWSME, TWSME requires specific conditioning of the material called training. In this study training is achieved by thermo-mechanical cycling. Torque tubes are selected for this work not only because it is a relevant geometry from application point of view but also to study effect of stress state.

6.3 Experimental Procedure

Material used in this study was $Ni_{50.3}Ti_{29.7}Hf_{20}$ in peak aged condition which can be obtained by 550 °C 3 hrs aging. The details about the material and test system can be found in sections 3.1.2 and 3.2.5 respectively.

The thermo-mechanical training route was chosen to obtain TWSME in the present study which can be defined as thermal cycling between two specified temperatures under constant stress levels, until certain desired properties are reached, such as stable or zero irrecoverable strain per cycle or stable actuation strain, or until a specified number of cycles. It is known that martensitic transformation temperatures change as a function of applied stress in accordance with the Clausius-Clapeyron relation and they evolve with the number of cycles during extended thermal cycling. To ensure complete transformation, the upper cycle temperature should be above A_f at all times. For this study, 50°C above A_f temperature under 200 MPa shear stress, which is 240°C in the present case, has been chosen as the upper cycle temperature. Similarly, lower cycle temperature was chosen to be 80°C which is 50°C below M_f under 20 MPa which is the lowest shear stress level tested.

Table 6.1 The list of the $Ni_{50.3}Ti_{29.7}Hf_{20}$ torque tubes used in this study. Thick or thin walled tubes were tested under constant torsional loading and thermally cycled (i.e. trained) across the martensitic transformation temperatures. The training shear stress levels and number of cycles applied are summarized in the table. Thick tubes had the wall thickness of 1.86 mm while thin walled tubes had a thickness of 1.33 mm.

Name	Wall Thickness	Training Shear Stress (MPa)	Characterization Shear Stress Levels (MPa)	Number of Thermo-Mechanical Cycles
Tube-1	Thick (1.86 mm)	145	20, 35, 55, 90, and 145	1600
Tube-2	Thick (1.86 mm)	145	20, 35, 55, 90, and 145	1600
Tube-3	Thick (1.86 mm)	200	20, 55, 110, and 200	600
Tube-4	Thick (1.86 mm)	200	20, 55, 110, and 200	600
Tube-5	Thin (1.33 mm)	145	20, 45, 90, 110, and 145	1600
Tube-6	Thin (1.33 mm)	145	20, 45, 90, 110, and 145	1600

The effects of testing parameters and geometric factors, i.e. applied shear stress level, the number of training cycles, and tube wall thickness, have been investigated. For each of these parameter, two levels were chosen: the training shear stress levels were 145 MPa or 200 MPa, the number of training cycles were 600 or 1600 cycles, and the wall thicknesses were 1.33 mm or 1.87 mm. A full factorial test matrix would require 8 experiments without repetition, instead a parametric test matrix has been designed. With this test matrix, the isolated effects of each parameter can be obtained keeping other parameters constant.

A training path here is defined as a pair of stress and the number of cycles. Several different training paths were used in this study. These paths can be classified based on the number of training cycles as “long” for 1600 cycles and “short” for 600 cycles, or based on the shear stress level under which the training is performed such as “high stress” for 200 MPa and “low stress” for 145 MPa. 600 cycles is chosen for short training path based on previous experience which shows less than 600 cycles is enough to fully train the material. Low stress, 145 MPa is chosen to be just above martensite reorientation stress of this material. Actuation behavior of the samples (actuation strain as a function of the applied stress) was determined by a procedure what we call “characterization sequence”. Characterization sequence is subjecting the samples to 3 thermal cycles under a set of stress levels. Five and four stress levels were selected for 145 MPa and 200 MPa training stresses respectively. These levels are summarized in Table 6.1.

Testing under 0 MPa was not performed due to the limitations of the experimental setup. Therefore, to report the actual TWSMS, which is the actuation response under no stress, first two actuation strain vs. stress data points were used to extrapolate and estimate the no stress behavior of the samples. These estimated points were marked with hallow markers and connected with dashed lines in the plots, reported in the next section, for clear distinction from the experimentally measured data points. For the long route (1600 cycles), the characterization sequence was employed after the 100^{th}, 350^{th}, 600^{th}, 1100^{th} and 1600^{th} cycles, while for the short route (600 cycles), the characterization sequence was applied after the 100^{th}, 350^{th} and 600^{th} cycles.

6.4 Results

6.4.1 Evolution of Actuation Strain and TWSME during Thermo-Mechanical Training

For the low stress (145 MPa), longer (1600 cycles) training path, both thick (Tube-1 and Tube-2) and thin (Tube-5 and Tube-6) torque tubes were tested. Two tubes were used for each condition to check the repeatability, and the reported results here are the averages from these two repetitions. As the results from the thick and thin tubes are almost equivalent, only those from the thick tubes are introduced in this section. Before any training, the thick tubes exhibit only 0.053 ± 0.004% strain (Figure 6.1.a), which is most likely because of the transformation volume change and this indicates there is no TWSME on the material before the training.

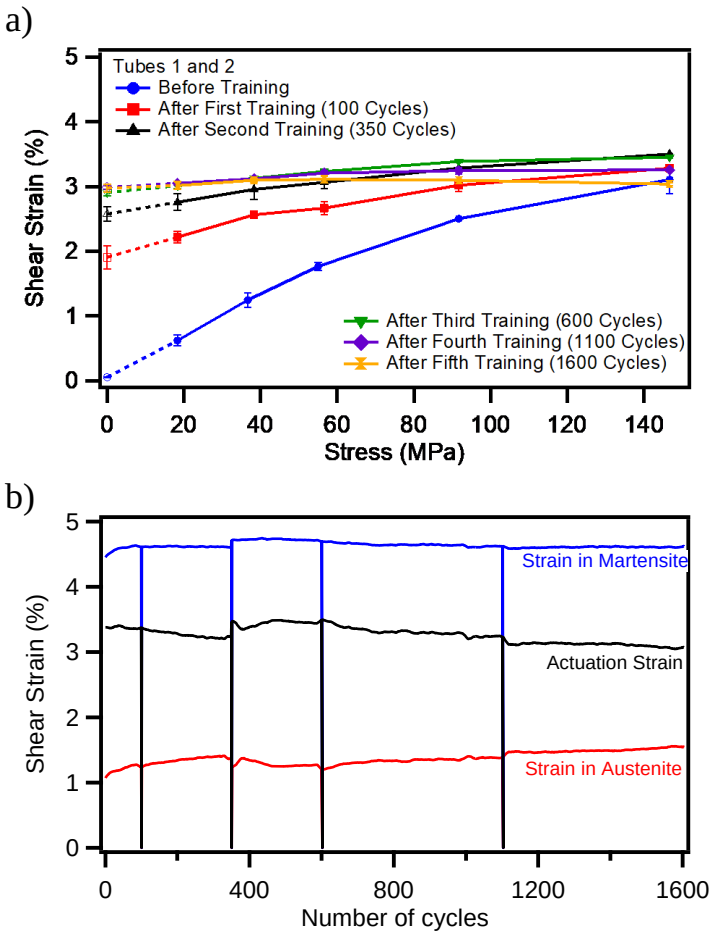

Figure 6.1 a) Shear strain vs. applied shear stress response of the $Ni_{50.3}Ti_{29.7}Hf_{20}$ torque tube samples (Tube-1 and Tube-2 in Table 6.1) during the "characterization sequence". b) Evolution of the strain in martensite, strain in austenite, and actuation strain in Tube-2 under 145 MPa for the long training path (1600 cycles). The strain drops at certain number of cycles indicates that the characterization sequence was applied to monitor the TWSMS evolution.

The actuation strain on the un-trained tubes is about 3.107 ± 0.216 % under 145 MPa. After 100 training cycles, TWSMS increases to 2.083 ± 0.176 % and the actuation strain under the training stress only slightly increases to 3.283 ± 0.025 %. Percentage of

TWSMS to the actuation strain under the training stress is about 60 % after 100 cycles. Upon further training, actuation shear strain vs. stress response (Figure 6.1.b) becomes less dependent on the stress level. After 350 training cycles, TWSMS and the actuation strain under 145 MPa are 2.576 ± 0.110 % and 3.453 ± 0.016 % respectively. After 600 training cycles, both TWSMS and the actuation strain under 145 MPa seem to saturate at about 2.906 ± 0.053% and 3.453 ± 0.016%, respectively, making the percentage of TWSMS to the actuation strain almost 84%. Further training cycles have negligible effect on TWSMS with a maximum value of 2.95 ± 0.07%. On the other hand, the actuation strain under 145 MPa decreases from 3.453 ± 0.016 % to 3.038 ± 0.024 % progressively by increasing the number of training cycles from 600 to 1600 cycles. Evolution of TWSMS as a function of the number of cycles can be seen in Figure 6.2.

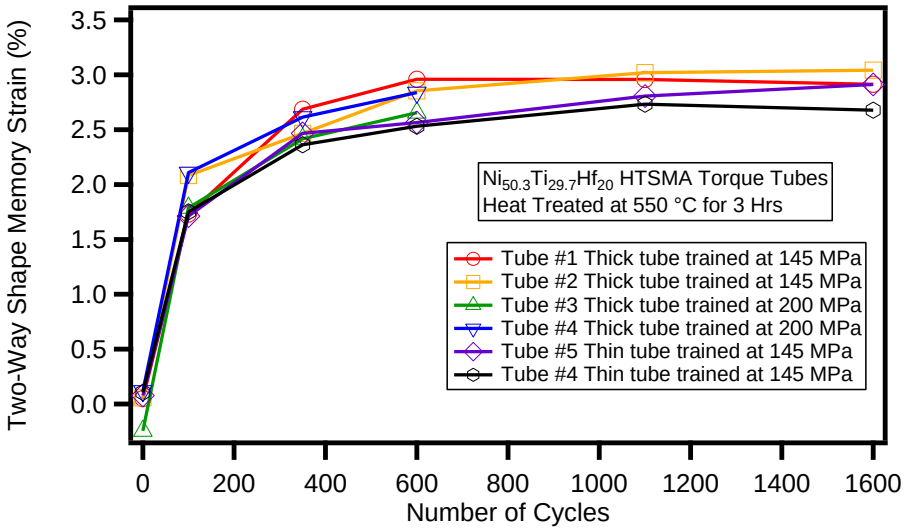

Figure 6.2 Evolution of TWSMS as a function of the number of cycles for the $Ni_{50.3}Ti_{29.7}Hf_{20}$ high temperature shape memory alloy torque tubes. It can be seen that TWSMS saturates after 600 cycles in all conditions. There is no significant effect of wall thickness or training stress level.

Evolution of the relevant strains in Tube-2 during the training is shown in Figure 6.1.b. Since the no load austenite (extrapolated angle for 0 MPa stress) is the reference state for the strain calculations, the strain values in austenite show the evolution of the remnant strain. The reduction in the actuation strain can also be seen between cycles 600 and 1600. It is noted that the accumulation of remnant strain is more significant in the first 400 cycles and decreases after that. Some small minimas and maximas in the actuation strain can be observed in Figure 6.1.b. These small changes are caused by the experiments of the characterization sequence performed at those points, and they do not have a significant influence on the overall evolution trend of the actuation strain. Indeed, after about 10 training cycles, the actuation strain reaches the values observed before the characterization sequence. Initial strain in austenite was 1.00 % (due to the elastic strain upon initial loading) and after 1600 cycles, it reached to 1.55 %. This shows that even under notably high shear stresses, the actuation response is stable in the present nano-precipitation hardened NiTiHf HTSMAs, i.e. remnant strain only evolves less than 1%.

The stability of the strain in martensite is better than that in austenite: the strain in the first cycle was 4.36 % while the strain after 1600 cycles was 4.61 %. The difference in the increase of two characteristic strains yields a reduction in actuation strain. One possible reason of this reduction is the stabilization of austenite, martensite or both. It is known from the literature [35,101–103] that plastic deformation or thermo-mechanical training can result in the stabilization of martensite above A_f temperatures. This stabilization is due to the local defects pinning the martensite boundaries and preventing martensite to transform back to austenite. In such cases increasing the upper cycle

temperature or low temperature annealing usually helps to relieve the remnant martensite. The DSC results shown in Figure 6.3 demonstrate a reduction in the transformation enthalpy which is an indication of the reduction in the martensitically transforming volume. This reduction also points out the stabilization of martensite, austenite or both. However, the stabilization of austenite has not been reported in the literature, to the best of the authors' knowledge. In the following sections, Transmission Electron Microscopy (TEM) investigations will show that the present torque tube samples, trained under shear stress, contain retained austenite phase at 100°C below the M_f temperature, contributing to the observed reduction in the transformation enthalpies.

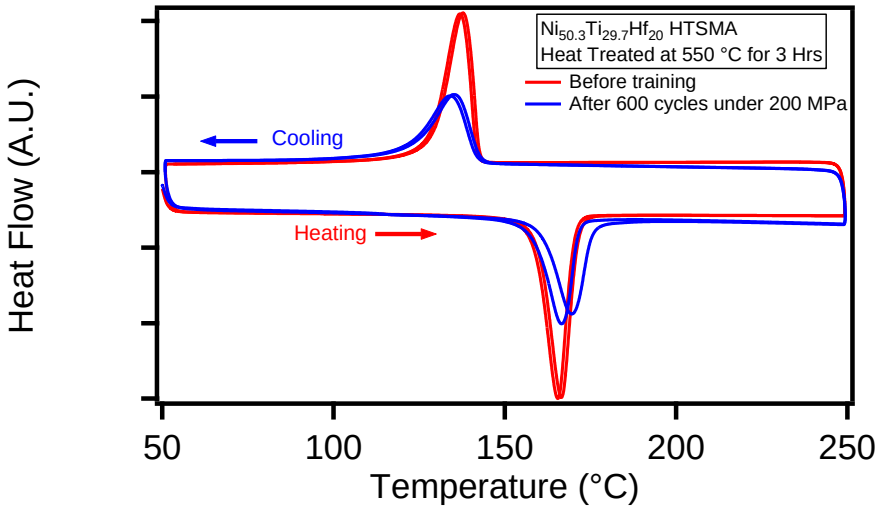

Figure 6.3 DSC results for the $Ni_{50.3}Ti_{29.7}Hf_{20}$ high temperature shape memory alloy torque tubes before and after thermo-mechanical training under 200 MPa shear stress for 600 cycles. While there is not a significant change in transformation temperatures, there is a reduction in the enthalpy of transformation which can be related to the stabilization of martensite and austenite.

6.4.2 Effect of Training Stress Level on the Evolution of TWSME

In order to determine the effect of applied training stress on the evolution of TWSME, two samples (Tube-3 and Tube-4) were trained under 200 MPa shear stress in addition to those trained under 145 MPa. Since it was shown above that 600 cycles is enough to stabilize the TWSME, the tubes were trained up to this particular number of cycles. The evolution of TWSME of the samples trained under 200 MPa and 145 MPa can be seen in Figure 6.5.a. The results shown are the average from the two identical tubes tested in each training stress level. Initial training cycles showed notable difference in the actuation strains between the tubes trained under 200 MPa and those trained under 145 MPa. This is likely due to the more intermediate characterization sequence steps and more associated number of cycles in the samples for 145 MPa training than those for 200 MPa training (for example, 35 MPa and 90 MPa experiments with 3 cycles under each stress, Table 1), leading to a training effect before the actual training under 145 MPa or 200 MPa starts. For the trained samples, however, there is no notable difference in either actuation strain or TWSMS between the samples trained under two different shear stresses. The evolution of TWSME and the actuation strain during training is comparable for high and

low shear stresses as can be seen in Figure 6.4.a and Figure 6.4.b. The evolution of TWSMS as a function of number of cycles has been presented in Figure 6.2. In Figure 6.2, the response of Tube-3 trained under 200 MPa is almost identical to other conditions. Tube-4, although identical to Tube-3, has slightly different response, namely the TWSMS is about 0.5% higher after 100 cycles, yet the overall trend in the dependence of TWSMS on the number of cycles is similar to other conditions. Therefore, it can be concluded that increasing training shear stress above 145 MPa does not notably change the TWSMS and the number of cycles to reach a particular TWSMS. As a result, it can be argued that 145 MPa shear stress is enough to maximally reorient martensite and further increasing the stress does not contribute to increasing the actuation strain.

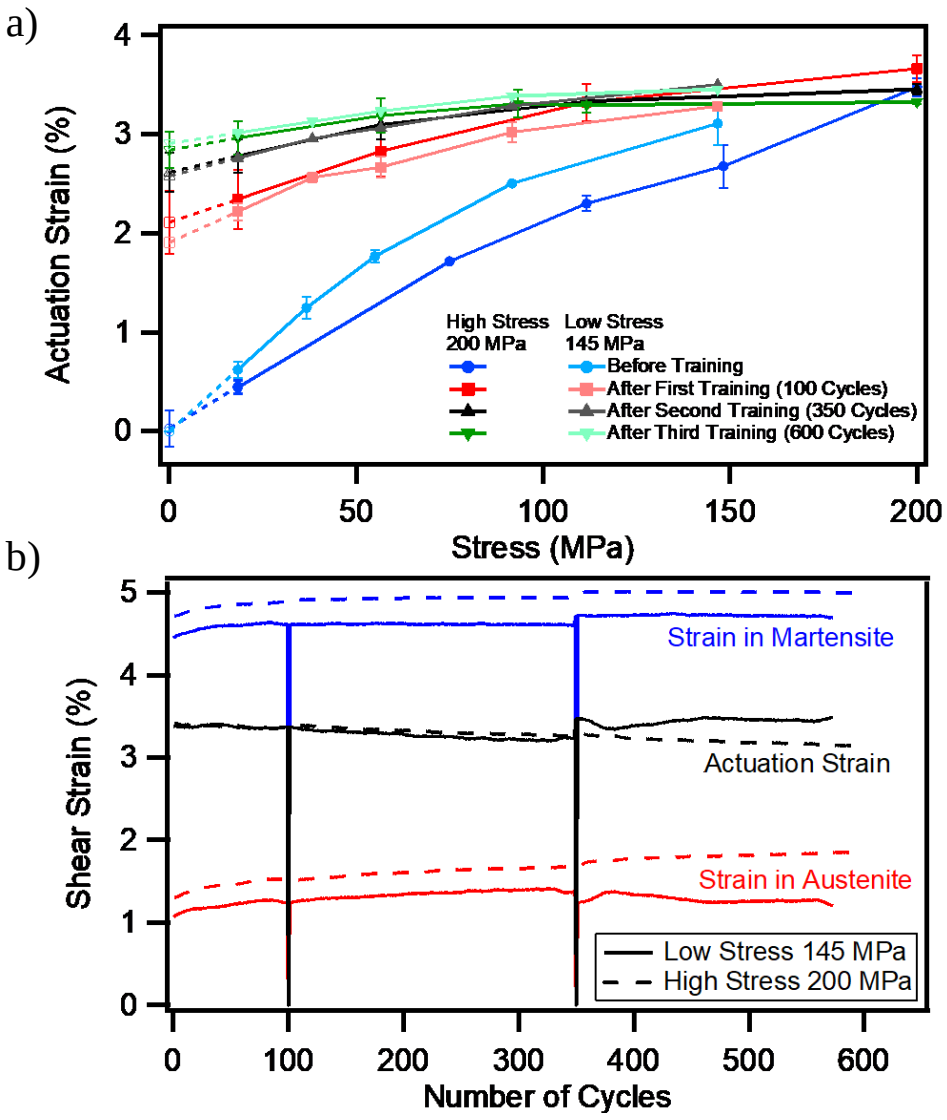

Figure 6.4 a) Shear strain vs. applied shear stress response of the $Ni_{50.3}Ti_{29.7}Hf_{20}$ high temperature shape memory alloy torque tubes trained under low stress, 145 MPa (Tube-1 and Tube-2 in Table 6.1) and high stress, 200 MPa (Tube-3 and Tube-4 in Table 6.1) during the "characterization sequence" after various number of thermo-mechanical training cycles demonstrating how actuation strains and TWSMS evolve with the number of training cycles. The results shown are the average from the two identical tubes tested in each training stress level. b) Evolution of critical strains with the number of cycles for high (200 MPa, Tube 3) and low (145 MPa, Tube 2) stress training

6.4.3 Effect of Sample Size on the Evolution of TWSME

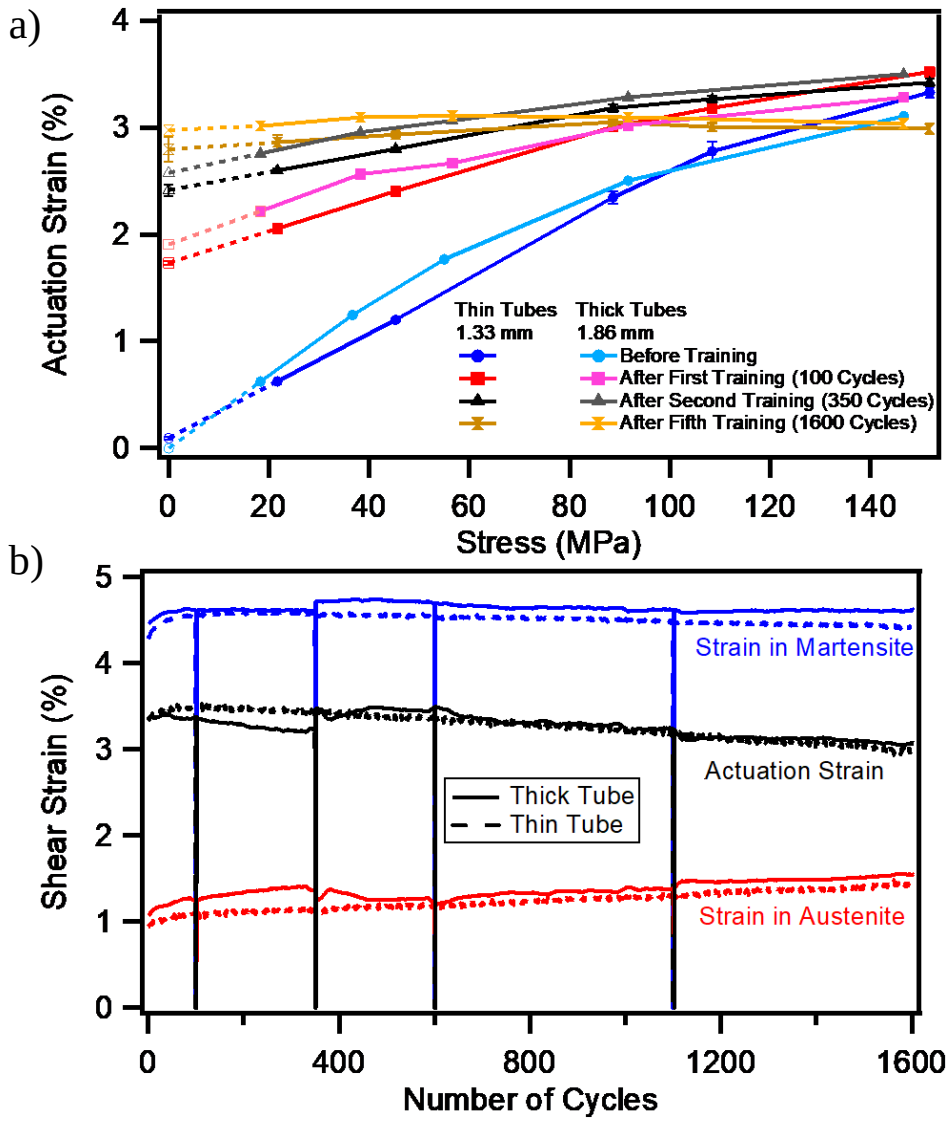

Figure 6.5 a) Shear strain vs. applied shear stress response of the $Ni_{50.3}Ti_{29.7}Hf_{20}$ torque tubes trained under 145 MPa with two different wall thicknesses. Thick walled tubes (Tube-1 and Tube-2 in Table 6.1) and thin walled tubes (Tube-5 and Tube-6 in Table 6.1) during the "characterization sequence" after various number of thermo-mechanical training cycles demonstrating how actuation strains and TWSMS evolve with the number of training cycles. The results shown are the average from the two identical tubes tested in each training stress level. b) Evolution of critical strains with the number of cycles for thick (Tube-2) and thin (Tube-5) walled tubes

In order to determine the effect of sample size on the training response and TWSME, in addition to the thick torque tube samples, thin torque tube samples (Tube-5 and Tube-6) were also trained. The evolution of TWSME and actuation strain in thin tubes can be seen in Figure 6.5.a and Figure 6.5.b, respectively, in comparison to the thick tubes. As compared to the response of the thick tubes, there is no significant difference in the actuation strains and the evolution of TWSMS as a function of the number of cycles, as can be seen in Figure 6.2. The evolution of the critical strains with the number of cycles can also be seen in Figure 6.5.b. Note that there is again no significant difference in the accumulated plastic strain. This suggests that thin-walled tube assumption and linear approximation are valid for the present tested conditions.

6.4.4 Microstructural Investigation

Transmission electron microscopy (TEM) was used to investigate the microstructural changes introduced by training in the NiTiHf high temperature shape memory alloy tubes. TEM observations of the samples before training show relatively large self-accommodated martensite variants containing a high density of spindle like H-phase precipitates (see [32,34] for more information on the H-phase), of about 8-25 nm in length and 4-10 nm in width, as shown in Figure 6.6.a and Figure 6.6.b. TEM investigations performed on the trained Tube-3 sample (the thick tube trained under 200 MPa for 600 cycles) reveal similar precipitate sizes and interparticle distances as shown in Figure 6.6.c and Figure 6.6.d. Moreover, four variants of the H-phase can theoretically form in these materials [32,34], which were observed in both trained and untrained

specimens. The SAEDPs has predominantly shown the same twinning modes in both trained and untrained samples: (011)-Type I and (001)-compound twinning [34] . These observations indicate that the particular training process used here did not bring about any significant growth or realignment of the nanoprecipitates nor a change in the martensite twinning modes.

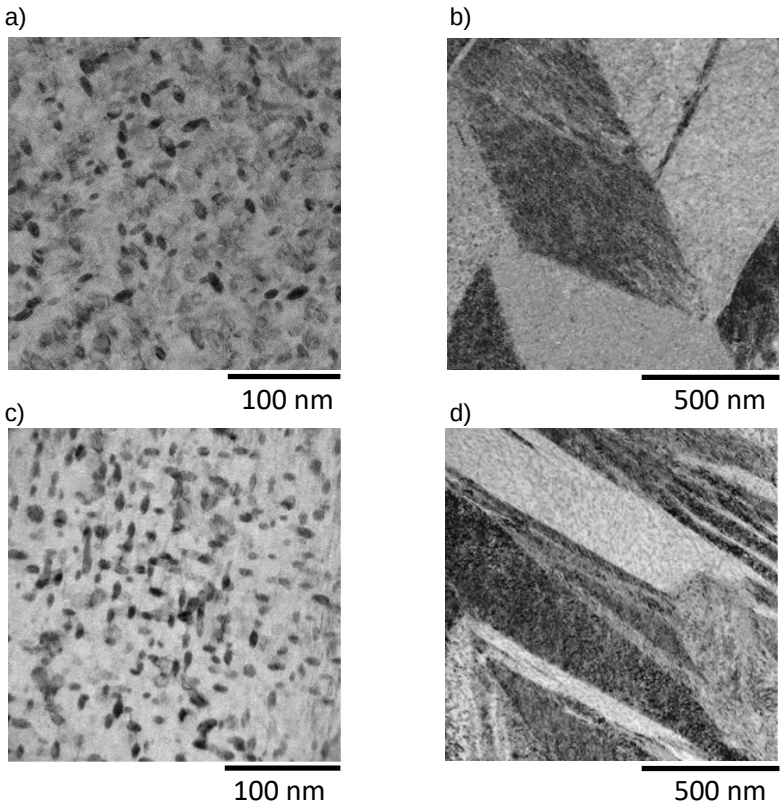

Figure 6.6 Bright field TEM images of the $Ni_{50.3}Ti_{29.7}Hf_{20}$ torque tubes before and after thermo-mechanical training under shear stress. a) Precipitate structure of the untrained material which was precipitation heat treated at 500°C for 3 hrs. b) Martensite structure of the untrained material shows large martensite variants in self-accommodated morphology, absorbing the precipitates. c) Precipitate structure of the trained material after 600 cycles under 200 MPa (Tube-3), basically showing that there is no notable change in precipitate size and morphology after training. d) Martensite morphology of the trained material (Tube-3).

On the other hand, the thermo-mechanical cycling notably changed the self-accommodated martensite morphology. In the untrained samples, the martensite variants are usually large and regularly spaced, and form different self-accommodating groups (Figure 6.6.b), whereas in the trained samples, there exist many regions showing a predominance of long and thin needles (less than 100 nm in width) of a few martensite variants with nearly-parallel intervariant boundaries. Figure 6.7 shows an example of such microstructure with predominant aligned variants extending across the grain boundaries. Such microstructure is typical in low temperature SMAs, such as NiTi, with well-developed TWSME, which is a result of the defect structures evolved during the training process.

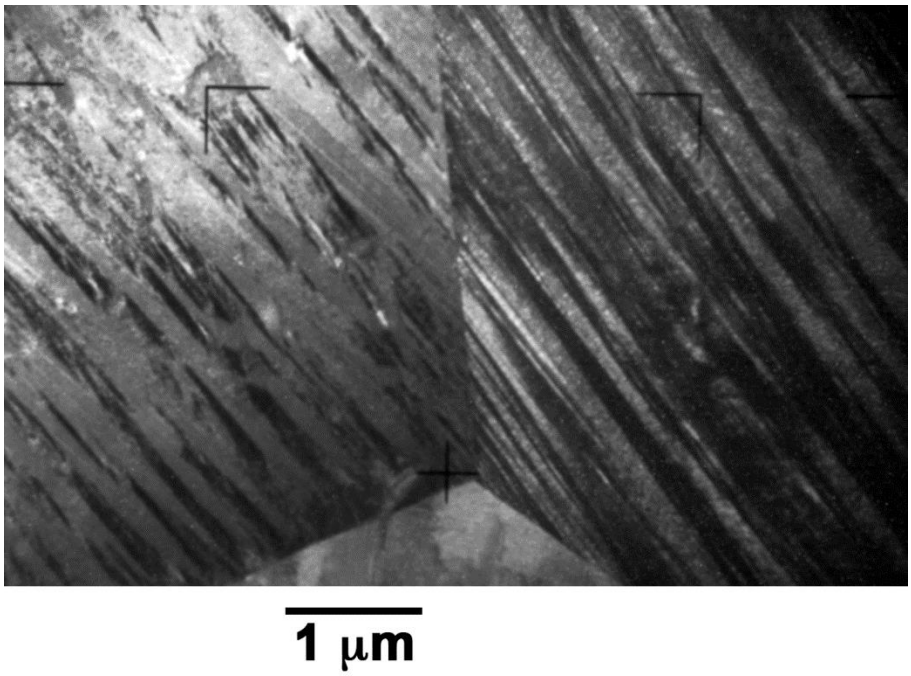

Figure 6.7 Bright-field TEM image of the $Ni_{50.3}Ti_{29.7}Hf_{20}$ high temperature shape memory alloy torque tubes after thermo-mechanical training under shear stress exhibiting large and thin martensitic plates, which leads to nearly parallel plates, even in different crystallographic grains.

Furthermore, in the trained samples, there were many regions exhibiting (011)-Type I twins together with additional overlapped domains showing oblique interfaces with respect to the twinning planes (Figure 6.8.a, from Tube-3. This particular microstructure differs from the typical arrays of (011)-twinned plates observed in edge-on conditions, in which all the twins show parallel interfaces (see [32] for the examples of the normal (011)-Type I twinning morphology). The microstructure shown in Figure 6.8.a has been studied by SAEDP (Figure 6.8.b-e) using very small selected area apertures. The SAEDPs of zones V1 and V2 (Figure 6.8.c and Figure 6.8.d) reveal two B19' variants with twinning relationship over the $(011)_{B19'}$ planes, which corresponds to the normal (011)-Type I

twinning. However, the V3 zones, which are interspersed in between the twinned martensite variants, can only be indexed as B2 austenite. Moreover, the orientation between the B19' variants and the V3 domains matches perfectly the orientation relationship between austenite and martensite. Therefore, Figure 6.8 demonstrates the existence of the areas that have not been transformed into martensite even at room temperature, 100°C below the M_f temperature, i.e. remnant austenite, as a consequence of the training process. The presence of this remnant austenite correlates well with the observed decrease of the actuation strain upon prolonged cycling (Figures. 6.1.b, 6.4.b and 6.5.b) as well as the decrease of the transformation enthalpy after the training (Figure 6.2).

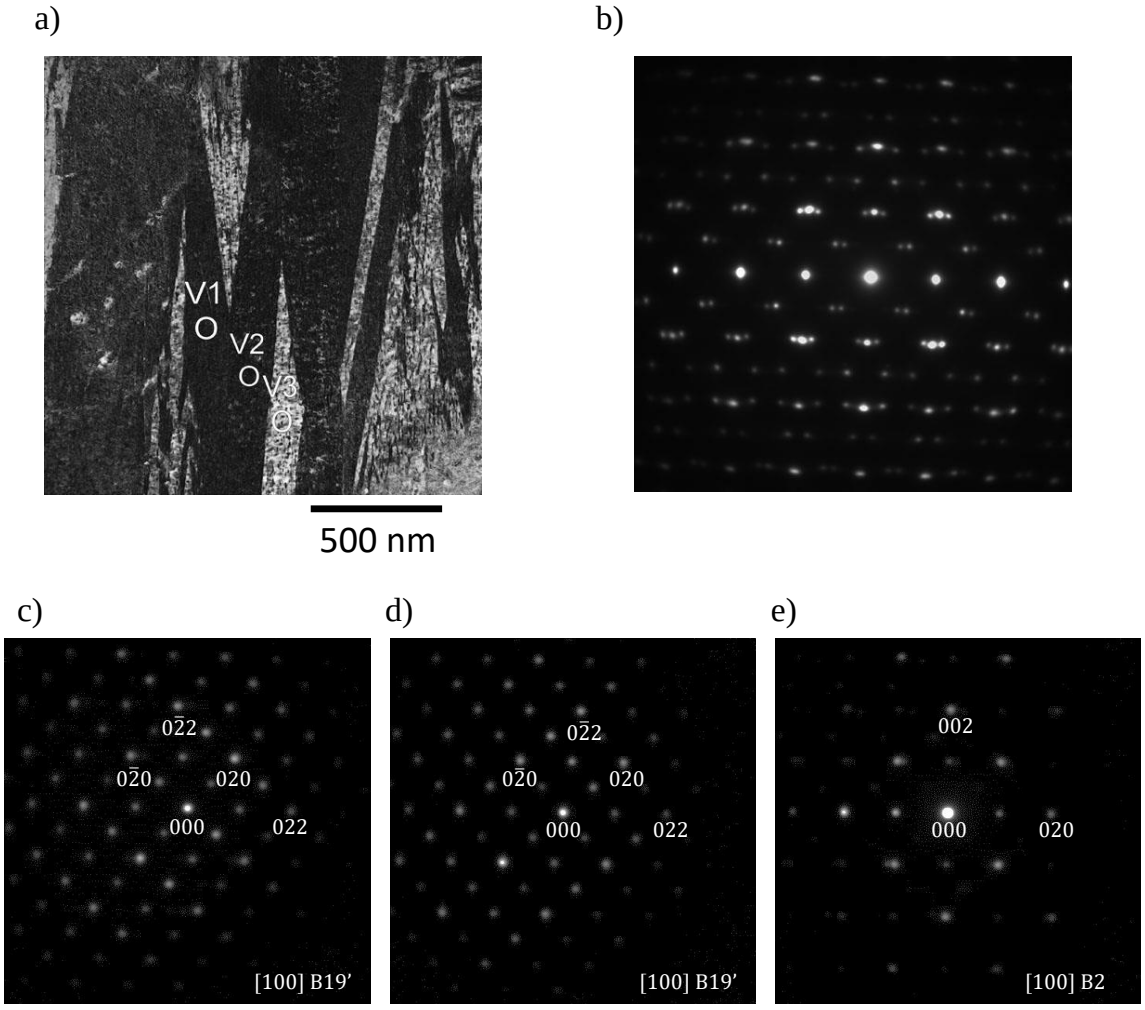

Figure 6.8 a) The bright field TEM image of the $Ni_{50.3}Ti_{29.7}Hf_{20}$ torque tubes after thermo-mechanical training under shear stress showing different martensite variants and remnant austenite at room temperature. b) Selected Area Electron Diffraction Pattern (SAEDP) of the entire region shown in (a). c) SAEDP from the region marked as V1, showing a martensite variant (B19'); d) SAEDP from the region marked as V2, showing a martensite variant (B19'); and e) SAEDP from the region marked as V3, showing remnant austenite (B2).

Another important microstructural feature observed in the trained sample (Tube-3) is the presence of dislocations interconnecting the nanoprecipitates as shown in Figure

6.9.a. They were not observed in untrained samples, thus the dislocations were created during the repeated martensitic transformation under stress. Figure 6.9.b presents an enlarged image taken under suitable conditions for imaging the (001)-compound internal twins, which are usually very thin in NiTiHf alloys containing nanoprecipitates. The dislocations appear with bright contrast in Figure 6.9.b. Interestingly, the image shows that the (001) twins are refined in the areas close to the dislocations and there is a discontinuity in the twin sequence at each side of the dislocation lines. Thus, these observations reveal the difficulty of martensite growth when the dislocations are present. The difficult martensite growth would explain the incomplete transformation on cooling and presence of remnant austenite in the trained materials at room temperature.

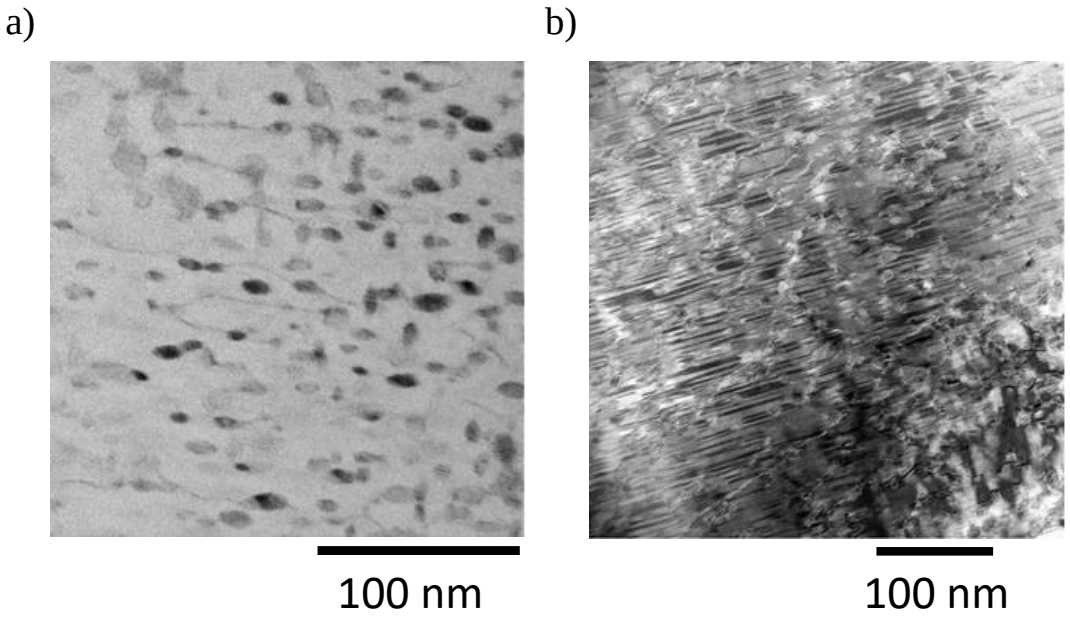

Figure 6.9 Bright field TEM images of the $Ni_{50.3}Ti_{29.7}Hf_{20}$ torque tubes after thermo-mechanical training under shear stress showing dislocations. a) Dislocations between precipitates and b) refined martensite twins interrupted by dislocations.

As it was already noted, TWMSE has been traditionally associated with the defects generated, or modified, during training. For instance, growth of aligned precipitates by aging under stress can generate TWSME by means of the aligned internal stress created by the precipitates, which select certain variants over the other. The dislocations created by the austenite-martensite front moving back and forth during a training process based on the repeated transformation cycling, also create internal stresses which favors certain variants over others, yielding to TWSME [104]. Finally, retained martensite plates of suitable variants can also contribute to TWSME by promoting growth of the retained plates instead of nucleation of other variants [105–107]. In the present work, the TEM results rule out any precipitate growth or re-orientation as a possible responsible factor of the TWSME observed. On the other hand, the TEM results clearly demonstrate dislocation formation during training, which may contribute to the observed TWSME. It is interesting to note that TWSMS saturates at ~600 cycles in the present NiTiHf material and further training does not significantly increase the amount of TWSMS for most of the samples (Figure 6.2). Therefore, the dislocation density observed in the present work (Figure 6.9) should be close to the maximum that can be reached in this alloy and initial thermal treatment. Such dislocation density is rather low in comparison with the dense dislocation tangles typically observed in solution heat treated (precipitate-free) Ni-Ti alloys after a few transformation cycles [108–110]. Moreover, other alloys in precipitate-free condition, such as CuZnAl [111] and NiTiPd [112], do not require this many cycles to reach the TWSMS saturation. These observations demonstrate the strengthening effect caused by the H-phase nanoprecipitates in $Ni_{50.3}Ti_{29.7}Hf_{20}$, which act as barriers to the dislocation

formation and motion, and may justify the need for prolonged training treatments to induce the TWSME in this material.

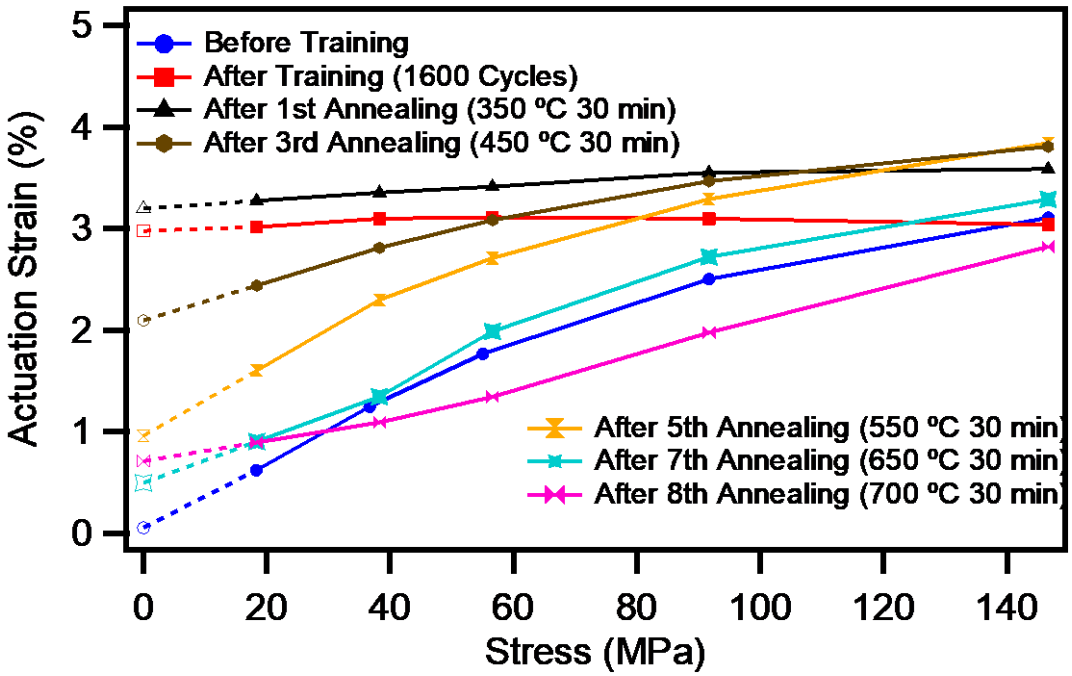

Figure 6.10 Two-way shape memory strain (TWSMS) and actuation strain under various stresses in thermo-mechanically trained $Ni_{50.3}Ti_{29.7}Hf_{20}$ torque tube (Tube-2) after static annealing treatments at various temperatures for 30 min. The TWSMS is stable at temperatures up to 400°C and completely deteriorates above 600°C. For the sake of clarity, the responses from annealing steps 400, 500 and 600 are not shown.

Therefore, it is reasonable to deduce that the low amount of dislocations formed after training could be not enough to develop the high levels of TWSME observed in the present samples, and the mechanism based on retained martensite plates (unable to back-transform to austenite at the upper cycle temperature) could also play a role, in

combination with the dislocations. The study of the TWSME stability at elevated temperatures (c6.4.5 below) indicates that all the retained martensite plates and dislocation arrays are stable up to 400ºC. Above this temperature, the retained martensite plates, with various degrees of stabilization, progressively re-transform to austenite and the dislocations tend to redistribute and annihilate, leading to a gradual decrease of the TWSMS with the increasing aging temperatures.

6.4.5 Stability of TWSME at Elevated Temperatures

Since TWSME in SMAs is a result of defects and internal residual stresses, it is important to understand the evolution of TWSME as a function of temperature and to determine its stability at high temperatures, especially above 0.4 T_H (T_H=homologous temperature), where diffusional mechanisms start playing significant roles in materials response. This is particularly critical for HTSMAs due to their high operating temperatures as compared to conventional SMAs. For this purpose, a thick walled torque tube sample (Tube-2) was annealed at a set of temperatures after the long training procedure (Figure 6.1) and the characterization sequence was utilized after each step of annealing to evaluate the evolution of TWSMS and actuation strain under 145 MPa. Figure 6.10 summarizes the results after selected annealing treatments. As can be seen in Figure 6.10, after 350 and 400°C annealing treatments, there is no significant change in TWSME response. The slight increase in the TWSMS after these annealing treatments as compared to the TWSMS right after the training is probably because of the reverse transformation of remnant martensite and thus increase in the transforming volume. On the other hand,

above 450°C up to 600°C annealing treatments, there was a sequential reduction in TWSMS. In these cases, the sample was further trained for 100 cycles before the next annealing step to stabilize the actuation strain under 145 MPa again. After annealing at 650°C for 30 min, TWSMS was reduced down to 0.49 % and actuation shear strain vs. stress response was almost identical to the initial behavior before the training. This indicates that the annealing at 650 °C for 30 min. is sufficient to relieve all the internal stresses stored during the thermo-mechanical training under 145 MPa. In contrast, after the annealing at 700 °C for 30 min, actuation strain levels at a given stress are lower (shown in Figure 6.10) than those before training, indicating that the microstructure changed significantly after this annealing treatment. These results indicate that TWSME in nano-precipitation hardened NiTiHf HTSMAs is stable up to 400°C above which the internal residual stresses start relaxing, because of the annealing of the defects responsible from these stresses.

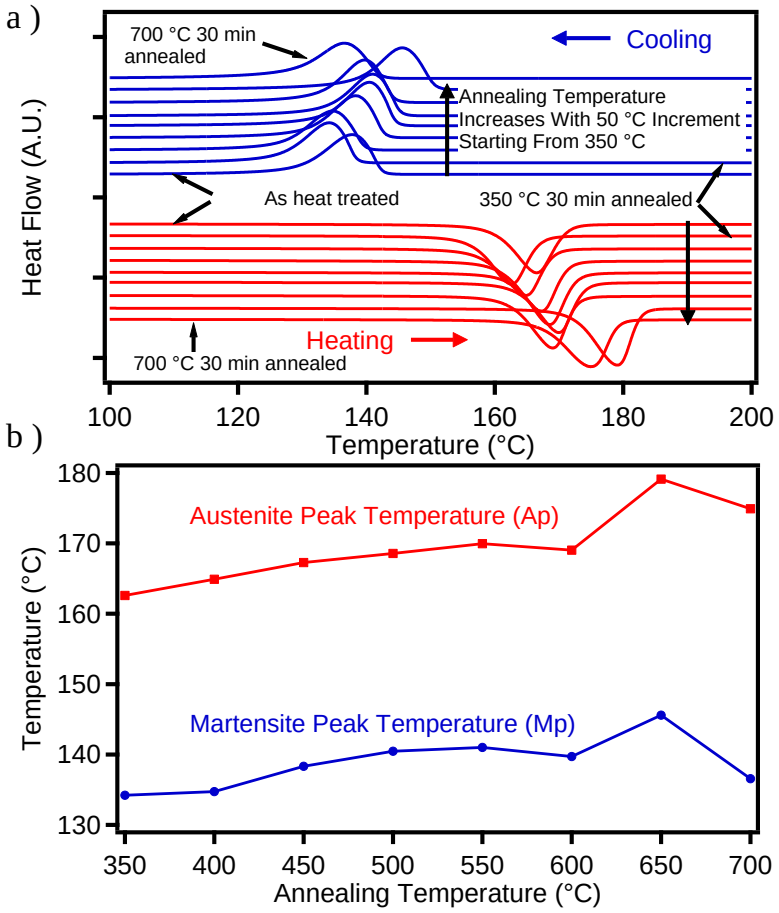

Figure 6.11 a) DSC results of the untrained and trained + annealed samples of the $Ni_{50.3}Ti_{29.7}Hf_{20}$ torque tubes. The most inward pair is for the as precipitation heat treated, untrained material. The shifted curves to outside are for annealing steps. Annealing was done for 30 minutes for each step and started from 350 up to 700°C with 50 °C increments. b) Martensite (M_p) and austenite (A_p) peak temperatures are plotted as a function of the annealing temperature. Note that there is no significant change up to 650 °C annealing step. At and above 700 °C heat treatment transformation temperatures reduced to previous levels but it is suspected that microstructure has already been changed.

In order to better assess potential microstructural changes that may occur during the static annealing experiments performed here, we have conducted DSC experiments on the annealed trained samples to determine the transformation temperatures. In the present alloy, there should be two competing changes in the microstructure: new formation or

growth of nano-precipitates and relaxation of internal stresses through annihilation of dislocations, or diffusion of point defects, or transformation of remnant martensite into austenite. Since transformation temperatures in SMAs are quite sensitive to even small microstructural changes [112–114], DSC can sometimes provide powerful evidence of the type of microstructural changes. Figure 6.3 and Figure 6.11 show the DSC results of the samples before and after training and after various annealing heat treatments. The results indicate that no significant change occurs on transformation temperatures after annealing up to 600 °C for 30 minutes. However, above that temperature, the transformation temperatures notably change. This indicates that precipitate structure in the material may have changed.

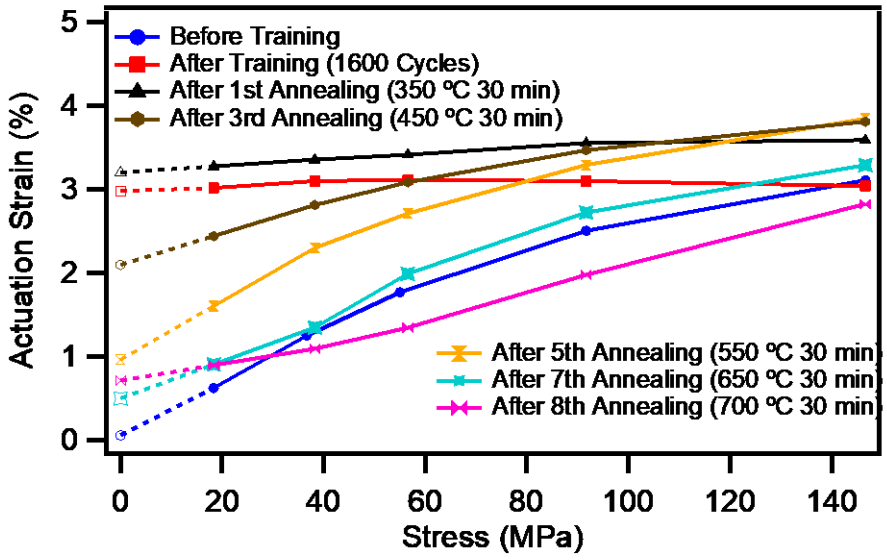

Figure 6.12 Two-way shape memory strain (TWSMS) and actuation strain under various stresses in thermo-mechanically trained $Ni_{50.3}Ti_{29.7}Hf_{20}$ torque tube (Tube-2) after static annealing treatments at various temperatures for 30 min. The TWSMS is stable at temperatures up to 400°C and completely deteriorates above 600°C. For the sake of clarity, the responses from annealing steps 400, 500 and 600 are not shown

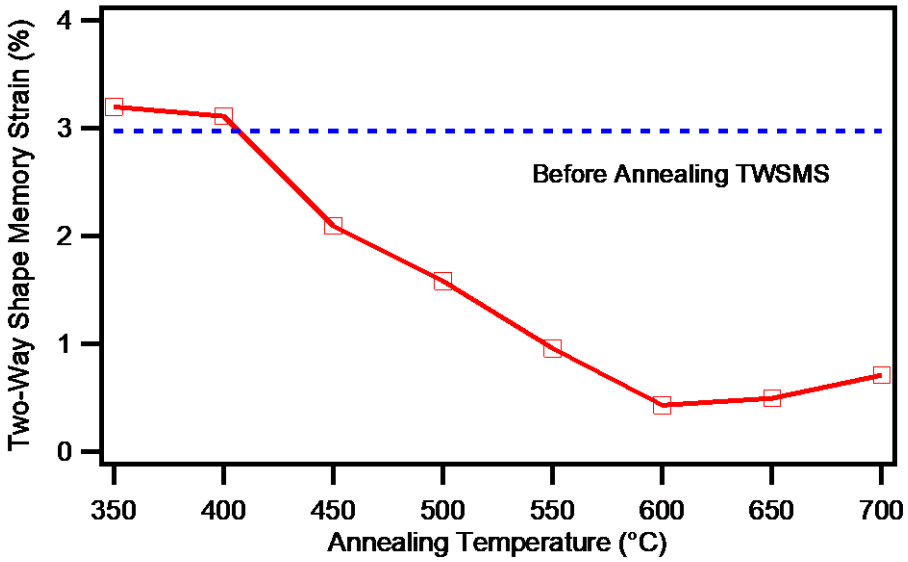

Figure 6.13 Change in Two-Way Shape Memory Strain (TWSMS) as a function of the annealing temperatures for the $Ni_{50.3}Ti_{29.7}Hf_{20}$ high temperature shape memory alloy tubes after the thermo-mechanical training. Each annealing step is for 30 minutes at given temperature. As trained sample's TWSMS has been added with blue dashed line to be a reference. There is a slight increase after first annealing which may be associated with the dissolution of retained martensite, thus liberating more material to go through the phase transformation.

Using the data in Figure 6.12, the evolution of TWSMS as a function of annealing temperature is plotted in Figure 6.13, which shed light onto possible mechanisms responsible for the origin of TWSME in these materials. As mentioned earlier, the three possible reasons of TWSME are aligned nano-precipitates, remnant martensite, and dislocations and point defects or some combination of these mechanisms. The microstructural investigations with TEM demonstrated that there is no significant change in the precipitate structure such as size and orientation after training suggesting that possible internal stress field around any aligned precipitates cannot be a mechanism

responsible for TWSME here. Annealing can induce precipitate growth, and since the precipitates grow under no stress in the present case, this should decrease TWSMS. However, the change in the precipitate size and fraction should also alter the composition and transformation temperatures of the matrix, and since the transformation temperatures did not significantly change after annealing below 600 °C, the contribution of the precipitate growth to the change in TWSME should be insignificant for the present cases. If the main reason of TWSME in present material would have been remnant martensite, a sudden drop in actuation strain would be expected above a critical annealing temperature. However, the gradual decrease in TWSMS with increasing annealing temperature in Figure 6.13 suggests that the main source of two-way shape memory effect on the present materials is dislocations and point defects that they gradually annihilate, possibly following an Arrhenius type temperature dependence.

6.5 Summary and Conclusions

It was found that under 200 MPa, 600 thermal cycles are enough to reach a two-way shape memory strain (TWSMS) as high as 2.95 %, which was shown to be stable upon annealing up to 400 °C for 30 minutes. This TWSMS is 85 % of the maximum measured actuation strain under 200 MPa. The microstructure after thermo-mechanical training was investigated using transmission electron microscopy (TEM), which did not indicate a significant change in precipitate structure and size after the training. However, small amount of remnant austenite was revealed 100 °C below the martensite finish temperature, with notable amount of dislocations. Overall, it is found that nano-precipitation hardened

$Ni_{50.3}Ti_{29.7}Hf_{20}$ shows relatively high TWSMS after much less number of training cycles as compared to nickel lean NiTiHf compositions. Although binary NiTi shows TWSME after less number of training cycles plastic strain continues to accumulate (unstable) up to 1000 -1500 cycles, where precipitation hardened NiTiHf has stable TWSMS after 600 cycles. Tube wall thickness and training stress levels have been found to have negligible effect on shape memory strains and number of cycles to reach the desired training level, for the ranges studied. In the light of the results obtained, the main findings can be summarized as follows:

1. TWSME can be induced in the precipitated hardened Ni-rich NiTiHf HTSMAs by repetitive thermos-mechanical cycling. TWSME saturates in about 600 cycles and further cycling reduces the actuation strain under stress.
2. The chosen training shear stress levels (145 MPa and 200 MPa) and the tube wall thicknesses have not produced notable differences in TWSME. The latter can be attributed to validity of thin walled tube assumption and linear approximation to calculate stresses and strains in the present conditions.
3. TEM observations have demonstrated the existence of remnant austenite after the training, which leads to the reduction in actuation strain with thermo-mechanical cycling after training. TEM images have also revealed a moderate level of dislocation accumulation interconnecting the nano-precipitates. The dislocation arrays formed during cycling and, eventually, retained martensite are considered to be the origin of TWSME in these alloys.

4. TWSME is thermally stable upon annealing at temperatures up to 400 °C after 30 min heat treatments. The thermal treatments from 450 °C to 650 °C gradually decrease the two-way shape memory strain. Annealing at 650 °C for 30 min yields to actuation response close to that of the untrained material whereas the annealing at 700°C for 30 min notably changes the microstructure and the transformation temperatures, resulting in partial martensitic transformation during cycling between the selected temperature range for testing in the present study.

7. FRACTURE TOUGHNESS MEASUREMENT OF SHAPE MEMORY ALLOYS

7.1 Overview

Fracture toughness of shape memory alloys (SMAs) were studied in this section. Different fracture toughness measurement methods were considered in this study namely linear elastic fracture mechanics (LEFM) and elasto-plastic fracture toughness mechanics (EPFM). Applicability of those method are investigated. Effect of phase constitution is also studied. Samples are tested at martensitic and austenitic temperatures.

7.2 Introduction

Fracture toughness is an important metric used in material selection to an application. It can be defined as materials resistance to crack growth. Despite its importance, it is not a mature field in SMAs because of unique properties of those alloys. First of all, SMAs show strong non-linearity in stress strain diagrams at relatively earlier stages. This makes sample sizes prohibitively large when LEFM approach is desired to be used. Alternatively EPFM can be used but nature of non-linearity is not dislocation plasticity as in most ductile material but rather phase transformation or twining.

Fracture toughness of shape memory alloys, including effect of phase constitution was studied in the literature but only LEFM approach were considered. There are several work proposing and using modified linear elastic or elasto-plastic approaches but those

studies hadn't studied effect of phase constitution. The aim of this work is to combine two types of investigations and study effect of phase constitution while also considering different fracture mechanics approaches. Moreover effect of sample size on measured fracture toughness values is also studied. It is hypothesized in this study that phase transformation and twinning can be treated as plasticity for fracture toughness measurement purposes. This way a better comparison of effect of phase constitution or material system can be achieved.

7.3 Experimental Procedure

Two composition of materials were used in this study. Ni lean NiTi ($Ni_{49.5}Ti_{50.5}$) and Ni rich NiTiHf ($Ni_{50.3}Ti_{29.7}Hf_{20}$), details of which described in sections 3.2.3 and 3.2.2 respectively, was used in this study. Fracture toughness tests at fully martensitic stage and austenitic stage were measured on CT for $Ni_{49.5}Ti_{50.5}$ and DCT for $Ni_{50.3}Ti_{29.7}Hf_{20}$ samples based on ASTM standard E1820. To ensure material has single phase in the beginning of the test, fully martensitic samples were heated up test temperature from M_f-20 where austenitic samples were cooled down from A_f+60. All three methods (linear elastic fracture mechanics, elasto-plastic fracture mechanics simple method and R curve behavior) to process data employed in this work when applicable. Details about test system and experimental procedures can be found in section 3.2.6.

Mechanical properties which are relevant for fracture toughness such as yield stress and elastic modulus can be seen in Table 7.1. Stress strain curves at upper and lower cycle temperatures can be seen in Figure 7.1. Note that $Ni_{49.5}Ti_{50.5}$ shows good ductility

up to 40 % and at A_f+60 it does not show super elasticity. The test on 75 °C was done at 100 % austenitic state by heating up to a temperature above A_f (170 °C) and cooled down to 75 °C. On the other hand $Ni_{50.3}Ti_{29.7}Hf_{20}$ shows lower ductility around 6.5 % in martensitic state and 16 % in austenitic state.

Table 7.1 Critical mechanical properties that is necessary for fracture toughness measurement. Note that yield stress (σ_{ys}) in equations are taken to be martensite reorientation stress (σ_{mr}) or stress induced martensitic transformation stress (σ_{sim}) depending on test temperature.

Material	Temperature (°C)	E (GPa)	σ_{sim} or σ_{mr} (MPa)	σ_{uts} (MPa)	ε_{uts} (%)
$Ni_{49.5}Ti_{50.5}$	25	45.5	168.9	880.3	40.5
	75	52.7	100.2	855.2	36.2
	170	67.0	319.8	623.3	20.95
$Ni_{50.3}Ti_{29.7}Hf_{20}$	25	58.3	507.5	1263.6	6.94
	100	56.2	446.1	1128.4	6.55
	200	68.7	456.8	1282.3	16.04

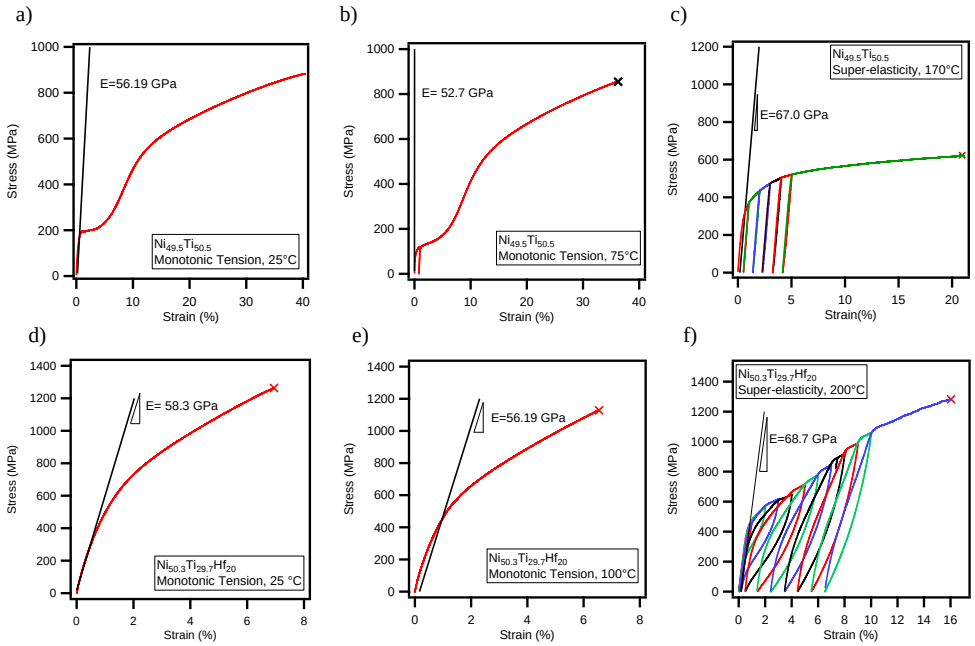

Figure 7.1 Monotonic tension tests for $Ni_{49.5}Ti_{50.5}$ and $Ni_{50.3}Ti_{29.7}Hf_{20}$ that are tested in this work. a) Stress strain at room temperature on $Ni_{49.5}Ti_{50.5}$ b) Stress strain at 75 °C on $Ni_{49.5}Ti_{50.5}$ c) Stress strain at 170 °C on $Ni_{49.5}Ti_{50.5}$ d) Stress strain at room temperature on $Ni_{50.3}Ti_{29.7}Hf_{20}$ e) Stress strain at 100 °C on $Ni_{50.3}Ti_{29.7}Hf_{20}$. f) Stress strain at 200 °C on $Ni_{50.3}Ti_{29.7}Hf_{20}$

Test matrix for the $Ni_{49.5}Ti_{50.5}$ samples studied in this section can be seen in Table 7.2. In fully martensitic fracture toughness tests of $Ni_{49.5}Ti_{50.5}$, to determine effect of sample thickness on measured values, thicknesses ranging from 1.5 to 3.5 mm were tested. After initial screening more tests conducted in 3 mm thickness to get statistically sound comparisons. In austenitic fracture toughness tests of $Ni_{49.5}Ti_{50.5}$ only 2 tests conducted so far. Note that two of the samples with the smallest thicknesses (NiTi_ASR_005 and NiTi_ASR_011) failed to be tested properly. The sample with 1.5 mm thickness buckled

before stable crack growth. The data was intact to process for linear elastic fracture mechanics but not for elasto-plastic fracture mechanics since out of plane displacement also effects crack mouth opening. The sample with 1 mm thickness developed a crack between loading pin hole and side of the sample thus failed from there instead of growing crack from the notch.

Table 7.2 Experimental test matrix for $Ni_{49.5}Ti_{50.5}$ with sample code, test temperature, thickness and status of the experiment.

Sample Code	Test Temperature (°C)	Thickness (mm)	Status
NiTi_ASR_001	25	3.31	Successfully Tested
NiTi_ASR_002	25	2.95	Successfully Tested
NiTi_ASR_003	25	3.38	Successfully Tested
NiTi_ASR_004	25	2.86	Successfully Tested
NiTi_ASR_005	25	1.50	Test Failed
NiTi_ASR_006	25	2.39	Successfully Tested
NiTi_ASR_007	25	1.84	Successfully Tested
NiTi_ASR_010	25	2.89	Successfully Tested
NiTi_ASR_011	25	1.00	Test Failed
NiTi_ASR_012	25	2.95	Successfully Tested
NiTi_ASR_013	170	2.42	Successfully Tested
NiTi_ASR_017	170	3.21	Successfully Tested
NiTi_ASR_021	25	2.99	Successfully Tested
NiTi_ASR_022	25	2.97	Successfully Tested

A smaller test matrix was utilized for $Ni_{50.3}Ti_{29.7}Hf_{20}$ samples which can be seen in Table 7.3. Two samples were tested at 100 °C which is M_f-20 and three samples were tested at 200 °C which is A_f+15. Nominal thickness of all samples were 3.5 mm, but

because samples mechanically polished to 1600 grid before testing, thickness varies slightly. All tests were successfully completed.

Table 7.3 Experimental test matrix for $Ni_{49.5}Ti_{50.5}$ with sample code, test temperature, thickness and status of the experiment.

Sample Code	Test Temperature (°C)	Thickness (mm)	Status
NiTiHf_ASR_002	100	3.48	Successfully Tested
NiTiHf_ASR_003	100	3.40	Successfully Tested
NiTiHf_ASR_004	200	3.48	Successfully Tested
NiTiHf_ASR_005	200	3.44	Successfully Tested
NiTiHf_ASR_006	200	3.40	Successfully Tested

7.4 Results

7.4.1 Measuring Fracture Toughness of NiTi at Martensitic Range

Force displacement curves of all 10 tests can be seen in Figure 7.2. Note that maximum force changes with thickness and pre-crack length. The fracture toughness values obtained by all three methods can be seen in Table 7.4. Although J integral values normally reported in kJ/m^2 unit, for comparison purposes stress intensity values in $MPa\sqrt{m}$ unit were calculated. The values calculated by LEFM had an average of 39.4 ± 2.7 $MPa\sqrt{m}$. On the other hand values calculated by two EPFM were 131.9 ± 27.9 and 154.6 ± 34.0 kJ/m^2 for simple and R-curve methods respectively. The converted values to stress intensity factor were 92.0 ± 9.8 and 99.6 ± 10.9 $MPa\sqrt{m}$.

Table 7.4 Summary of all fracture toughness tests on $Ni_{49.5}Ti_{50.5}$ run at room temperature. Units of K values are ($MPa\sqrt{m}$) and J values are (kJ/m^2)

Sample Code	Precrack Length (mm)	Thickness (mm)	Fracture Toughness Values				
			LEFM	EPFM (simple)		EPFM (R-Curve)	
			K_I	J_C	K_{JC}	J_{IC}	K_{JIC}
NiTi_ASR_001	10.53	3.31	39.5	152.4	99.4	152.9	99.6
NiTi_ASR_002	10.45	2.95	34.5	103.8	82.1	120.2	88.3
NiTi_ASR_003	11.10	3.38	42.2	98.8	80.0	109.1	84.1
NiTi_ASR_004	9.46	2.86	41.2	177.3	107.2	168.6	104.6
NiTi_ASR_006	10.00	2.39	38.4	113.3	85.7	134.0	93.2
NiTi_ASR_007	9.56	1.84	38.6	146.5	97.5	175.9	106.8
NiTi_ASR_010	9.77	2.89	43.3	162.3	102.6	209.9	116.7
NiTi_ASR_012	8.90	2.95	40.6	137.3	94.4	201.6	114.3
NiTi_ASR_021	9.75	2.99	36.8	98.4	79.9	146.4	97.4
NiTi_ASR_022	9.95	2.97	38.5	129.0	91.5	127.2	90.8

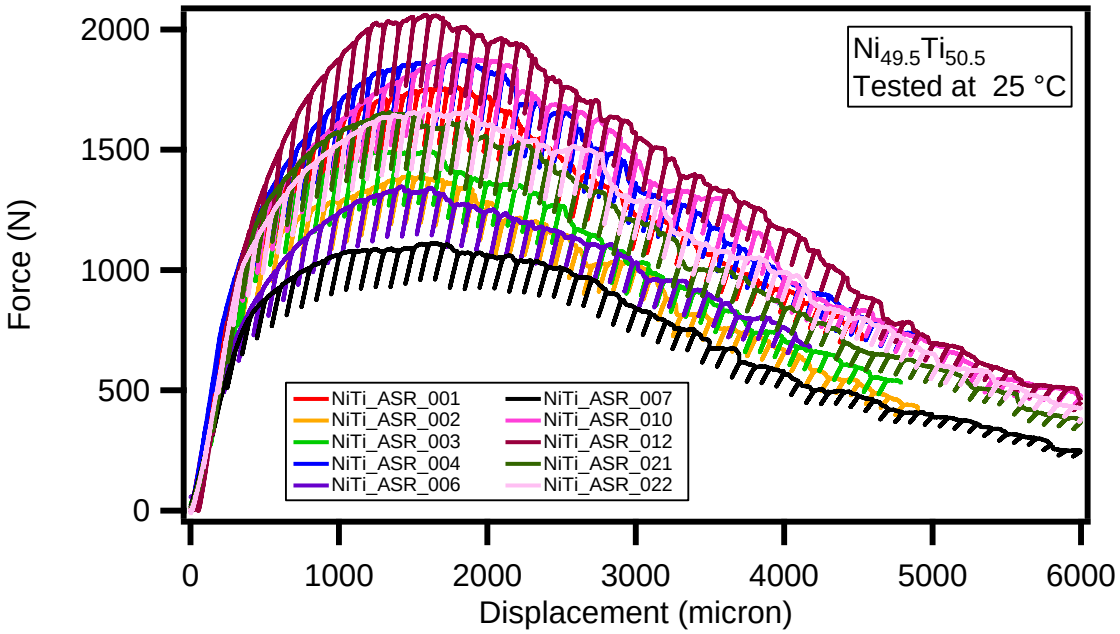

Figure 7.2 Force vs displacement curves for all fracture toughness tests on $Ni_{49.5}Ti_{50.5}$ done at room temperature.

To investigate measured fracture toughness values dependence to sample thickness, a set of thicknesses were tested. Fracture toughness values calculated by 3 method plotted with respect to sample thickness in Figure 7.3. Note that, although linear elastic fracture mechanics approach does not satisfy multiple criteria, it produces the most repeatable values. There is no significant change in fracture toughness with changing thickness in tested range.

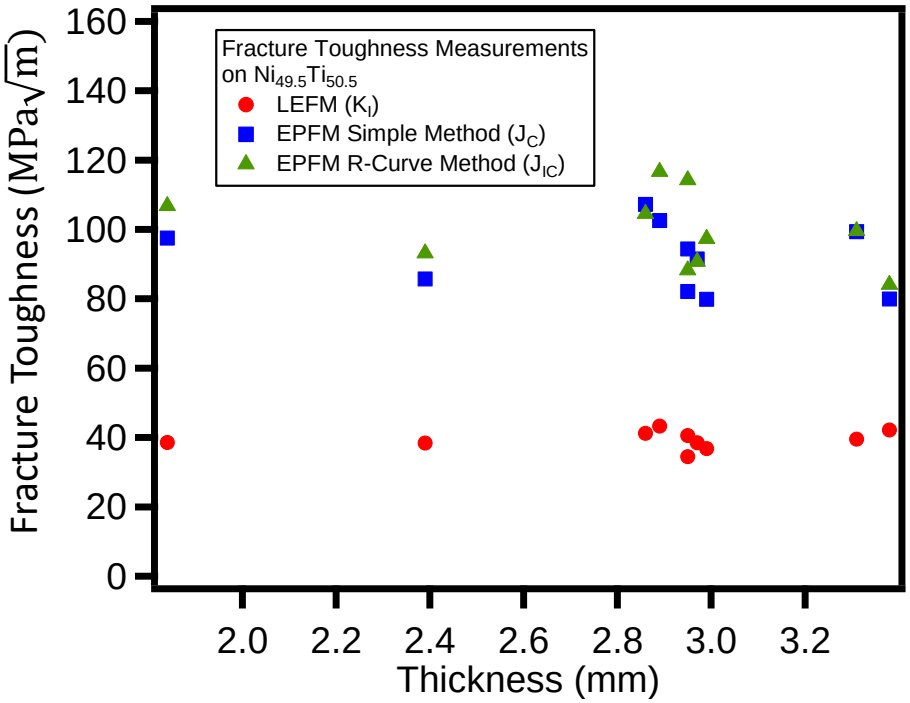

Figure 7.3 Fracture toughness values of $Ni_{49.5}Ti_{50.5}$ calculated with three methods (LEFM, EPFM simple and R-curve methods) as a function of thickness.

ASTM standard E1820, specifies several condition for each method as acceptance criteria. Those criteria were evaluated for all three methods to determine compliance of measured values to the standard. Those conditions can be found in detail in section 3.2.5. Minimum thickness or length of unbroken ligament for linear elastic fracture mechanics approach to be applicable is calculated to be 135 mm calculated by equation 3.6 for $Ni_{49.5}Ti_{50.5}$ at room temperature. Note that it is significantly bigger than samples used in this study and is prohibitively large. Acceptance criteria for EPFM approach were also evaluated. According to the standard, for values obtained by simple method to be accepted stable crack growth should be limited by following equation 3.9. The maximum acceptable crack growth before instability for $Ni_{49.5}Ti_{50.5}$ at room temperature is calculated to be 0.32 mm. Note that in our experiments stable crack growth consists to a much greater extend. Minimum thickness and length for unbroken ligament is also specified by equation 3.10. The minimum thickness for simple EPFM method for $Ni_{49.5}Ti_{50.5}$ at room temperature is 25.1 mm. Note that our thickness and unbroken ligament length is much smaller and are in the ranges of 1.5-3.5 and 9-11 mm respectively.

Lastly according to acceptance criteria for R curve behavior, minimum thickness and length of unbroken ligament should be calculated by equation 3.14. When the value was calculated for $Ni_{49.5}Ti_{50.5}$ at room temperature, minimum thickness and unbroken ligament must be 2.95 mm. Note that this is an order of magnitude smaller than simple method and all the criteria for R curve elasto-plastic approach are satisfied.

Digital image correlation (DIC) is used to determine two dimensional (2-D) strain fields. Details regarding to DIC can be found in section 3.2.9. A representative DIC image

can be seen in Figure 7.4. Note that significant amount of deformation is observed and morphology resembles plastic zone in regular structural materials. Yet because of relatively lower value of martensite re-orientation stress, apparent plastic zone has a large size. As crack grows, stress relaxation occurs beyond crack tip. Because the material tested at martensitic temperatures deformation is permanent and does not recovers.

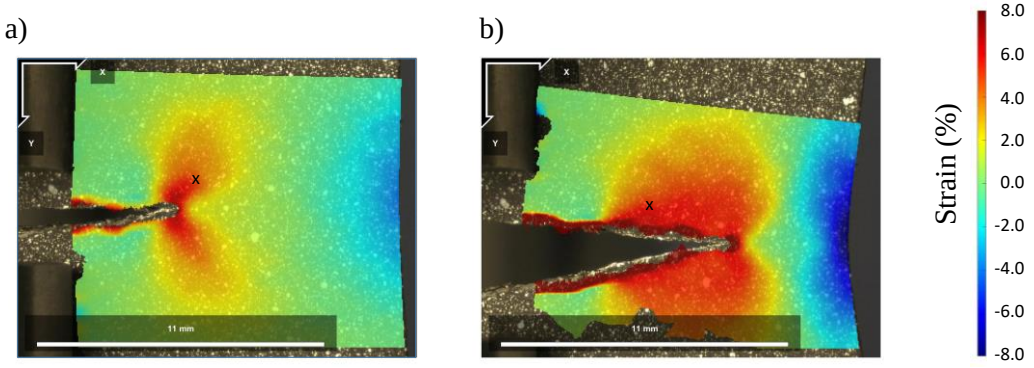

Figure 7.4 Digital image correlation showing strain in y direction for two crack lengths on $Ni_{49.5}Ti_{50.5}$. Sample was tested at 25 °C which is 25 °C lower than M_f. A marker is placed to the same location to show possible relaxation. a) Image taken at crack length of 11.4 mm and strain in marker is 5.35 % .b) Image taken at crack length of 15.5 mm and strain in marker is 5.50 %.

7.4.2 Measuring Fracture Toughness of NiTi at Austenitic Range

Force displacement curves for all tests run at 170 °C can be seen in Figure 7.5. Note that austenitic material shows a much sharper peak as opposed to diffused one in

martensitic material. Fracture toughness values calculated by all three approach were shown in Table 7.5.

Table 7.5 Summary of all fracture toughness tests on $Ni_{49.5}Ti_{50.5}$ run at 170 °C. Units of K values are ($MPa\sqrt{m}$) and J values are (kJ/m^2)

Sample Code	Precrack Length (mm)	Thickness (mm)	Fracture Toughness Values				
			LEFM	EPFM (simple)		EPFM (R-Curve)	
			K_I	J_C	K_{JC}	J_{IC}	K_{JIC}
NiTi_ASR_013	9.23	2.42	54.7	126.9	105.6	223.0	140.0
NiTi_ASR_017	9.97	3.21	57.3	139.7	110.8	190.4	129.4

Although austenitic NiTi has much sharper peak, still it doesn't satisfy 95 % secant line criteria for linear elastic fracture mechanics acceptance criteria. Moreover unbroken ligament length criteria states minimum length should be 76.7 mm calculated by equation 3.6 while in our study it is around 10 mm.

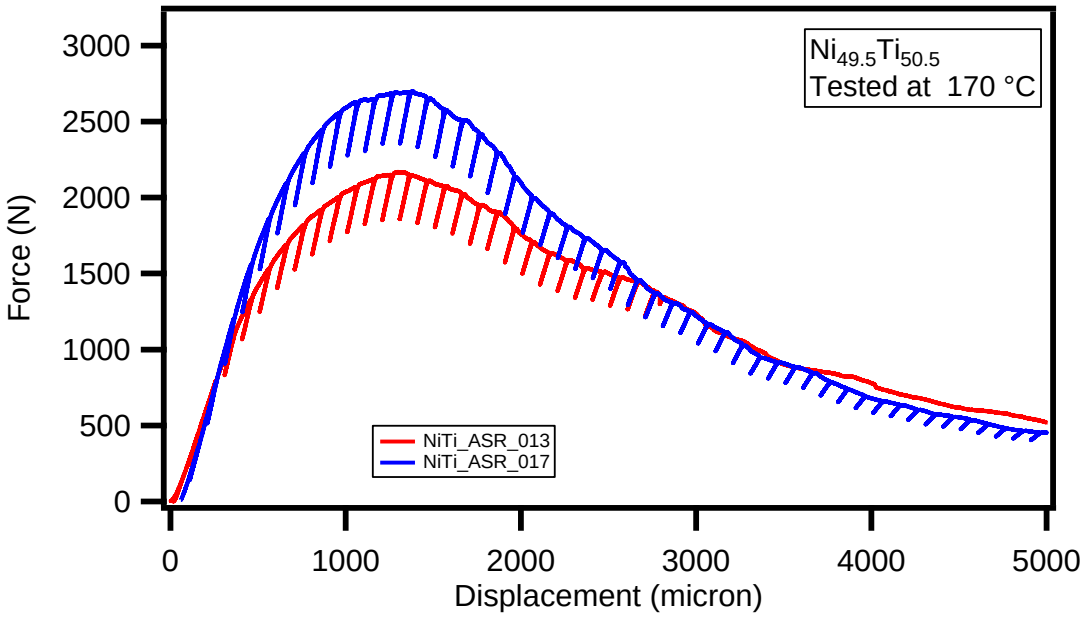

Figure 7.5 Force vs displacement curves for all fracture toughness tests on $Ni_{49.5}Ti_{50.5}$ done at 170 °C.

Unstable crack growth doesn't start before the critical value (0.33 mm) which is given by equation 3.9 for simple method for elasto-plastic fracture mechanics approach. Minimum thickness and unbroken ligament length should be 28.2 mm, where in this study thickness is around 3 mm and unbroken ligament is around 10 mm.

Minimum thickness for R curve method for elasto-plastic fracture mechanic approach was calculated to be 4.38 mm, which is bigger than samples tested in this study.

Strain field around crack tip determined by DIC as can be seen in Figure 7.6. Note that plastic zone also exist in those tests. Even though stress relaxation happens beyond the crack tip, no recovery in strain was observed. This can be associated with lack of super-elasticity on this material.

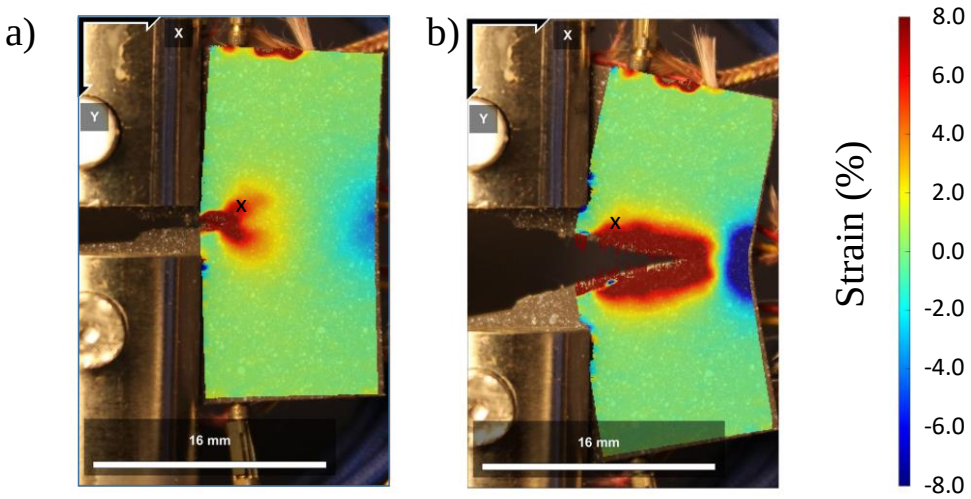

Figure 7.6 Digital image correlation showing strain in y direction for two crack lengths on $Ni_{49.5}Ti_{50.5}$. Sample was tested at 170 °C which is 60 °C higher than A_f. A marker is placed to the same location to show possible relaxation. a) Image taken at crack length of 10.34 mm and strain in marker is 3.22 % .b) Image taken at crack length of 15.03 mm and strain in marker is 3.81 %.

7.4.3 Measuring Fracture Toughness of NiTiHf at Martensitic Range

Force displacement curves of 2 tests run at 100 °C can be seen in Figure 7.7. Because of the lack of stable crack growth, elasto-plastic fracture mechanics approach R curve method is not applicable. Fracture toughness values, calculated by 2 methods (linear elastic and elasto-plastic simple method) can be seen in Table 7.6.

Table 7.6 Summary of all fracture toughness tests on $N_{50.3}Ti_{29.7}Hf_{20}$ run at 100 °C. Units of K values are ($MPa\sqrt{m}$) and J values are (kJ/m^2)

Sample Code	Precrack Length (mm)	Thickness (mm)	Fracture Toughness Values		
			LEFM	EPFM (simple)	
			K_I	J_C	K_{JC}
NiTiHf_ASR_002	10.00	2.42	46.3	42.9	51.5
NiTiHf_ASR_003	10.07	3.21	45.8	47.6	54.2

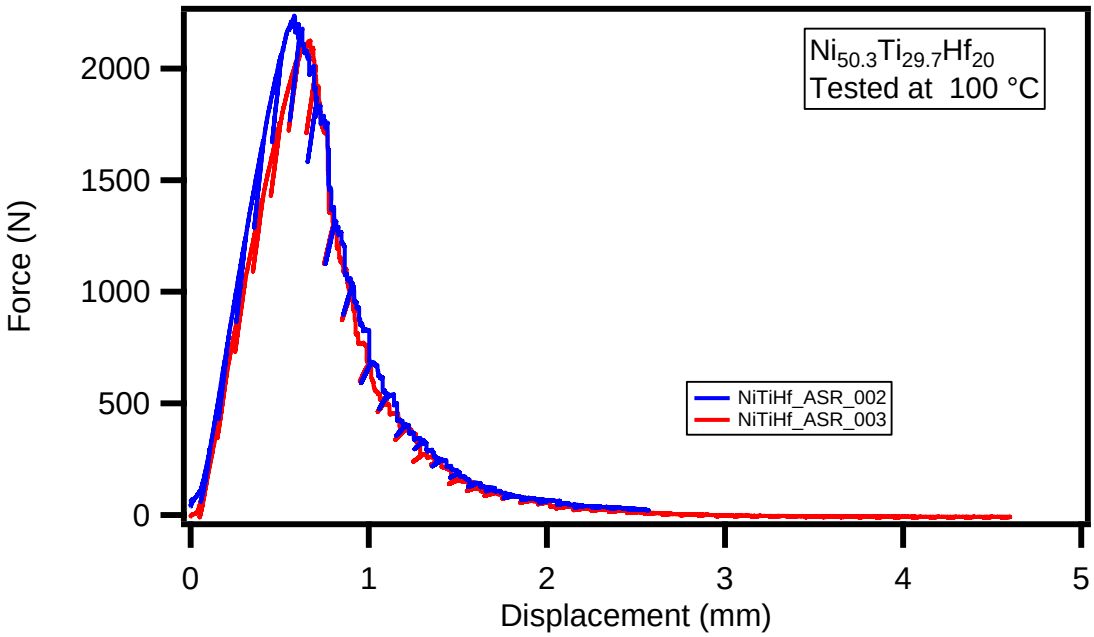

Figure 7.7 Force vs displacement curves for all fracture toughness tests on $Ni_{50.3}Ti_{29.7}Hf_{20}$ done at 100 °C.

Note that maximum force in force displacement curve lays within tangent and 95 % secant line. Minimum length for unbroken ligament was calculated by equation 3.6 to be 26.65 mm. In this study unbroken ligament length was 10 mm. Similarly minimum

thickness and unbroken ligament length for elasto-plastic fracture mechanics simple method calculated to be 5.74 mm where the values of thickness and unbroken ligament for current study was 3.5 mm and 10 mm respectively.

Strain field around crack tip determined by DIC as can be seen in Figure 7.8. Note that plastic zone exists but both it is smaller in size and magnitude of the strain is smaller. That can be explained by due to higher strength and smaller actuation strain of $Ni_{50.3}Ti_{29.7}Hf_{20}$ when compared to $Ni_{49.5}Ti_{50.5}$. In contrast to $Ni_{49.5}Ti_{50.5}$, recovery of strain beyond crack tip due to stress relaxation is observed. The “x” marker is placed to show recovery of strain. In Figure 7.8.a in marked position strain is 1.26 % and when crack grew in Figure 7.8.b strain is 0.58 %. Because material is in martensitic stage that relaxation is due to elastic strain.

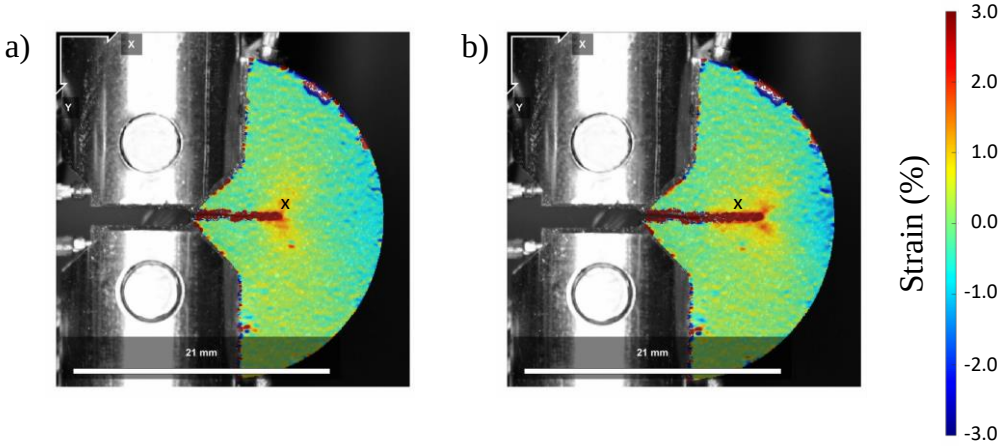

Figure 7.8 Digital image correlation showing strain in y direction for two crack lengths on $Ni_{50.3}Ti_{29.7}Hf_{20}$. Sample was tested at 100 °C which is 15 °C lower than M_f. A marker is placed to the same location to show possible relaxation. a) Image taken at crack length of 10.6 mm and strain in marker is 1.26 % .b) Image taken at crack length of 13.2 mm and strain in marker is 0.58 %.

7.4.4 Measuring Fracture Toughness of NiTiHf at Austenitic Range

Force displacement curves of 3 tests run at 200 °C can be seen in Figure 7.9. Because of the lack of stable crack growth, elasto-plastic fracture mechanics approach R curve method is not applicable. Fracture toughness values, calculated by 2 methods (linear elastic and elasto-plastic simple method) can be seen in Table 7.7.

Table 7.7 Summary of all fracture toughness tests on $N_{50.3}Ti_{29.7}Hf_{20}$ run at 200 °C. Units of K values are ($MPa\sqrt{m}$) and J values are (kJ/m^2)

Sample Code	Precrack Length (mm)	Thickness (mm)	Fracture Toughness Values		
			LEFM	EPFM (simple)	
			K_I	J_C	K_{JC}
NiTiHf_ASR_004	10.00	2.42	50.8	34.2	50.8
NiTiHf_ASR_005	10.07	3.21	59.7	55.5	64.8
NiTiHf_ASR_006	9.38	3.40	58.6	48.3	60.4

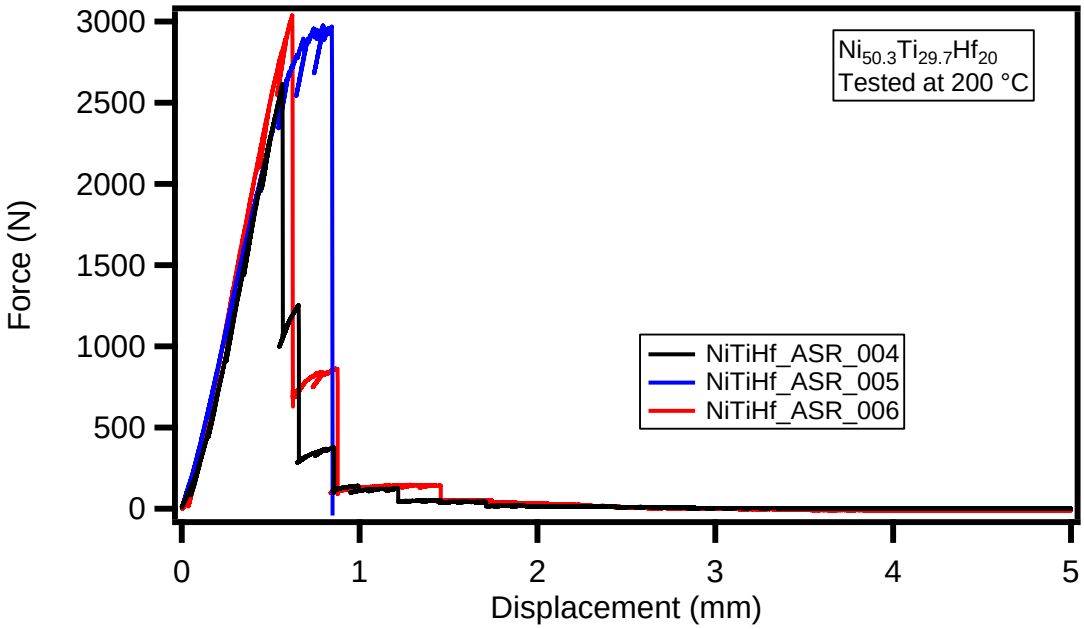

Figure 7.9 Force vs displacement curves for all fracture toughness tests on $Ni_{50.3}Ti_{29.7}Hf_{20}$ done at 200 °C.

Note that maximum force in force displacement curve lays within tangent and 95 % secant line. Minimum length for unbroken ligament was calculated by equation 3.6 to be 38.08 mm. In this study unbroken ligament length was 10 mm. Similarly minimum

thickness and unbroken ligament length for elasto-plastic fracture mechanics simple method calculated to be 5.29 mm where the values of thickness and unbroken ligament for current study was 3.5 mm and 10 mm respectively.

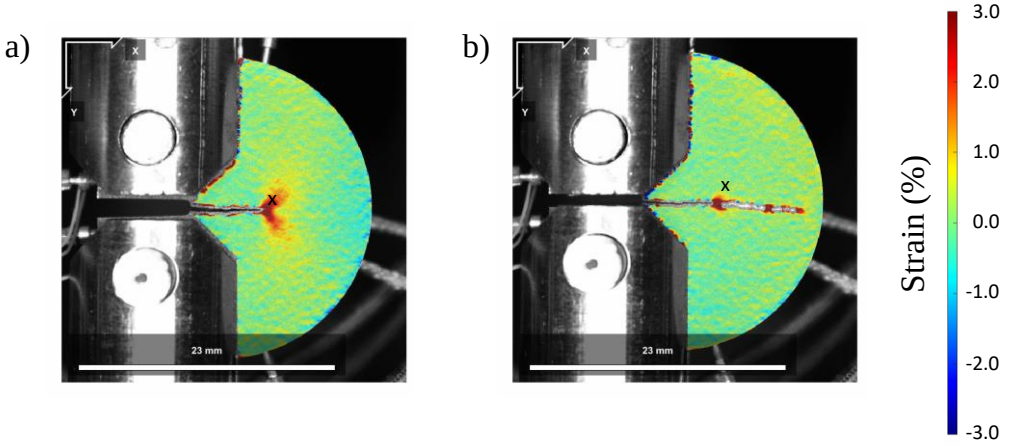

Figure 7.10 Digital image correlation showing strain in y direction for two crack lengths on $Ni_{50.3}Ti_{29.7}Hf_{20}$. Sample was tested at 200 °C which is 15 °C higher than A_f. A marker is placed to the same location to show possible relaxation. a) Image taken at crack length of 10.5 mm and strain in marker is 3.03 %b) Image taken at crack length of 18.4 mm and strain in marker is 0.90 %.

Strain field around crack tip determined by DIC as can be seen in Figure 7.10. Note that plastic zone exists but it is smaller in size and magnitude when compared to $Ni_{49.5}Ti_{50.5}$. That can be explained by due to higher strength and smaller actuation strain of $Ni_{50.3}Ti_{29.7}Hf_{20}$. In contrast to $Ni_{49.5}Ti_{50.5}$, recovery of strain beyond crack tip due to stress relaxation is more clearly observed. The “x” marker is placed to show recovery of

strain. In Figure 7.10.a in marked position strain is 3.03 % and when crack grew in Figure 7.10.b strain is 0.90 %.

7.5 Discussions and Conclusions

Three fracture toughness measurement methods were studied in this work. It is found that both minimum thickness and 95 % secant line criteria were not satisfied for LEFM approach for samples with dimensions in tested range. In $Ni_{49.5}Ti_{50.5}$ there is stable crack growth beyond the limit specified for simple J integral method (EPFM). On the other hand $Ni_{50.3}Ti_{29.7}Hf_{20}$ didn't show stable crack growth thus simple method can be applied in accordance with ASTM E1820 given that thickness criteria is also satisfied. Among all three methods R-curve method required the smallest size. For $Ni_{49.5}Ti_{50.5}$, all the requirements of R-curve method has been satisfied for samples thicker than 2.97 and 2.58 mm for martensite and austenite respectively.

The effect of thickness is studied in $Ni_{49.5}Ti_{50.5}$ at room temperature. Threshold of applicability for R-curve method is around 3 mm, samples were tested with thicknesses from 1 to 3.5 mm. The thinnest samples (1.5 and 1 mm) were failed to provide data for R-curve method. The data suggests there is no sharp change of fracture toughness values with varying thickness as in the case of plane strain-plane stress transition. When LEFM approach is considered the critical thickness for that transition is already quite high (152 and 90 mm for martensite and austenite respectively). The lack of change could be explained by that fact. Moreover it must me noted that the range considered is rather

limited. It only can be concluded that no significant change has been observed in studied range.

It was observed that LEFM give the smallest scattering in the data. The fracture toughness is measured to be 39.4 ± 2.7 MPa$\sqrt{m}$ where those obtained by simple and R-curve EPFM fracture toughness values are 92.0 ± 9.8 and 99.6 ± 10.9 MPa$\sqrt{m}$ respectively. Note that the scattering which obtained by calculating standard deviation, is higher in EPFM approaches but it also must be considered that because those values have plastic component they are considerably higher. If the percentage of the scattering to average is considered it can be observed that LEFM yields to 6.85% variation where simple and R-curve EPFM approaches yield to 10.65 and 10.94 % variations respectively. The increase could be associated with the fact that the EPFM approach requires precise displacement measurement and in this study cross-head displacement is used instead of extensometer.

When effect of phase constitution or temperature is considered, it can be noted that there is a strong difference between LEFM and EPFM approaches. If LEFM approach is considered for $Ni_{49.5}Ti_{50.5}$ it is 39.4 MPa$\sqrt{m}$ for room temperature (100 % martensite) case and 56.0 MPa$\sqrt{m}$ for 170 °C (100 % austenite) case. In this comparison it can be said that austenite has significantly higher fracture toughness and it is consistent with reports on literature. On the other hand when R-curve approach is considered, martensitic state shows 99.6 MPa$\sqrt{m}$ where austenitic state shows 134.7 MPa$\sqrt{m}$. The two of the phases has much closer fracture toughness values. When $Ni_{50.3}Ti_{29.7}Hf_{20}$ is considered LEFM shows 46.1 MPa$\sqrt{m}$ at martensitic stage and 56.4 MPa$\sqrt{m}$ at austenitic stage. On the other hand,

when EPFM considered (simple method) fracture toughness values are found to be 52.8 and 58.7 $MPa\sqrt{m}$ for martensite and austenite respectively. It was hypothesized that because there is always martensite at the crack tip fracture toughness of martensite and austenite should be the same. In $Ni_{49.5}Ti_{50.5}$ because material doesn't show superelasticity those values are not expected to be same and they are different and austenite is higher. In $Ni_{50.3}Ti_{29.7}Hf_{20}$ values are much closer and could be considered same. More tests must be done to validate this hypothesis.

Lastly fracture toughness values of $Ni_{49.5}Ti_{50.5}$ and $Ni_{50.3}Ti_{29.7}Hf_{20}$ can also be compared. If values of fracture toughness obtained by LEFM approach are considered $Ni_{50.3}Ti_{29.7}Hf_{20}$ has higher fracture toughness at martensitic stage, and two materials have the same fracture toughness at austenitic stage. On the other hand when EPFM approach is considered, $Ni_{50.3}Ti_{29.7}Hf_{20}$ has significantly lower fracture toughness values on both martensite and austenite. It is consistent with the observations of higher strength and lower ductility of $Ni_{50.3}Ti_{29.7}Hf_{20}$.

8. ACTUATION CRACK GROWTH OF SHAPE MEMORY ALLOYS

8.1 Introduction

Damage tolerant fatigue approach is a method where an intentionally formed crack is subjected to cyclic loading and crack growth rates are determined as function of controlled variables such as force levels, rate and ratio of higher and lower bound of cyclic force. This methods make it possible to asses remaining fatigue life of a component with an existing crack given that the force profile is known. This method was widely used for structural engineering materials with cycling the force. Because shape memory alloys (SMAs) show significant shape change with thermal cycling under stress and that route is representative of service condition of a solid state actuator with SMA active elements, it is proposed to measure crack growth under thermo-mechanical route and use obtained values to predict remaining fatigue life of components with crack or design against catastrophic failures.

Actuation crack growth is defined as extension of a crack under thermal cycling and under constant force in this study. Crack growth rates were quantitatively determined by methods analogous to mechanical crack growth experiments described in ASTM standard E647 and summarized in section 3.2.6 of this dissertation. Actuation fatigue was studied in life based approach but to the best of author's knowledge this is the first work where damage tolerant approach for thermo-mechanical fatigue of SMAs studied in a

systematical manner. Aim of this study is to develop methods of crack growth rate measurements and provide initial data.

8.2 Experimental Procedure

Ni lean NiTi ($Ni_{49.5}Ti_{50.5}$), details of which described in section 3.1.3, was used in this study. Actuation crack growth experiments were done in setup described in section 3.2.6.2. Samples used in this study were rectangular compact tension samples with thickness 3 mm, width 25 mm and length 24 mm.

Precracks were introduced with mechanical cycling. The stress intensity factor amplitude for crack growth was chosen to be 9 $MPa\sqrt{m}$ with R=0.1, which means the lowest and highest stress intensity factors are 1 and 10 $MPa\sqrt{m}$ respectively. Total length of initial crack length including notch was chosen to be 6 mm. Upper and lower cycle temperatures were chosen to be 35 °C (M_f-10) and 170 °C (A_f+60) respectively. Note that upper cycle temperature is chosen to be higher to ensure complete transformation, since transformation temperatures increases with applied stress in accordance with Clausius-Clapeyron law.

Initial stress intensity factors were chosen to be 5, 10, 15 and 30 $MPa\sqrt{m}$. Samples were heated up to upper cycle temperature under no load. Force required to create given stress intensity factors were applied to the sample and kept constant throughout the test. Temperature of the sample was measured by six spot welded thermocouples. Details of temperature control and locations of the thermo-couples can be seen in section 3.2.6.2.

8.3 Results

8.3.1 Determination of Actuation Crack Growth Rate

Four stress intensity factors were tested on $N_{49.5}Ti_{50.5}$. Number of cycles to failure, average crack growth rate can be seen in Table 8.1. Note that when stress intensity factor is 30 MPa$\sqrt{m}$ sample (NiTi_ASR_014) broke during first cooling. Crack length as a function of temperature for this test can be seen in Figure 8.1.a. It was observed that crack doesn't grow until a specific temperature was reached. That temperature can be called as onset of crack opening and will be symbolized with CO_s. After that crack grew unstably and sample failed. On other force levels, stable crack growth and multiple cycles before failure were observed.

Table 8.1 List of all tested samples including experimental details such as initial stress intensity factor, number of cycles to failure and average crack growth rate. Sample codes were reported which are unique values to identify each sample as will be referred for the rest of the study.

Sample code	Initial Stress Intensity Factor , K (MPa$\sqrt{m}$)	Number of cycles to failure	Average Crack Growth Rate (mm/cycle)
NiTi_ASR_014	30	<1	NA
NiTi_ASR_016	15	7	0.84
NiTi_ASR_031	15	6	1.13
NiTi_ASR_015	10	21	0.34
NiTi_ASR_030	10	18	0.39
NiTi_ASR_025	5	341	0.022
NiTi_ASR_027	5	264	0.029

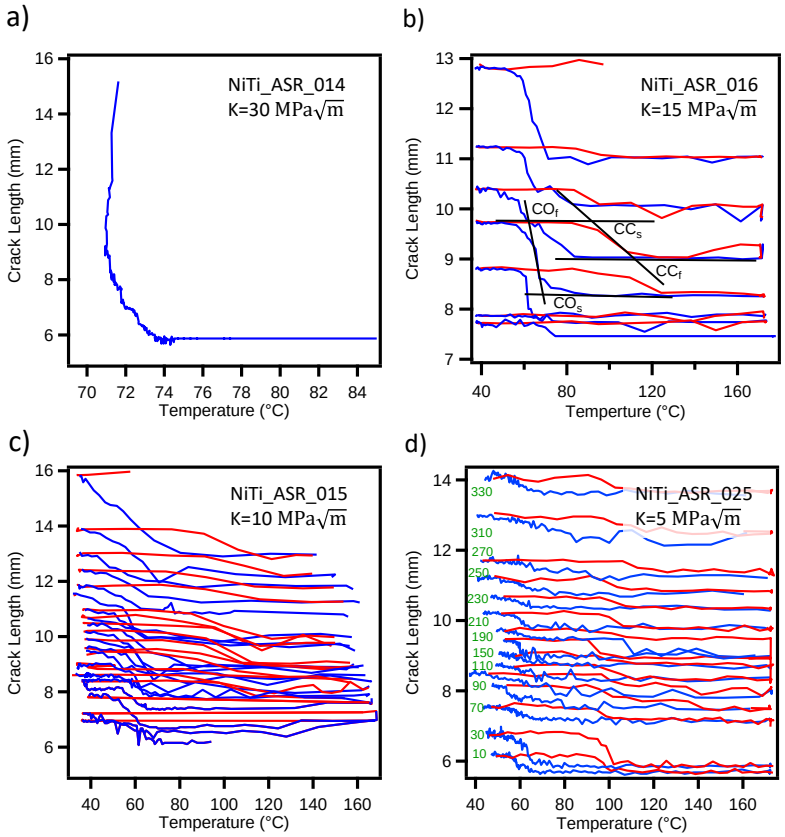

Figure 8.1 Crack length as a function of temperature during thermal cycling for 4 tests with different initial stress intensity factors; a) for sample coded NiTi_ASR_014 where initial stress intensity factor has chosen to be 30 MPa$\sqrt{m}$, sample failed during first cooling, b) for sample coded NiTi_ASR_016 where initial stress intensity factor chosen to be 15 MPa$\sqrt{m}$, sample failed in 7th cycle during heating c) for sample coded NiTi_ASR_015 where initial stress intensity factor chosen to be 10 MPa$\sqrt{m}$ sample failed during heating 21st cycle during heating d) for sample coded NiTi_ASR_025 where initial stress factor chosen to be 5 MPa$\sqrt{m}$ for the sake of clarity only selected cycles were shown.

The samples NiTi_ASR_016 and NiTi_ASR_31 tested with initial stress intensity factor of 15 MPa$\sqrt{m}$ lasted 7 and 6 cycles respectively. Crack length as a function of temperature can be seen in Figure 8.1.b, where heating cycles were red and cooling cycles

were blue. Since number of cycles were limited whole test was plot in the figure. Similar to previous test, crack didn't grow before CO_s. Once the critical temperature is reached crack extends to a length and below another critical temperature crack growth stops. The temperature where crack growth ends is named as crack opening finish and symbolized as CO_f. It is observed that during heating because of phase transformation crack mouth closes and as a result, two lips of the crack touches at the crack tip. The crack is not healed but because crack length is measured by optical and potential drop methods it is not possible to measure the exact crack length during heating. This phenomena will be called crack closure and the onset of temperature when it happens will be noted as CC_s. As it happened with crack opening crack closure also stops after a critical temperature which will be called CC_f. Those critical values reported are calculated by tangent intersection method similar to DSC and iso-baric heating cooling tests and method is demonstrated in Figure 8.1.b. Since multiple cycles were observed it was also possible to plot crack length as a function of cycle numbers. The crack length vs number of cycle plots can be seen in Figure 8.2. Other than increased crack growth rate at the last cycle, crack growth can be fit to a linear function.

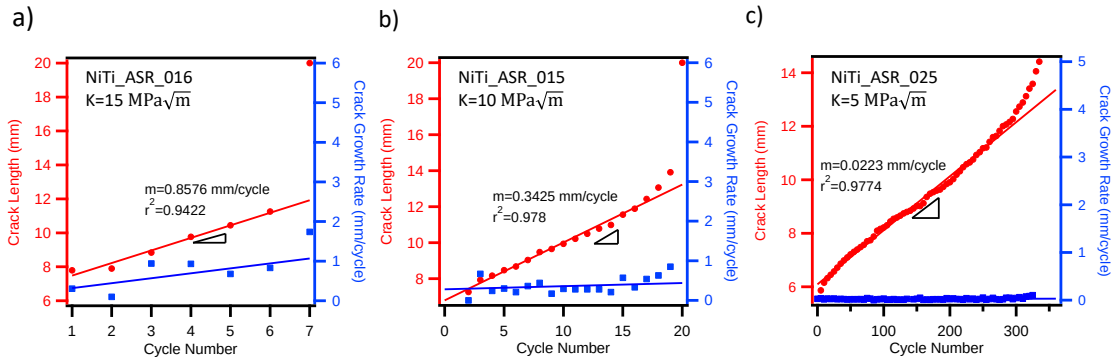

Figure 8.2 Plot of crack growth and rate of it as a function of number of cycles for samples that showed multiple cycles. a) Sample coded NiTi_ASR_016 with initial stress intensity factor of 15 MPa$\sqrt{m}$. b) Sample coded NiTi_ASR_015 with initial stress intensity factor of 10 MPa$\sqrt{m}$. c) Sample coded NiTi_ASR_025 with initial stress intensity factor of 5 MPa$\sqrt{m}$.

The samples NiTi_ASR_15 and NiTi_ASR_30 tested at 10 MPa$\sqrt{m}$ initial stress intensity factor cycled 21 and 18 times before failure respectively. Crack length as a function of temperature was plotted in Figure 8.1.c. The same observations hold in this tests as well where crack starts and stops growing at specific temperatures during cooling and closes during heating. Crack length at lower cycle temperature as function of number of cycles can be seen in Figure 8.2.b.

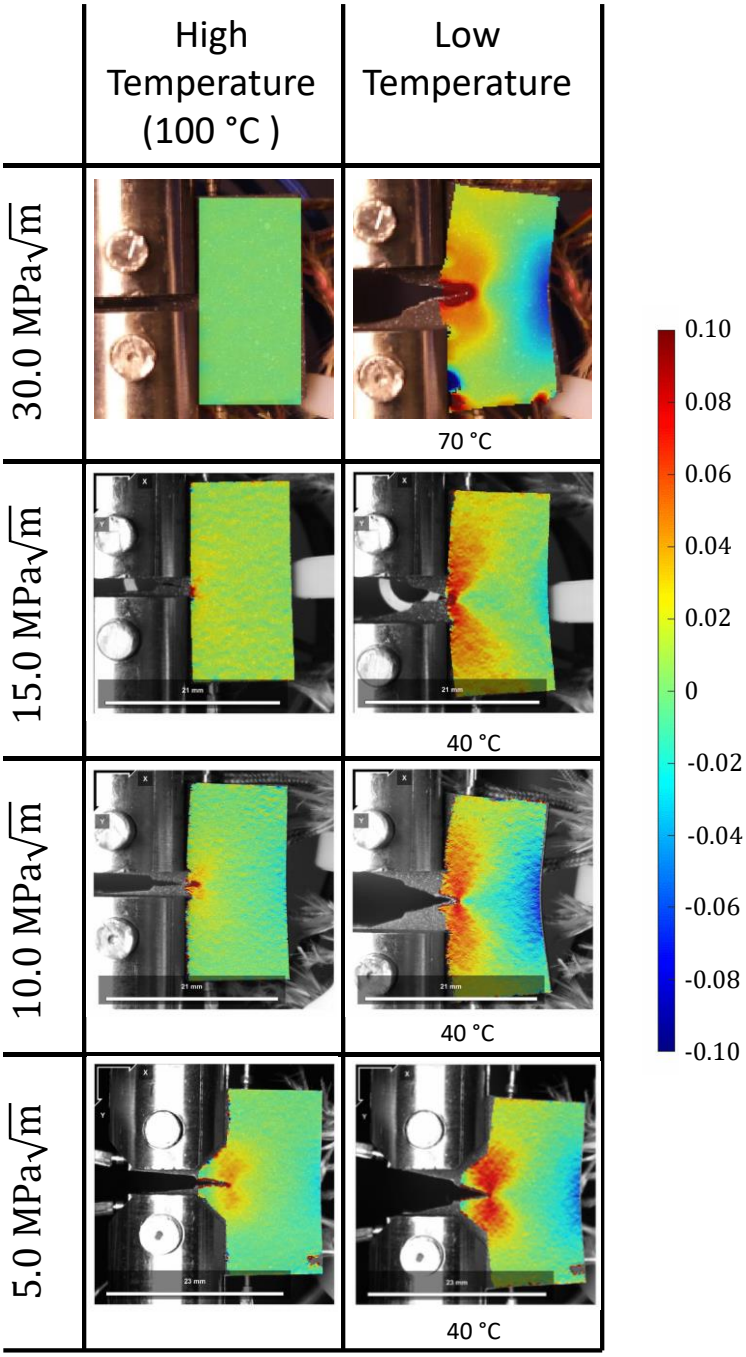

Figure 8.3 Digital image correlation (DIC) of NiTi CT samples during thermal cycling. Two dimensional strain maps are overlaid. The strain shown in the figure is the strain in vertical (y) direction (ε_{yy})

The samples NiTi_ASR_25 and NiTi_ASR_27 tested at 5 $MPa\sqrt{m}$ initial stress intensity factor cycled 341 and 264 times before failure. Similar to previous test for the sake of clearance a subset of cycles (every 10^{th}) were plotted in Figure 8.1.d for sample coded NiTi_ASR_025 and crack length versus number of cycles plot can be seen in Figure 8.2.c.

Digital image correlation (DIC) was used to determine 2 dimensional (2D) strain fields during thermal cycling. Images for upper and lower cycle temperatures for all tests can be seen in Figure 8.3. Note that because 15 $MPa\sqrt{m}$ initial stress intensity factor test sample failed during first cooling instead of 35 °C, DIC image before failure is used in the figure which corresponds to around 70 °C. Significant amount of strain is generated in front of crack tip due to stress concentration and its morphology coincides with regular plasticity strain field. As crack continues to grow regions behind the crack tip becomes stress free points. Yet it can be noted that plastic deformation behind the crack tip (between crack tip and load line) stays. It can be attributed to lack of super elasticity on tested material. Also note that there is a compressive strain region on the far end of unbroken ligament. This phenomena also coincides with fracture of elastoplastic materials in CT geometry.

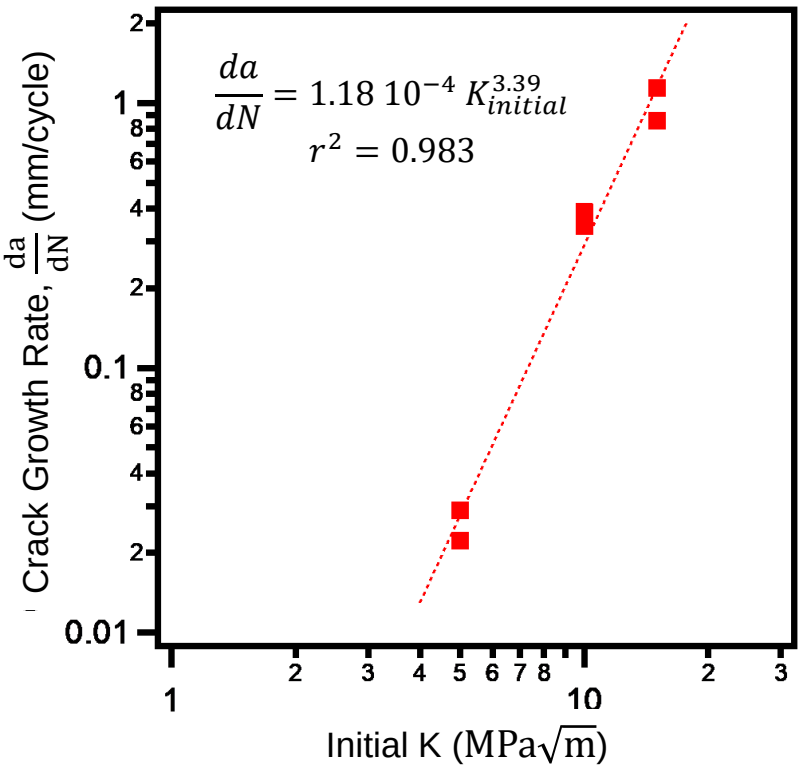

Figure 8.4 Effect of initial stress intensity factor on crack growth rates. Similar to Paris law, increasing stress intensity factor increases crack growth rate. Moreover, the data obtained fits to a power function analogous to Paris law with parameters given.

As expected crack growth rates increases with stress intensity factor. The results tabulated in Table 8.1 can be plot in initial stress intensity factor versus crack growth rate plots analogous to Paris law for mechanical fatigue crack growth. Note that in Paris' law amplitude of stress intensity factors were used as variable or driving force for crack growth. In actuation fatigue crack growth, based on linear elastic fracture mechanics (LEFM) stress intensity factor changes slightly due to crack growth but do not cycle as in

the case of mechanical fatigue crack growth. Thus ΔK can be considered 0. On the other hand, if initial K is used as driving force a trend line can be drawn as shown in Figure 8.4.

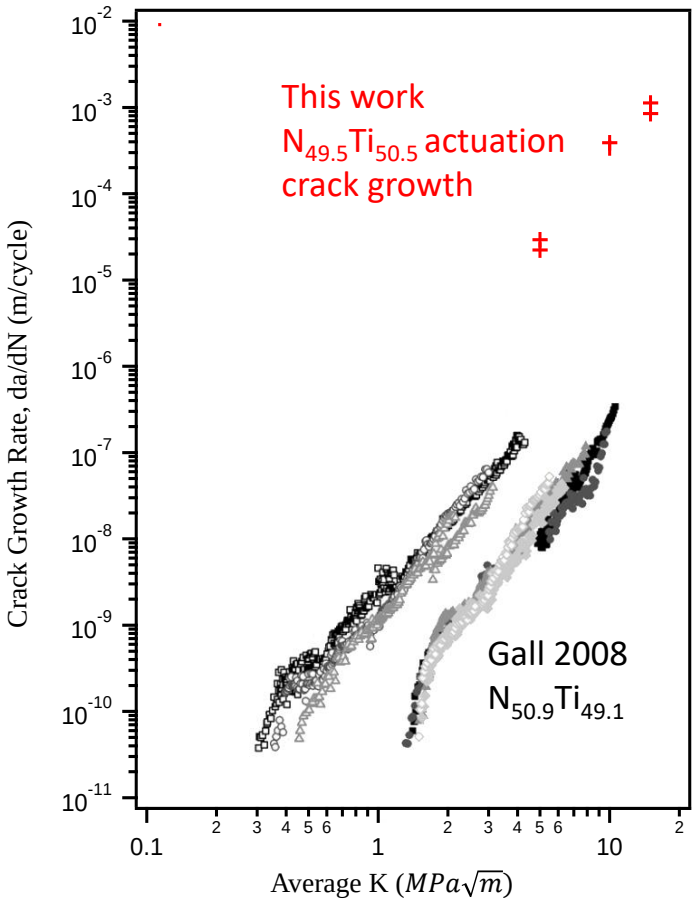

Figure 8.5 Comparison of crack growth rates from mechanical and actuation crack growth. Red data point are from actuation crack growth obtained in this work, black data points are obtained from Gall [46] open markers are for cold rolled and solid markers are for hot rolled with followed by a range of annealing treatments.

In order to compare crack growth rates during actuation and mechanical fatigue, results from mechanical crack growth on literature and measured results were drawn in the same plots in Figure 8.5. The comparison metrics were chosen to be average stress intensity factor (LEFM).

8.3.2 Post Mortem Investigation

Pictures and micrographs were obtained after failure to document deformation and identify features in fracture surface. Pictures of broken samples can be seen in Figure 8.6. It can be seen that samples are significantly deformed and the amount of deformation increases with decreasing initial stress intensity factor or with increasing number of cycles.

Micrographs of fracture surface can be seen in Figure 8.7. Note that overall fracture surface shows quasi cleavage features. End of crack growth after each cycle was marked with blue vertical lines starting with fatigue precrack. Higher magnification images showed that there were crack branching after each cycle.

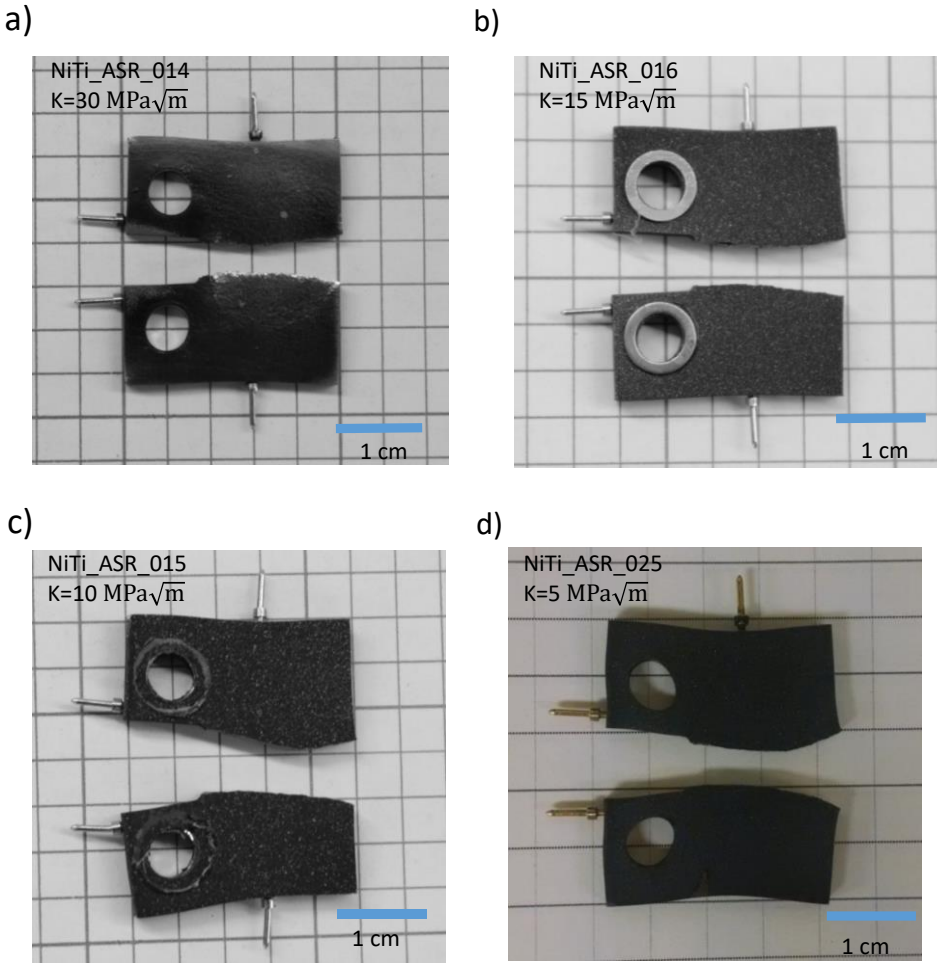

Figure 8.6 Pictures of failed samples tested by actuation crack growth experiments a) Sample coded NiTi_ASR_014, b) sample coded NiTi_ASR_016 c) sample coded NiTi_ASR_015 and d) sample coded NiTi_ASR_025

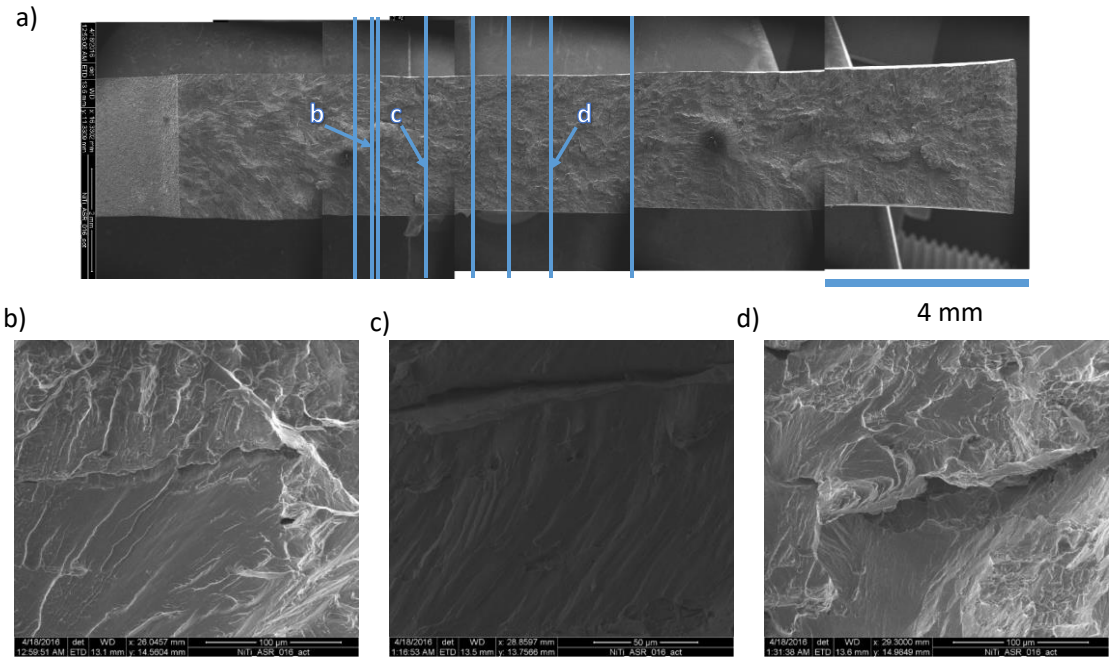

Figure 8.7 Scanning electron microscopy images of fracture surface on sample coded NiTi_ASR_016. a) Construction of low magnification images to show whole fracture surface. Location of higher magnification images and end of crack growth for each cycle are also marked. b), c) and d) higher magnification imaged taken at the points of end of crack growth showing crack branching

8.4 Discussion and Conclusion

Actuation crack growth was studied for the first time to the best of author's knowledge. It was found that in the presence of constant force and thermal cycling crack mouth opens during cooling and closes during heating. Also during cooling crack length increases. The crack length versus temperature plot which is shown in Figure 8.1. resembles to isobaric heating cooling tests. The critical temperatures are likely function of martensitic transformation temperatures. The fact that those temperatures increases with increasing stress intensity factors further supports the hypothesis. Because of the selected

test procedure, stress intensity factor increases with number of cycles or growth of the crack. Note that during heating crack apparently closes, the crack doesn't heal but because crack lengths are measured by optical and potential drop methods when two lips of crack touch to each other it is not possible to distinguish touching surfaces of a crack and continuous material. The growth of crack during cooling has been predicted by finite element analysis (FEA) by Jape [86,87]. According to simulations during cooling strain energy release rate at the crack tip increases due to global phase transformation. That increase saturates when material completely transformed.

The effect of initial stress intensity factor on crack growth rate was shown in Table 8.1 and Figure 8.4. As stress intensity factor increases crack growth rates increases and the correlation between them were expected to be a power function analogous to Paris Law. Note that because force is not cycled, there is no stress intensity range (ΔK) the initial stress intensity factor was used in Figure 8.4. This approach is more in accordance with modified Paris Law reported in section 2.2.2 and equation 2.13. ΔK could be set to 0 and K_{max} could be used as initial. When crack growth rates are compared to the ones obtained by mechanical cycling, it is observed that there is a significant difference. It appears that crack growth rates are 4 orders of magnitude higher during actuation than mechanical fatigue crack growth.

However it must be noted that, LEFM (stress intensity factor values) might not be the best metric to compare. An alternative to that could be EPFM but currently there is no standardized way of calculation J integral values during thermal cycling.

Lastly it was observed in post mortem investigation that after each cycle there forms side cracks or main crack branches through the material. This could be happening during heating. It is known that during heating main crack mouth closes and material actually does work against external forces. During this action there could be favorable stress state for a side crack. After heating section ends and cooling section starts, main branch becomes favorable again and side crack got arrested. It is also analogous to river mark patterns in mechanical crack growth.

9. MAIN CONCLUSIONS AND FUTURE DIRECTIONS

Shape memory alloys are promising candidates for solid state actuators. But it is crucial to determine fatigue performance precisely. Both fatigue life prediction methods namely life based and damage tolerant approaches, are studied in this work. It is aimed to comprehensively characterize fatigue performance and moreover develop methods and techniques to form basis for future data generation.

In this study 3 compositions were studied, Ni-rich NiTi ($Ni_{50.7}Ti_{49.3}$), Ti-rich NiTi ($Ni_{49.5}Ti_{50.5}$) and ternary NiTiHf ($Ni_{50.3}Ti_{29.7}Hf_{20}$). It is found that, NiTiHf has better fatigue performance when life based approach is considered. Also effect of surface condition was studied and found that it has a significant effect. Moreover, fracture toughness was also measured and available methods and their applicability were investigated. Lastly, damage tolerant fatigue approach was studied for $Ni_{49.5}Ti_{50.5}$ with methods derived from classical mechanical fatigue crack growth but in thermo-mechanical route.

Based on the results of the present study the following conclusions can be made:

1. Surface condition has a strong effect on fatigue performance of shape memory alloys as found in $Ni_{50.7}Ti_{49.3}$ and $Ni_{50.3}Ti_{29.7}Hf_{20}$. It is found that EDM recast layer, increases fatigue life considerably when actuation strain is below a threshold. Above the threshold, recast layer has detrimental effect on fatigue performance likely due to premature cracking of the strong and brittle outer layer.

Microstructure also has an effect on fatigue performance. Cases with higher ductility showed better fatigue performances.

2. Two-way shape memory effect and stability of it in $Ni_{50.3}Ti_{29.7}Hf_{20}$ under shear loading has been studied. It is found that $Ni_{50.3}Ti_{29.7}Hf_{20}$ develops TWSME within 600 cycles and gains dimensional stability faster than binary NiTi compositions. Stability of developed TWSME has also been studied and found that it is stable up to 400 C. It is also found via TEM that austenite has been stabilized as a result of thermo-mechanical training.
3. Fracture toughness of $Ni_{49.5}Ti_{50.5}$ and $Ni_{50.3}Ti_{29.7}Hf_{20}$ has been studied at martensitic and austenitic temperature ranges. It is found that LEFM approach requires prohibitively large sample sizes. On the other hand EPFM approach requires much more attainable sample sizes. Changing approach to measure fracture toughness also impacts comparison of fracture toughness of martensite and austenite as well as $Ni_{49.5}Ti_{50.5}$ and $Ni_{50.3}Ti_{29.7}Hf_{20}$. Using EPFM reduces the gap between austenite and martensite considerably suggesting material may have a single fracture toughness value since there is always martensite at the crack tip due to stress concentration. The ranking of fracture toughness of $Ni_{49.5}Ti_{50.5}$ and $Ni_{50.3}Ti_{29.7}Hf_{20}$ also reverses as LEFM and EPFM compared. In LEFM $Ni_{50.3}Ti_{29.7}Hf_{20}$ has slightly higher fracture toughness where EPFM shows $Ni_{49.5}Ti_{50.5}$ to have significantly higher fracture toughness.
4. Crack growth during actuation has been studied for the first time. The method for testing has been developed in house, and initial finding has been reported. It is

found that crack grows during cooling as also was predicted by FEA. Measured crack growth rates found to be significantly higher than mechanical crack growth rates when LEFM metric is used to compare but it is likely not a proper comparison. More work should be done to refine the method and develop better metrics for quantifying fatigue performance before accurate comparisons can be made.

It is aimed in this work to comprehensively study fatigue performance of shape memory alloys. The methods outlined can be used to quantify fatigue life and crack growth rates making it possible to use both life based and damage tolerant design approaches against fatigue.

Although initial data has been provided for comparison and resolving effect of various factors, more data should be generated to strengthen the conclusions presented in this work. Moreover only 3 compositions and several microstructure has been studied in this work and only 2 material composition is studied in each section (fatigue, fracture toughness). Other compositions and microstructures can be studied and effect of various factors such as microstructure, loading or thermal cycling rate, effect of sample geometry can be revealed.

Lastly, to compare actuation crack growth performance to mechanical, better metrics should be developed which can take global phase transformation into account.

REFERENCES

[1] F.C. Campbell, Elements of Metallurgy and Engineering Alloys, ASM International, 2008.

[2] S. Hirose, K. Ikuta, Y. Umetani, Adv. Robot. 3 (1988) 3–16.

[3] R. Noebe, T. Biles, S. Padula, in:, T.S.S. Winston O. Soboyejo (Ed.), Adv. Struct. Mater. Des. Optim. Appl., CRC Press, 2006, pp. 145–186.

[4] J. Van Humbeeck, Adv. Eng. Mater. (2001) 837–850.

[5] K. Yamauchi, I. Ohkata, K. Tsuchiya, S. Miyazaki, Shape Memory and Superelastic Alloys: Applications and Technologies, Elsevier Science, 2011.

[6] L. Portlock, L. Schetky, B. Steinetz, Aiaa 1995 3326 (1995) 346–354.

[7] L.M. Schetky, Mater. Sci. Forum 327–328 (2000) 9–16.

[8] J.H. Mabe, R.T. Ruggeri, E. Rosenzweig, C.-J.M. Yu, in:, Smart Struct. Mater., 2004, pp. 95–109.

[9] P. Barooah, N. Rey, Proc. SPIE - Int. Soc. Opt. Eng. 4693 (2002) 384–395.

[10] J. Mabe, F. Calkins, G. Butler, 47th AIAA/ASME/ASCE/AHS/ASC Struct. Struct. Dyn. Mater. Conf. 14th AIAA/ASME/AHS Adapt. Struct. Conf. 7th (2006) 1–19.

[11] K. Yamauchi, I. Ohkata, K. Tsuchiya, S. Miyazaki, Shape Memory and Superelastic Alloys: Applications and Technologies, Elsevier Science, 2011.

[12] D.C. Lagoudas, Shape Memory Alloys: Modeling and Engineering Applications, Springer US, 2008.

[13] T Tadaki, K Otsuka, and K Shimizu, Annu. Rev. Mater. Sci. 18 (1988) 25–45.

[14] P. Chowdhury, H. Sehitoglu, in:, Prog. Mater. Sci., Elsevier Ltd, 2017, pp. 49–88.

[15] ASTM, Stand. Des. F2005-05 5 (2005).

[16] A. Ölander, Zeitschrift Fur Krist. 83 (1932) 145–148.

[17] L.C. Chang, T.A. Read, Trans. Am. Inst. Min. Metall. Eng. 191 (1951) 47–52.

[18] D.S. Lieberman, M.S. Wechsler, T.A. Read, 473 (1955).

[19] W.J. Buehler, J. V Gilfrich, R.C. Wiley, J. Appl. Phys. 34 (1963) 1475–1477.

[20] S. Gollerthan, Untersuchungen Zum Bruchverhalten von NiTi-Formgedaechtnislegierungen, Ruhr University Bochum, 2008.

[21] T. Tadaki, Y. Nakata, K. Shimizu, K. Otsuka, Trans. JIM 27 (1986) 731–740.

[22] M. Nishida, C.M. Wayman, Mater. Sci. Eng. 93 (1987) 191–203.

[23] W. Tirry, D. Schryvers, K. Jorissen, D. Lamoen, Acta Crystallogr. Sect. B Struct. Sci. 62 (2006) 966–971.

[24] M. Nishida, C.M. Wayman, T. Honma, Metall. Trans. A 17 (1986) 1505–1515.

[25] W. Tang, B. Sundman, R. Sandström, C. Qiu, Acta Mater. 47 (1999) 3457–3468.

[26] E.Y. Panchenko, Y.I. Chumlyakov, I. V. Kireeva, A. V. Ovsyannikov, H. Sehitoglu, I. Karaman, Y.H.J. Maier, Phys. Met. Metallogr. 106 (2008) 577–589.

[27] A. Evirgen, F. Basner, I. Karaman, R.D. Noebe, J. Pons, R. Santamarta, Funct. Mater. Lett. 5 (2012) 1250038.

[28] K. Otsuka, X. Ren, Prog. Mater. Sci. 50 (2005) 511–678.

[29] J. Ma, I. Karaman, R.D. Noebe, Int. Mater. Rev. 55 (2010) 257–315.

[30] O.L. Semenova, L.O. Tret'yachenko, V.M. Petyukh, Powder Metall. Met. Ceram. 46 (2007) 556–564.

[31] E.L. Semenova, Powder Metall. Met. Ceram. 40 (2001) 414–425.

[32] R. Santamarta, R. Arróyave, J. Pons, A. Evirgen, I. Karaman, H.E.E. Karaca, R.D.D. Noebe, Acta Mater. 61 (2013) 6191–6206.

[33] B.C. Hornbuckle, Investigations in Phase Stability And Mechanical Attributes in Nickel-Rich Nitinol With And Without Hafnium Additions, University of Alabama, 2014.

[34] F. Yang, D.R. Coughlin, P.J. Phillips, L. Yang, A. Devaraj, L. Kovarik, R.D. Noebe, M.J. Mills, Acta Mater. 61 (2013) 3335–3346.

[35] B. Kockar, I. Karaman, J.I. Kim, Y. Chumlyakov, Scr. Mater. 54 (2006) 2203–2208.

[36] X.L. Meng, Y.F. Zheng, Z. Wang, L.C. Zhao, Mater. Lett. 45 (2000) 128–132.

[37] S. Suresh, Fatigue of Materials. 2nd Ed. S. Suresh., Cambridge ; New York : Cambridge University Press, 1998., 1998.

[38] E. Castillo, A. Fernández-Canteli, A Unified Statistical Methodology for Modeling Fatigue Damage, 2009.

[39] ASTM, Stand. Des. E468-11 (2011).

[40] ASTM, Stand. Des. E606/E606M-12 (2012).

[41] R.G. Forman, Study of Fatigue Crack Initiation from Flaws Using Fracture Mechanics Theory, 1968.

[42] D. Broek, J. Schijve, Aircr. Eng. Aerosp. Technol. 39 (1967) 10–18.

[43] R.O. Ritchie, Compr. Struct. Integr. 4 (2003) 359–388.

[44] A. Ohta, N. Suzuki, T. Mawari, Int. J. Fatigue 14 (1992) 224–226.

[45] K.N. Melton, O. Mercier, Acta Metall. 27 (1979) 137–144.

[46] K. Gall, J. Tyber, G. Wilkesanders, S.W. Robertson, R.O. Ritchie, H.J. Maier, Mater. Sci. Eng. A 486 (2008) 389–403.

[47] K.N. Melton, O. Mercier, Mater. Sci. Eng. 40 (1979) 81–87.

[48] Z. Moumni, A. Van Herpen, P. Riberty, Smart Mater. Struct. 14 (2005) S287–S292.

[49] C. Maletta, E. Sgambitterra, F. Furgiuele, R. Casati, A. Tuissi, Smart Mater. Struct. 21 (2012) 112001.

[50] A. Runciman, D. Xu, A.R. Pelton, R.O. Ritchie, Biomaterials 32 (2011) 4987–4993.

[51] S. Miyazaki, K. Mizukoshi, T. Ueki, T. Sakuma, Y. Liu, Mater. Sci. Eng. A 273–275 (1999) 658–663.

[52] M. Wagner, T. Sawaguchi, G. Kausträter, D. Höffken, G. Eggeler, Mater. Sci. Eng. A 378 (2004) 105–109.

[53] Y. Zhang, J. Zhu, Z. Moumni, A. Van Herpen, W. Zhang, Smart Mater. Struct. 25 (2016) 35042.

[54] F. Casciati, S. Casciati, L. Faravelli, Proc. Est. Acad. Sci. – Phys. Math. 56 (2007) 207–217.

[55] C.R. Clark, D.P. Marcelli, in:, Proc. SPIE, 1999, pp. 311–320.

[56] L. Brown, Metall. Mater. Trans. A 13 (1982) 25–31.

[57] L. Delaey, J. Janssen, D. Van de Mosselaer, G. Dullenkopf, A. Deruyttere, Scr. Metall. 12 (1978) 373–376.

[58] N. Morgan, A. Wick, J. DiCello, R. Graham, in:, Proc. Int. Conf. Shape Mem. Superelastic Technol., 2006, pp. 821–828.

[59] S. Miyazaki, in:, Eng. Asp. Shape Mem. Alloy., 1990, pp. 394–413.

[60] S.W. Robertson, a R. Pelton, R.O. Ritchie, Int. Mater. Rev. 57 (2012) 1–37.

[61] C. Dunand-Chatellet, Z. Moumni, Int. J. Fatigue 36 (2012) 163–170.

[62] G. Eggeler, E. Hornbogen, A. Yawny, A. Heckmann, M. Wagner, Mater. Sci. Eng. A 378 (2004) 24–33.

[63] R. Vaidyanathan, D.C. Dunand, U. Ramamurty, Mater. Sci. Eng. A 289 (2000) 208–216.

[64] A.L. McKelvey, R.O. Ritchie, J. Biomed. Mater. Res. 47 (1999) 301–308.

[65] P. Filip, M. Paliwal, K. Mazanec, Zeitschrift Für Met. 95 (2004) 356–361.

[66] A.L. McKelvey, R.O. Ritchie, Metall. Mater. Trans. A 32 (2001) 731–743.

[67] R.L. Holtz, K. Sadananda, M.A. Imam, Int. J. Fatigue 21 (1999) S137–S145.

[68] S.W. Robertson, R.O. Ritchie, Biomaterials 28 (2007) 700–709.

[69] J.M. Stankiewicz, S.W. Robertson, R.O. Ritchie, J. Biomed. Mater. Res. Part A 81A (2007) 685–691.

[70] O.W. Bertacchini, D.C. Lagoudas, F.T. Calkins, J.H. Mabe, Behav. Mech. Multifunct. Compos. Mater. 2008 6929 (2008) 692916-692916–11.

[71] O.W. Bertacchini, J. Schick, D.C. Lagoudas, SPIE Smart Struct. Mater. Nondestruct. Eval. Heal. Monit. 7289 (2009) 72890P--72890P.

[72] C. Calhoun, D. Lagoudas, 52nd AIAA/ASME/ASCE/AHS/ASC Struct. Struct. Dyn. Mater. Conf. (2011) 1–8.

[73] O.W. Bertacchini, D.C. Lagoudas, E. Patoor, Int. J. Fatigue 31 (2009) 1571–1578.

[74] M. Karhu, T. Lindroos, Smart Mater. Struct. 19 (2010) 115019.

[75] R. Casati, A. Tuissi, J. Mater. Eng. Perform. 21 (2012) 2633–2637.

[76] M.J. Bigeon, M. Morin, Scr. Mater. 35 (1996) 1373–1378.

[77] C.N. Saikrishna, K. V. Ramaiah, J. Bhagyaraj, Gouthama, S.K. Bhaumik, Mater. Sci. Eng. A 587 (2013) 65–71.

[78] G. Scirè Mammano, E. Dragoni, J. Mater. Eng. Perform. 23 (2014) 2403–2411.

[79] V. Demers, V. Brailovski, S.D. Prokoshkin, K.E. Inaekyan, Mater. Sci. Eng. A 513–514 (2009) 185–196.

[80] J.L. McNichols, P.C. Brookes, J.S. Cory, J. Appl. Phys. 52 (1981) 7442–7444.

[81] H. Iwanaga, H. Tobushi, H. Ito, JSME Int. Journal. Ser. 1, Solid Mech. Strength Mater. 31 (1988) 634–637.

[82] H. Tobushi, K. Kimura, H. Iwanaga, J.R. Cahoon, JSME Int. Journal. Ser. 1, Solid Mech. Strength Mater. 33 (1990) 263–268.

[83] F. Xiong, Y. Liu, E. Pagounis, J. Alloys Compd. 415 (2006) 188–192.

[84] K. V. Ramaiah, C.N. Saikrishna, V.R. Ranganath, V. Buravalla, S.K. Bhaumik, Mater. Sci. Eng. A 528 (2011) 5502–5510.

[85] T. Baxevanis, A.F. Parrinello, D.C. Lagoudas, Int. J. Plast. 50 (2013) 158–169.

[86] S. Jape, T. Baxevanis, D.C. Lagoudas, Shape Mem. Superelasticity 2 (2016) 104–113.

[87] S. Jape, T. Baxevanis, D.C. Lagoudas, Proc. SPIE 9058 (2014) 905802–905809.

[88] S. Gollerthan, M.L. Young, A. Baruj, J. Frenzel, W.W. Schmahl, G. Eggeler, Acta Mater. 57 (2009) 1015–1025.

[89] S. Gollerthan, D. Herberg, a. Baruj, G. Eggeler, Mater. Sci. Eng. A 481–482 (2008) 156–159.

[90] A. Ahadi, Q. Sun, Scr. Mater. 113 (2016) 171–175.

[91] S. Daly, a. Miller, G. Ravichandran, K. Bhattacharya, Acta Mater. 55 (2007) 6322–6330.

[92] T. Baxevanis, D. Lagoudas, Int. J. Fract. 175 (2012) 151–166.

[93] T. Baxevanis, Y. Chemisky, D.C. Lagoudas, Smart Mater. Struct. 21 (2012) 94012.

[94] A. Evirgen, Microstructural Characterization and Shape Memory Response of Ni-Rich NiTiHf and NiTiZr High Temperature Shape Memory Alloys, Texas A&M University, 2014.

[95] B. Reedlunn, S. Daly, J. Shaw, in:, ASME 2012 Conf. Smart Mater. Adapt. Struct. Intell. Syst., 2012, pp. 213–222.

[96] F.M. Davidson, C. Liang, D.W. Lobitz, in:, Smart Struct. Mater. 1996 Smart Struct. Integr. Syst., 1996, pp. 672–682.

[97] ASTM, Stand. Des. E1820-11 11 (2011).

[98] J. Blaber, B. Adair, A. Antoniou, Exp. Mech. 55 (2015) 1105–1122.

[99] E. Hornbogen, Fatigue Fract. Eng. Mater. Struct. 25 (2002) 785–790.

[100] E. Hornbogen, G. Eggeler, Materwiss. Werksttech. 35 (2004) 255–259.

[101] I. Karaman, H. Ersin Karaca, H.J. Maier, Z.P. Luo, Metall. Mater. Trans. A Phys. Metall. Mater. Sci. 34 A (2003) 2527–2540.

[102] B. Kockar, I. Karaman, A. Kulkarni, Y. Chumlyakov, I. V. Kireeva, J. Nucl. Mater. 361 (2007) 298–305.

[103] B. Kockar, K.C. Atli, J. Ma, M. Haouaoui, I. Karaman, M. Nagasako, R. Kainuma, Acta Mater. 58 (2010) 6411–6420.

[104] Z.G. Wang, X.T. Zu, L.P. You, X.D. Feng, C.F. Zhang, J. Mater. Sci. 39 (2004) 3391–3395.

[105] J. Perkins, Scr. Metall. 8 (1974) 1469–1476.

[106] J.M. Guilemany, J. Fernández, Scr. Metall. Mater. 30 (1994) 319–323.

[107] J.M. Guilemany, J. Fernández, J. Phys. IV Fr. 5 (1995) C2-355-C2-359.

[108] D.M. Norfleet, P.M. Sarosi, S. Manchiraju, M.F.X. Wagner, M.D. Uchic, P.M. Anderson, M.J. Mills, Acta Mater. 57 (2009) 3549–3561.

[109] T. Simon, A. Kröger, C. Somsen, A. Dlouhy, G. Eggeler, Acta Mater. 58 (2010) 1850–1860.

[110] A.R. Pelton, G.H. Huang, P. Moine, R. Sinclair, Mater. Sci. Eng. A 532 (2012) 130–138.

[111] L. Contardo, G. Guénin, Acta Metall. Mater. 38 (1990) 1267–1272.

[112] K.C. Atli, I. Karaman, R.D. Noebe, Scr. Mater. 65 (2011) 903–906.

[113] K.C. Atli, I. Karaman, R.D. Noebe, D. Gaydosh, Mater. Sci. Eng. A 560 (2013) 653–666.

[114] K.C. Atli, I. Karaman, R.D. Noebe, G. Bigelow, D. Gaydosh, Smart Mater. Struct. 24 (2015) 125023.